BEHAVIOR OF THREE-SPAN CONTINUOUS PRE-STRESSED CONCRETE GIRDER FOR PRECAST CONSTRUCTION OF MONORAIL TRANSIT SYSTEM

ATHASIT SIRISONTHI

A Thesis Submitted to the Graduate School of Naresuan University
in Partial Fulfillment of the Requirements
for the Doctor of Philosophy in Civil Engineering
2021

BEHAVIOR OF THREE-SPAN CONTINUOUS PRE-STRESSED CONCRETE GIRDER FOR PRECAST CONSTRUCTION OF MONORAIL TRANSIT SYSTEM

ATHASIT SIRISONTHI

A Thesis Submitted to the Graduate School of Naresuan University
in Partial Fulfillment of the Requirements
for the Doctor of Philosophy in Civil Engineering
2021

Thesis entitled "Behavior of Three-Span Continuous Pre-stressed Concrete Girder for Precast Construction of Monorail Transit System"

By ATHASIT SIRISONTHI

has been approved by the Graduate School as partial fulfillment of the requirements for the Doctor of Philosophy in Civil Engineering of Naresuan University

Oral Defense Committee

.... Chair
(Associate Professor Dr. Preeda Chaimahawan)

.... Advisor
(Assistant Professor Phongthorn Julphunthong)

.... Co Advisor
(Assistant Professor Dr. Panuwat Joyklad)

.... Co Advisor
(Associate Professor Dr. Suniti Suparp)

.... Internal Examiner
(Assistant Professor Dr. Sasikorn Leungvichcharoen)

Approved

....
(Associate Professor Dr. Krongkarn Chootip)

Dean of the Graduate School

Title	BEHAVIOR OF THREE-SPAN CONTINUOUS PRE-STRESSED CONCRETE GIRDER FOR PRECAST CONSTRUCTION OF MONORAIL TRANSIT SYSTEM
Author	ATHASIT SIRISONTHI
Advisor	Assistant Professor Phongthorn Julphunthong
Co-Advisor	Assistant Professor Dr. Panuwat Joyklad Associate Professor Dr. Suniti Suparp
Academic Paper	Ph.D. Dissertation in Civil Engineering, Naresuan University, 2021
Keywords	Finite element analysis, Precast concrete, Posttensioned, Girder, Straddle monorail, Pier segments, Service load, CFRP composites

ABSTRACT

This study presented the results of an experimental and finite element analysis programme conducted on a newly proposed Full-scale Precast Post-tensioned Continuous (FPPC) girder for straddle monorail. The investigated FPPC girder represents the actual size, design and construction details for a newly designed monorail transit system (Yellow Line and Pink Line Monorail) in Bangkok, Thailand. The salient features of the newly proposed girder system include lightweight, low-cost, easy and fast construction. The newly proposed FPPC girder is mainly comprised of three reinforced concrete (RC) hollow haunched girders, four piers or supports, two pier segments, four wet joints, and four bearings at each support. The FPPC girder was constructed at the casting yard of Sino-Thai Engineering and Construction Public Company Limited (STECON), Thailand. In the first part of this study, the FPPC girder was tested under different loading conditions (such as service and ultimate loading conditions). Both service and ultimate loads were applied as two-point loadings. Service load in a monotonic manner was applied on the right exterior span (two-point), middle span (two-point), and on the left exterior span and middle span (four-point). Meanwhile, the ultimate load in a monotonic manner was applied only on the left exterior and middle span as a four-point loading scheme. The test results indicate that the behaviour of the FPPC girder under service load conditions is elastic. Further, cracking of the concrete was not observed at any location. The observed maximum deflections under service load conditions were less than the permissible limits at all locations. Further, the maximum ultimate load-carrying capacity was observed to be much greater than the design load under ultimate loading conditions. This is an indication that the design details and construction procedure of FPPC girder are appropriate and further that this system could be used effectively to construct straddle monorail transit systems. In the second part of this study, small-scale reinforced concrete hollow (RCH) beams were also constructed and tested at the laboratory environment to ascertain the efficiency of Carbon Fiber Reinforced Polymer (CFRP) in enhancing flexural response of hollow section reinforced concrete (RC) beams. Nine beams were tested under four-point bending in 3 groups. Beams were categorized to reflect the presence or configuration of CFRP sheet. Each group consisted of 3 beams: 1 with solid section, 1 with a square 50 x 50 mm opening, and 1 with 100 x 100 mm opening. Beams in 1st group were tested in as-built condition. Beams in 2nd group were strengthened with a single CFRP sheet bonded to their bottom sides. Configuration of CFRP sheet was altered to U-shape applied to the tension side of 3rd group beams. Inclusion of openings, regardless of their size, did not result in degradation of ultimate load and corresponding deflections. However, cracking loads were found to decline as opening size increased. Regardless of the opening size and CFRP configuration, ultimate loads of beams increased with the application of CFRP. However, this improvement was limited to the de-bonding and rupture of CFRP in group 2 and 3 beams, respectively. A comparison in the behavior of group 2 and 3 beams revealed that the application of U-shape CFRP sheet yielded better flexural performance in comparison with flat-CFRP sheet bonded to the bottom of beams. At the end of this study, finite element analysis of FPPC monorail bridge girder was also performed by using a computer program ATENA which is a computational tool for nonlinear engineering analysis of bridges and culverts. The finite element analysis results indicate that the computer program ATENA is well capable to predict the ultimate load carrying capacity, displacement and cracking patterns of FPPC girder.

ACKNOWLEDGEMENTS

I would like to show my deep gratitude and great appreciation to my advisor, Asst. Prof. Dr. Phongthorn Julphunthong, for his valuable guidance, sensible advice and helpful criticism, which are indispensable prerequisite for the completion of this thesis. I am thankful for his bright idea and impressive example during these two years. I would like to express my warm thanks to my co-advisors: Assoc. prof. Dr. Suniti Suparp and Asst. Prof. Dr. Panuwat Joyklad, for their appreciative comments and questions which incentively broaden my perspective of thinking in term of the research works and real applications.

I am very grateful to acknowledge STECON, Naresuan University, "Research and Innovation Development Unit for Infrastructure and Rail Transportation Structural System (RIDIR) of Srinakharinwirot University, and MHPM Co., Ltd. (Guideway Beam Designer) for providing beneficial support.

My sincere thanks also goes to Dr. Preeda Chaimahawan, for his guidance and crucial discussion which widen my research from various perspectives. His knowledge and experience have taught me a lot in terms of research work. I am indepted to all my friends and who have been a part of my life.

I would like to give my profound gratitude and warmest thanks to my family: my parents, my sisters and my brothers for supporting, encouraging and always stand by me throughout my whole life. I love you all.

ATHASIT SIRISONTHI

TABLE OF CONTENTS

Page

List of table

Page

List of figures

Page

CHAPTER I
INTRODUCTION

1.1 Introduction and back ground

Reinforced concrete hollow haunched (RCHH) girders are considered to be very efficient structural systems for the construction of bridges, especially in the case of continuous spans [1, 2]. The advantages of RCHH girders include being lightweight, low-cost, and high strength as well as having superior rigidity compared to conventional reinforced concrete (RC) solid girders [3, 4]. The design of the RCHH girder is usually considered more complex owing to the effects of torsional warping and shear lag in RCHH girders due to torque loads [5-7]. In the past, extensive theoretical studies have been conducted to develop guidelines for the design of RCHH girders [8-10]. Vlasov [11] studied the behaviour of RC hollow beams and developed a theoretical concept for RC hollow beams. Later, this theory became the basis for the current theoretical models that are frequently used to analyse and design RC box girders. Since then, different concepts and approaches have been proposed to analyse single and continuous span RCHH girders [12-14]. During the last decade, RCHH girders have been frequently utilised for the construction of highway bridges and elevated monorail transit systems. Examples of single-span RCHH girder bridges include the Shibanpo Bridge in China, Rio-Niterói Bridge in Brazil, and Sundøy Bridge in Norway [15-17].

Recently, different types of transit systems have been proposed and developed for both bi-rails and monorails to address the congestion in traffic-choked cities [18]. Monorail transit systems are frequently used in small, medium and large cities due to their excellent advantages such as better climbing ability, less construction time, reduced noise and low cost. Monorail transit systems have also been adopted and constructed for hilly cities [19-21]. Monorail transit systems are generally classified in two types, i.e. straddle type and suspension type, based on the operation of monorail vehicles [22, 23]. In monorail transit systems, the role of pre-cast concrete beams or girders is very critical for the safety of the entire system because pre-cast concrete beams or girders serve as the load-bearing components and guideway. These guideway beams or girders are typically subjected to both sustained and repeated traffic loads [24, 25]. In 2007, Tokyo Monorail with Taisei Corporation constructed a 40-m-long prismatic hollow monorail girder of Ultrahigh-performance concrete UHPC [26]. The girder was constructed in three segments and was joined together on-site by a combination of wet and dry joints. The monorail girder was reportedly the longest UHPC simple-span bridge member at the time of construction. In 2009, Palm Jumeirah Monorail Civil Joint Venture, a group of Japanese contractors, constructed a 5.45 km long monorail line that included 29 m long guideway haunched beams continuous over five spans. The monorail structure was designed by Norconsult Civil Engineering Company, Limited, Thailand. The design methodology of the monorail structures was developed to accommodate the unique features of transit guideway structures, durability and constructability. An efficient continuous frame system monolithically integrated with the columns was utilized as a result [27, 28].

Bangkok is the capital of Thailand and the nation’s most populous city. The city occupies 1568 square kilometres in the Chao Phraya River delta in central Thailand and has a population of over eight million, roughly 12.6 per cent of the country's total population. At the time of the 2010 census, more than fourteen million people (22.2 per cent) lived within the surrounding Bangkok Metropolitan Region, making Bangkok the nation's primate city, significantly dwarfing Thailand's other urban centres in terms of importance. In the last decade, Bangkok has attracted millions of migrants seeking economic opportunity, causing the city to expand quickly. Currently, In Bangkok, train systems are using two types of trains i.e. diesel trains and electrical trains. Further electrical train system is comprised of elevated train system (known as BTS Sky Train) and underground train system (known as MRT Line). All existing train systems are using traditional trains not monorail. The BTS sky train system was constructed using box girders and post-tensioning was performed for individual spans (Figure 1). Recently, Mass Rapid Transit Authority (MRTA) Thailand has decided to adopt Monorail systems (Pink and Yellow line monorail systems) in Bangkok as a rapid transit system due to the limited space, narrow roads and sharp curves in the city (Fig. 2). The design of monorail track lines permits flexible and various alignments that include curves of small radiuses and large slopes. The design and construction of both systems were assigned to Sino-Thai Engineering and Construction Public Company Limited (STECON). Since Bangkok is a highly-populated city with narrow roads and sharp curves, the construction of a traditional sky train system may cause difficulties in terms of construction, significant construction costs and time. In contrast to the traditional monorail systems, STECON proposed a novel four-span post-tensioned girder system (PTGS), in which four Guideway Beams (GWBs) would be post-tensioned in such a way that the post-tension tendons would run through four consecutive spans. The salient features of the proposed system are low cost, safety and less construction time. The proposed monorail system is the 1st monorail project in Thailand with a unique concept for its design and construction [29].

Figure 1 Box girder bridge for BTS sky train in Bangkok, Thailand.

Figure 2 Typical display of Pink line and Yellow line monorail transit systems [29].

To date, there is very little published literature on the ultimate behavior of bridges as a structural system. In particular, few tests have been performed on pre-stressed concrete girder and slab bridges, despite this bridge type being extremely common around the world. Information about failure mechanisms in bridges can provide important guidance to designers and can improve computer modelling techniques to more accurately represent bridge behavior. Since bridges are complex systems, there is no substitute for actual load tests to failure to verify the calculations of individual component capacity. A review of concrete bridge tests performed around the world determined that shear failures were particularly hard to predict, non-structural elements (like diaphragms) often contribute to capacity, and there were fewer tests of pre-stressed concrete girder bridges than reinforced concrete bridges. Pu et al. [22] experimentally studied the elastic range fatigue behavior of pre-stressed concrete beams for straddle-type monorail track systems in a simple supported manner. The displacement and rotation of the beam of concrete and reinforcement were examined, respectively. A three-dimensional finite element model was established to help understand the development of mechanical behavior [22].

As such, the objective of the current experimental study is to investigate the elastic and plastic structural response of a Full-scale Precast Post-tensioned Continuous (FPPC) girder for straddle monorail - a subject that has not yet been explored. For this, a full-scale three-span post-tensioned monorail bridge girder representative of actual construction details of monorail systems (Pink and Yellow line monorail systems) in Bangkok was constructed and tested under different loading conditions such as service load and ultimate load to investigate both the elastic and plastic structural responses. Although the actual construction of the Pink and Yellow line monorail systems comprises a four-span post-tensioned girder system, this study only considered three continuous spans to minimize the costs. The maximum mid-span deflections of interior and exterior span girders are found to be less than the allowable limits under service load conditions, and ultimate failure of the three-span post-tension system mainly occurred due to the cracking and crushing of the concrete near the wet joints. In the second step, Finite element analysis of FPPC monorail bridge girder was performed by using a computer program ATENA, which is a computational tool for nonlinear engineering analysis of bridges and culverts. The finite element analysis results indicate that the computer program ATENA is well capable to predict the ultimate load carrying capacity, displacement and cracking patterns of FPPC girder. At the end of this study, small-scale reinforced concrete hollow (RCH) beams were also constructed and tested at the laboratory environment to ascertain the efficiency of Carbon Fiber Reinforced Polymer (CFRP) in enhancing flexural response of hollow section reinforced concrete (RC) beams. Nine beams were tested under four-point bending in 3 groups. Beams were categorized to reflect the presence or configuration of CFRP sheet. Each group consisted of 3 beams: 1 with solid section, 1 with a square 50 x 50 mm opening, and 1 with 100 x 100 mm opening. Beams in 1st group were tested in as-built condition. Beams in 2nd group were strengthened with a single CFRP sheet bonded to their bottom sides. Configuration of CFRP sheet was altered to U-shape applied to the tension side of 3rd group beams. Inclusion of openings, regardless of their size, did not result in degradation of ultimate load and corresponding deflections. However, cracking loads were found to decline as opening size increased. Regardless of the opening size and CFRP configuration, ultimate loads of beams increased with the application of CFRP. However, this improvement was limited to the de-bonding and rupture of CFRP in group 2 and 3 beams, respectively. A comparison in the behavior of group 2 and 3 beams revealed that the application of U-shape CFRP sheet yielded better flexural performance in comparison with flat-CFRP sheet bonded to the bottom of beams. At the end, In order to further evaluate the economic and performance benefits of these beams, the cost-benefit analysis was also performed. The analysis showed that the feasibility of the hollow section RC beams is more than the solid section RC beams.

1.2 Problem Statement

To date, there is very little published literature on the ultimate behaviour of mono-rail bridge girders as a structural system. In particular, few tests of pre-stressed concrete girders and slab bridges have been performed despite this bridge type being extremely common across the world. Information about failure mechanisms in bridge girders can provide important guidance to designers and can improve computer modelling techniques to more accurately represent bridge behaviour. This study details the construction and testing to failure of real scale three-span continuous post-tensioned monorail bridge girders - a subject that has not been explored in the past. Further, there is need to develop a finite element model which can be accurately used to predict the ultimate behaviour of mono-rail bridge girders. Also, there is need to investigate the effect of openings on the structural behaviour of large-scale hollow section RC beams. Especially openings of larger dimensions which could significantly reduce the weight and cost of the RC beams. A detailed review of existing literature indicates that the so far openings of large dimensions have not yet been studied in RC beams. Additionally, the efficiency of Carbon Fiber Reinforced Polymer (CFRP) in enhancing flexural response of hollow section reinforced concrete (RC) beams is not yet clear especially under different strengthening configurations.

1.3 Objectives of the Study

•The objective of the large-scale experimental study was to investigate the elastic and plastic structural response of a Full-scale Precast Post-tensioned Continuous (FPPC) girder for straddle monorail - a subject that has not yet been explored to ascertain the accuracy of the design.

•Another objective was to investigate the effect of different loading conditions such as service and ultimate loads on the structural behavior of the Full-scale Precast Post-tensioned Continuous (FPPC) girder.

•To investigate the effect to loading conditions on different spans of the Full-scale Precast Post-tensioned Continuous (FPPC) girder such as exterior and interior spans.

•To develop an analytical tool which can be used to accurately predict the ultimate behaviour of the Full-scale Precast Post-tensioned Continuous (FPPC) girder.

•To investigate the effect of openings on the structural behavior of small-scale hollow section RC beams. Especially openings of larger dimensions which could significantly reduce the weight and cost of the RC beams.

•To investigate the efficiency of Carbon Fiber Reinforced Polymer (CFRP) in enhancing flexural response of hollow section reinforced concrete (RC) beams with different strengthening configurations.

1.4 Scope and limitations of the study

The main scope of this study was to evaluate the behavior of newly proposed three-span mono-rail girder system both through real-scale test to failure and by performing finite element analysis using computer program ATENA. The proposed test specimen is comprised of three main girders, two intermediate pier segments and wet joints. In the first step, pre-cast concrete girders and pier segments will be installed at the pre-built supports (columns) and then in the second step, tendons will be installed through pre-cast girders and pier segments. Once tendons are installed and post-tensioned, the joints between the main girders and pier segments will be filled using high performance non-shrink grout. The behavior and structural response of the wet joints is very critical in this system. Special attention will be paid to monitor the crack development at the location of wet joints. Different loading conditions such as axial service load, torsional service load and ultimate loads will be considered to evaluate the structural response of the proposed system. Another scope of this study was to investigate the effect of openings on the structural behavior of large-scale hollow section RC beams and to study the different configurations of carbon fiber reinforced polymers (CFRP) in enhancing flexural response of hollow section reinforced concrete (RC) beams.

1.5 Research significant

To date, a few studies has been conducted on single-span full- scale pre-cast post-tensioned girders. In order to ensure the structural safety of the multi-span monorail girders, it is very important to investigate the structural response through full-scale experimental investigations and finite element analysis. In this study, a full-scale three-span post-tensioned full-scale girder system was constructed and tested under static axial loading to investigate the structural response of the proposed systems. Total length of the test specimen was approximately 100 meter. The proposed test setup was first ever experimental investigation which provided very useful data to customize the design and cost of the monorail girders. Finite element analysis of FPPC monorail bridge girder was also performed by using a computer program ATENA which is a computational tool for nonlinear engineering analysis of bridges and culverts. The finite element analysis results indicate that the computer program ATENA is well capable to predict the ultimate load carrying capacity, displacement and cracking patterns of FPPC girder.

There are limited studies on RC beams with hollow sections. There is need to investigate the effect of openings on the structural behavior of large-scale hollow section RC beams. Especially openings of larger dimensions which could significantly reduce the weight and cost of the RC beams. Given that openings in RC beams reduce their capacities significantly, the need of their strengthening for optimal performance cannot be overlooked. This study further aims at investigating fiber reinforced polymer (FRP) application on rectangular hollow beams in enhancing their flexural strengths.

Chapter II

Theory and Previous Research

2.1 Related Theory

In the current research work, the structural response of the proposed pre-cast post-tensioned girder system will be investigate under two different conditions such as service load condition and ultimate load conditions. Further details of each condition are discussed in the following sections;

2.1.1 Service load condition

The main objective of this loading condition is to verify the structural response of the proposed pre-cast post-tensioned girder system in terms of crack appearance and deflection. From design point of view and structural safety requirements, at service load condition the maximum deflection should not be greater than span/1000 without any crack occurrence. Thus in service load conditions maximum load will be applied up to the service state. The criterial for service state will be developed by using the tensile strain of the steel bars in the tension region. Service state will be considered onset of 50% yield stain in the steel bars. Further in order to completely evaluate the structural response of the proposed three-span pre-cast post-tensioned girder system, the service load will be applied separately both at the exterior and interior spans. On each span, two-point loading will be applied using hydraulic jacks. A detailed description about the loading conditions and intervals is provided in the sections 3.4.1 to 3.4.3.

2.1.2 Ultimate load condition

The main objective of ultimate load condition is to evaluate the detailed structural response of the proposed pre-cast post-tensioned girder system up to the ultimate failure and or collapse. In this condition, four point loading will be applied at time. Four point loading will be considered by applying two point loading at each interior and exterior girder. During the loading, complete response of the three-span system will be monitored by using large number of linear variable differential transducers and strain gauges. The structural response of the wet joints will be observed through the crack gauges. The structural response of the longitudinal steel bars, vertical steel bars and post-tension tendon wires will be recorded through the strain gauges. The behavior of the bearings will also be monitored through linear variable differential transducers and strain gauges. During the test, the crack appearance and propagation will be monitored through the visual inspection and recorded using cameras. A detailed description about the loading conditions and intervals is provided in the section 3.4.4.

2.2 Literature Review

The behavior of the pre-stressed bridge girders both at small scale (laboratory tests) and full scale (field tests) have been extensively studied in the past all around the world. Different research parameters were considered and investigated to customize the design of bridge girders. A few of those studies are summarized in the following sections;

2.2.1 Laboratory Tests

Nurray et al. 2019 performed destructive testing and computer modeling of a scale pre-stressed concrete girder bridge. In their study, scale pre-stressed concrete bridge was constructed to investigate the ultimate behavior of the bridge with particular focus on load distribution after cracking and on contribution of full-depth diaphragms to structural capacity. A point load was applied at the quarter-span point of the bridge over an interior girder. As the loaded girder failed, the diaphragm-girder connection cracked. Torsion was observed to cause cracking in the exterior girder and the end diaphragm rotated away from the bridge as the deck deformed. A punching shear failure ended the test; however, damage indicative of two-way slab behavior was observed in the deck. This failure suggests that post girder failure, the diaphragms provide an important means of load transfer, allowing moment redistribution in the deck and potentially increasing capacity. Testing in the elastic range compared favorably with respect to deflections and shear distribution factors from a grillage model, a 2-D finite element model and a 3-D finite element model [30].

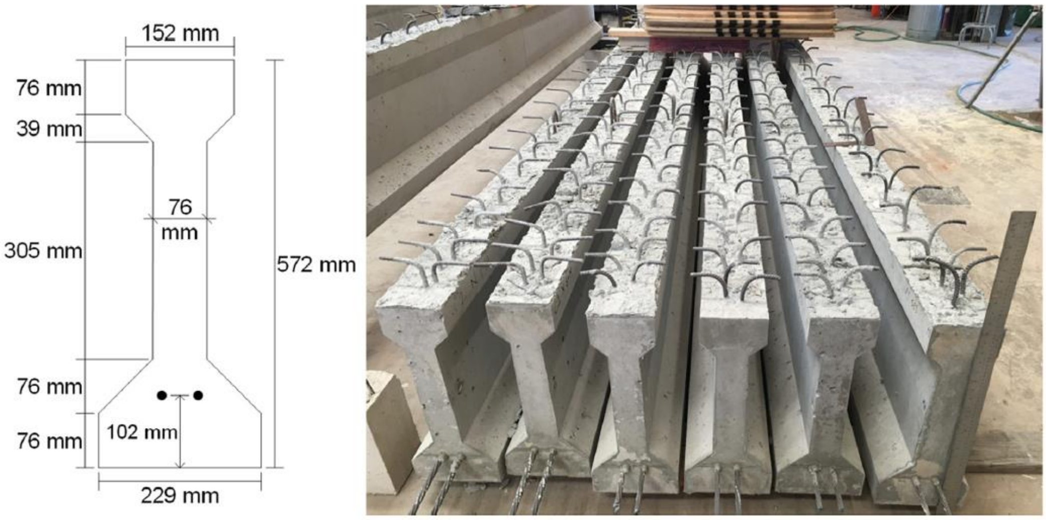

Figure 3 Scale girder dimensions (left) and completed sections (right) [30]

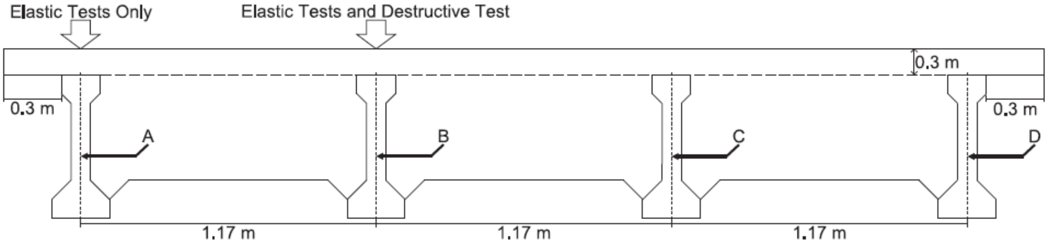

Figure 4 Girder naming convention and location of loads [30]

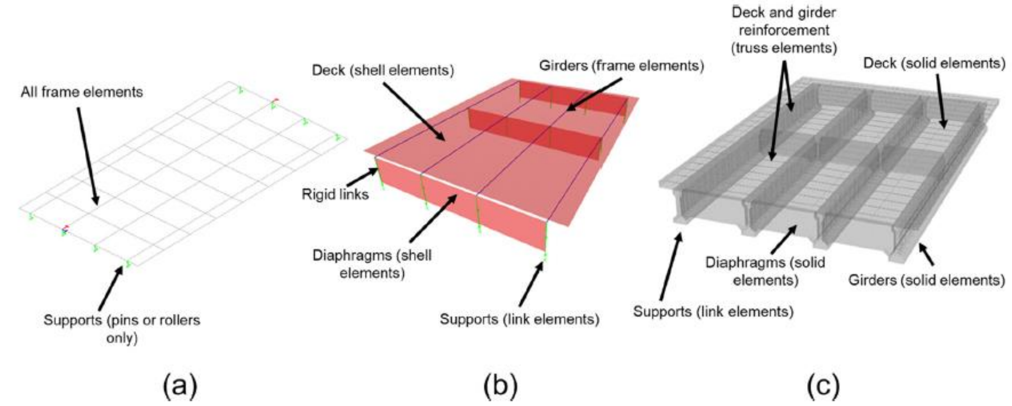

Figure 5 Isometric view of models; (a) 2-D grillage, (b) 2-D model, (3) 3-D model [30]

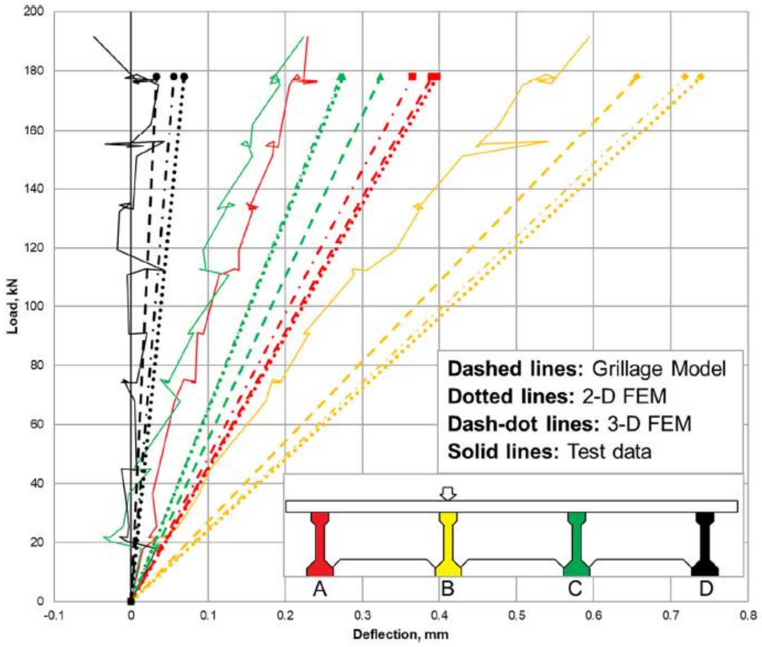

Figure 6 Comparison of load versus deflection [30]

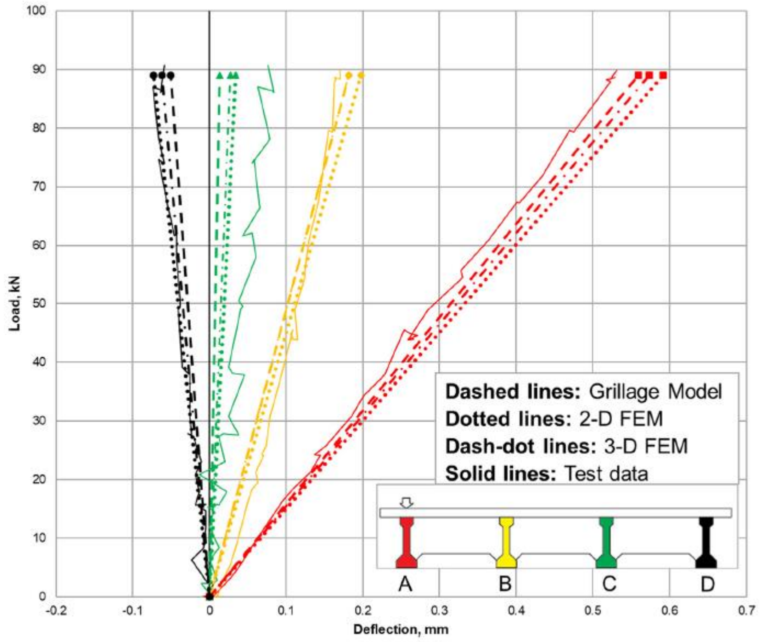

Figure 7 Comparison of load versus deflection relationships for computer models and scale bridge loaded at girder A [30]

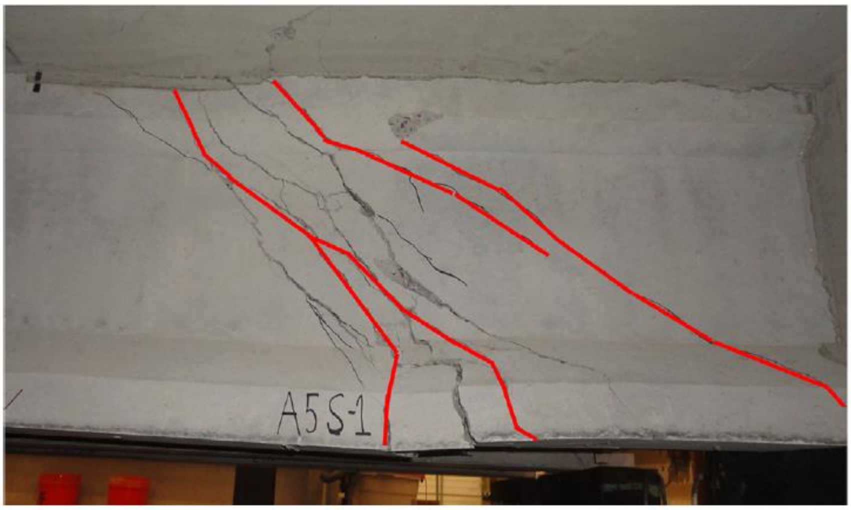

Figure 8 Girder B final cracking (cracking at 334 kN of load outlined in red) [30]

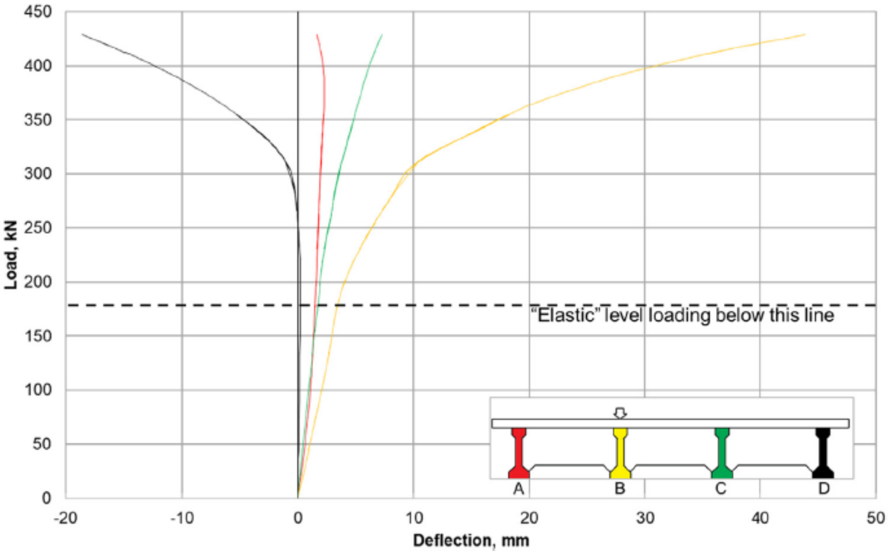

Figure 9 Load vs. deflection for bridge test [30]

Pu et al. 2018 experimentally studied the fatigue behavior of pre-stressed concrete (PC) beam for straddle type mono-rail track system in a simply supported manner. The displacement and rotation of the beam of concrete and reinforcement were examined, respectively. A three-dimensional finite element model was established to help understand the development of the mechanical behavior. A PC beam was fabricated to represent the typical PC track beam for a straddle-type monorail. The PC beam had a rectangular hollow cross section measuring 700 mm (width) × 1500 mm (height) and a length of 24,000 mm (net span 23,200 mm). The end of the girder specimen had a solid section to accommodate the application of the post-tensioning force. A three-dimensional finite element model was established to help understand the development of the mechanical behavior. No crack was observed throughout the test. Both concrete and bars behaved in their linear-elastic stage throughout the test, and the bond between them performed well [22].

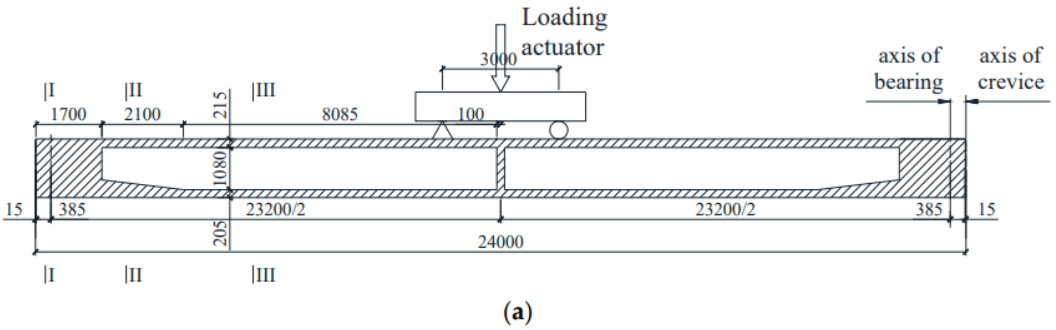

Figure 10 Detailed dimensions of the specimen (unit: mm): (a) Front of elevation; (b) sectional view [22]

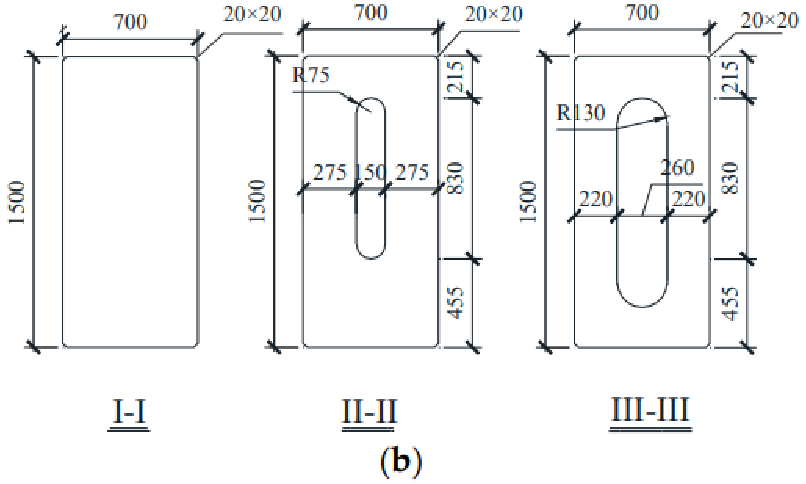

Figure 11 Detailed dimensions of the specimen (unit: mm): (a) Front of elevation; (b) sectional view [22]

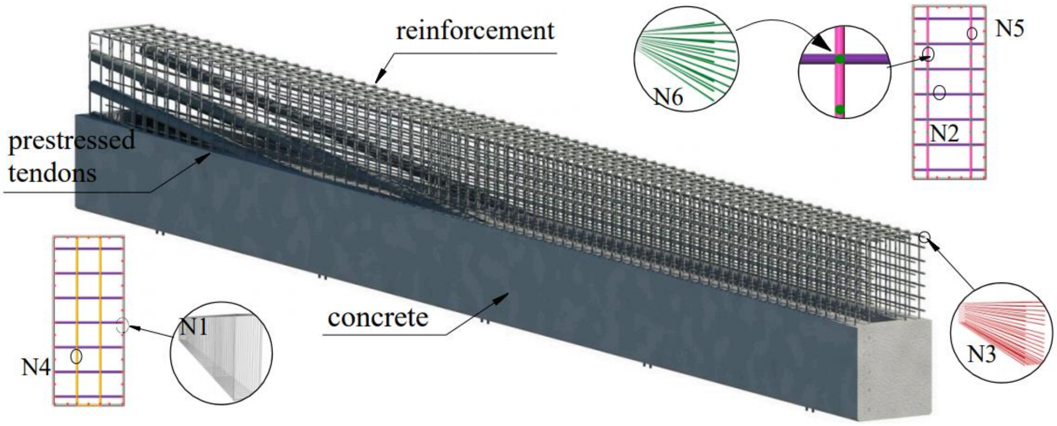

Figure 12 Details of reinforcement bars [22]

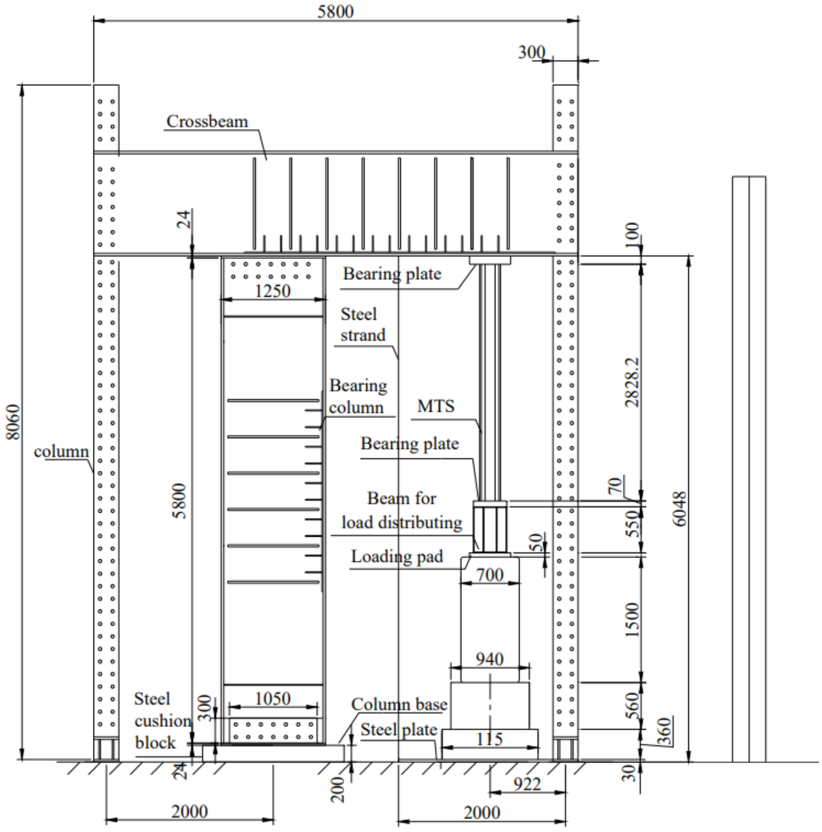

Figure 13 Elevation schematic view of the test setup (unit: mm) [22]

(a) (b)

Figure 14 Loading setup (a) specimen and device and (b) detail of testing system actuator [22]

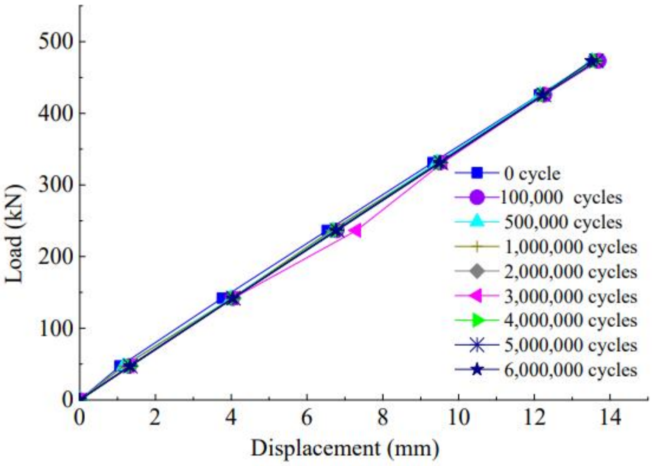

Figure 15 Static load-displacement curve at mid-span [22]

Tokyo Monorail and Taisei corporations have been carrying out the corporative technical development of a 40m long monorail girder applying the UFC that must be the longest span in the world made of concrete material (Photo. 4). Because of the length re in-situ UFC. It should be noted that the dry joints for U girders are located in inner side of the span but the wet-joints for bottom slabs are located outside of the dry joint as shown in Figure 4. The tensile stress for the design load of service limit state (SLS) should be less than the first cracking strength (f_{cr}=8 N/mm.^{2}) except the joint section, however the tensile stress for SLS cannot be allowed on both types of joint; i.e. it should be full pre-stressing for those joints. It is therefore possible to reduce the pre-stressing cables compared with the case that the locations of both joints coincide. The section of the dry joint and the wet join is shown in figure 5 and 6, respectively. Most of the modelling parameters of the proto-type 10m long monorail girder such as girder width, combination of joints and pre-cast segments, surface finishing of top slab and sizes of PBL are identical with the 40m long girder except the total length and the height (Fig. 7). There are two main purposes for the proto-type monorail girder; i.e. one is to confirm the erection and fabrication method for the complex composition of the pre-cast segments, and another is to verify the structural safety including two kinds of joints. The sequential fabrication steps such as production of segments, match casting, dry joint and wet joint were implemented and evaluated how those effect on the final structural performance. The loading set up for the completed proto-type girder was arranged so that both joints could have both bending moment and shear force (Fig. 7). The experimental result and a 3D-FEM analysis considered the modelling of material nonlinearity is indicated in Figure 8. Because a 10m long monorail girder instead of a 40 m girder was to be tested to prove the structural safety, the equivalent loading values were calculated so as to have equivalent forces at joints for SLS and ULS. The loading value P for SLS and ULS became 830 kN and 1748 kN, respectively. It was proven that no initial cracking was observed for SLS and no serious damage for ULS. The first cracking was observed at the bottom slab of mid-span for the loading value P = 1200 ~ 1300 kN. At the same time, the first cracking at wet joint of bottom slab was found. For the loading value P=1700kN, the diagonal cracks were observed on web [31].

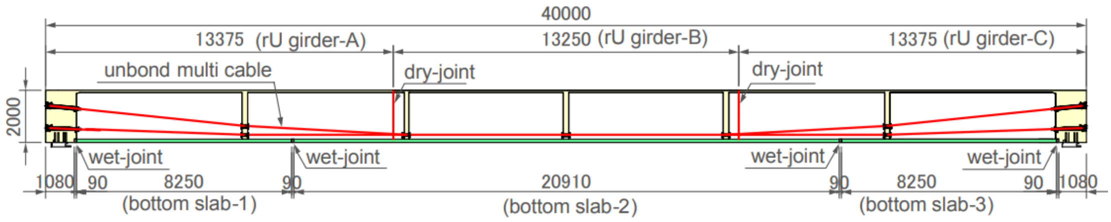

Figure 16 Longitudinal sectional details [31]

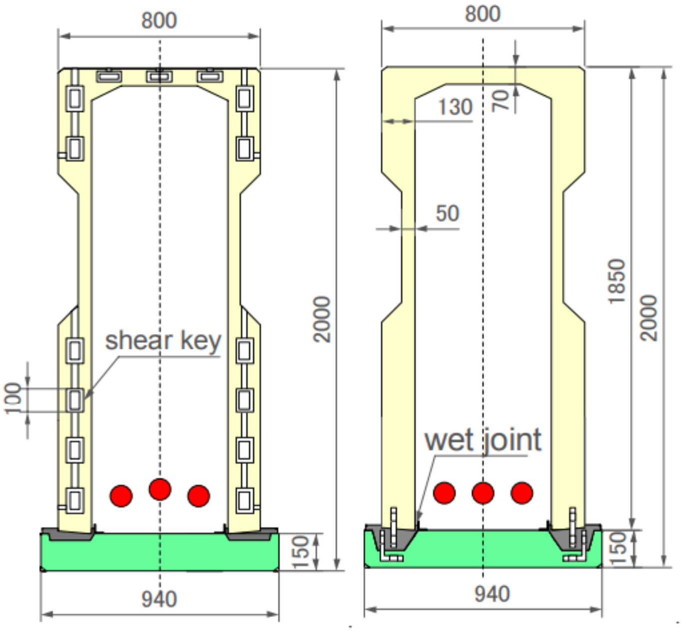

Figure 5. Dry-joint. Figure 6. Wet-joint.

Figure 17 Cross sectional details [31]

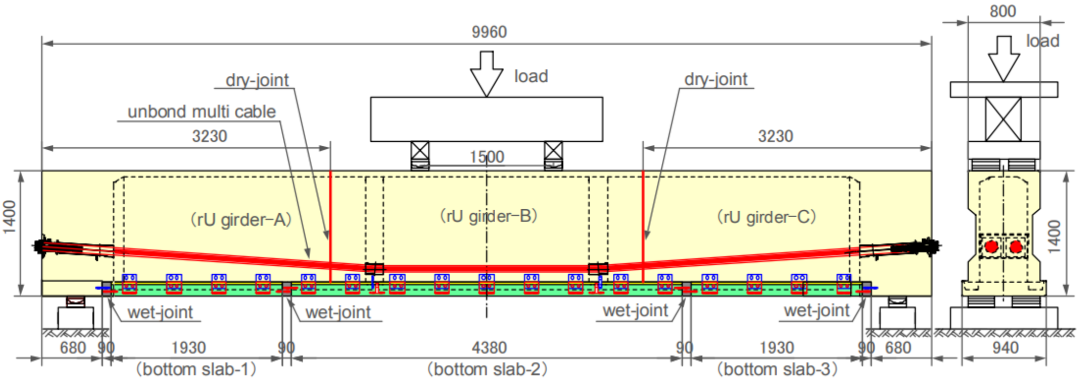

Figure 18 Structural composition of pre-cast segments and loading set up for proto-type girder [31]

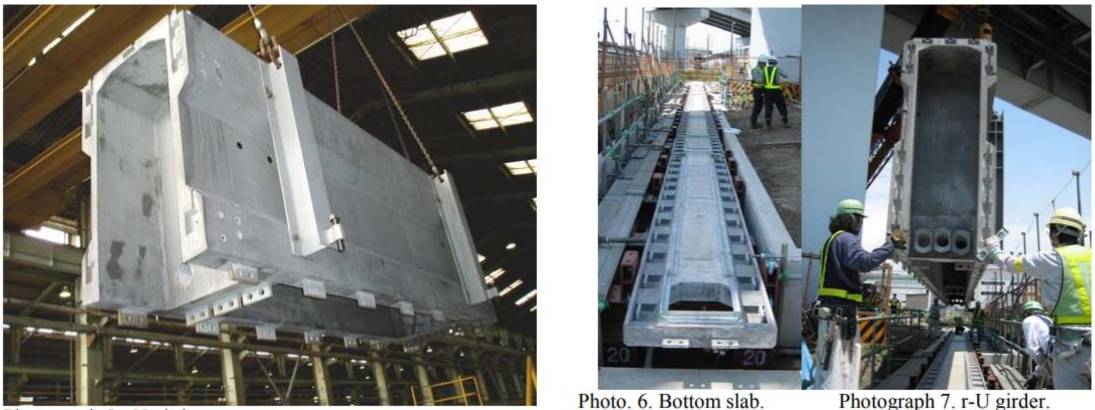

Photograph 5. rU girder segment.

Photo. 6. Bottom slab.

Photograph 7. r-U girder.

Figure 19 Construction process of girders [31]

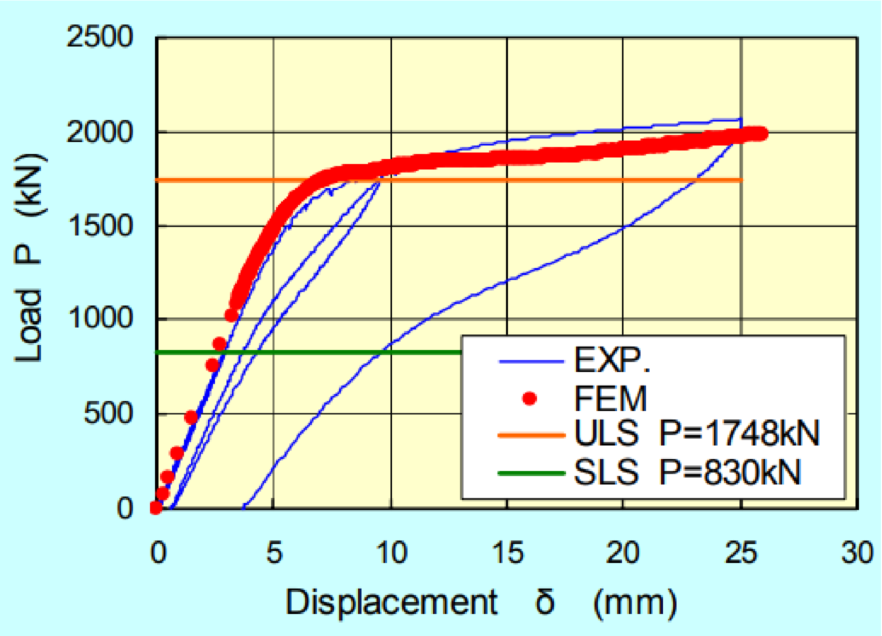

Figure 20 Comparison of experimental and FEM analysis [31]

Graybeal 2008 investigated the flexural behavior of an ultrahigh-performance concrete I-girder. The flexural behavior of an ultrahigh-performance concrete UHPC was investigated through the testing and related analysis of a full-scale pre-stressed I-girder. A 28 ksi 193 MPa compressive strength steel fiber reinforced concrete was used to fabricate an 80 ft 24.4 m long AASHTO Type II girder containing 26 pre-stressing strands and no mild steel reinforcement. Intermediate and final behaviors, including cracking, flexural stiffness, and moment capacity, were investigated. Test results are compared to predictions based on standard analytical procedures. A relationship between tensile strain and crack spacing is developed. The uniaxial stress-strain response of UHPC when subjected to flexural stresses in an I-girder is determined and is verified to be representative of both the stress and flexural stiffness behaviors of the girder [32].

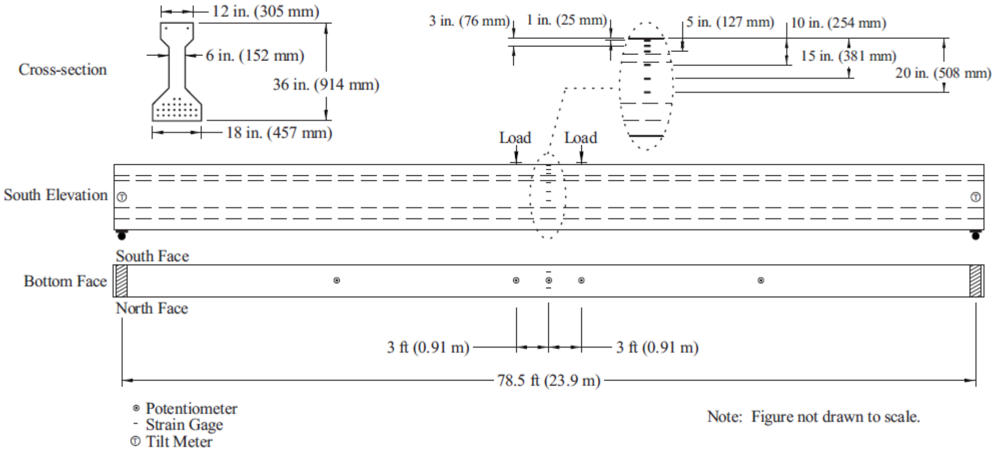

Figure 21 Cross section, loading configuration, and instrumentation plan [32]

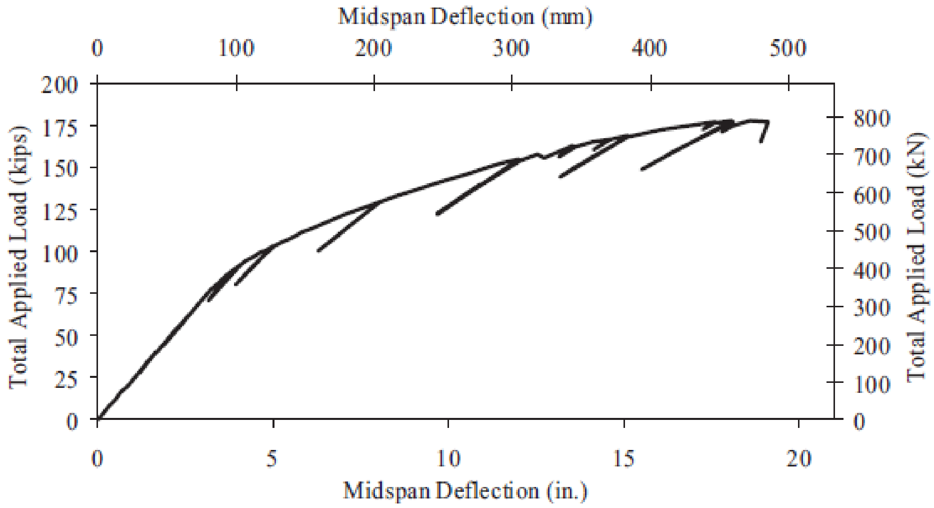

Figure 22 Flexural behavior of AASHTO Type II UHPC girder [32]

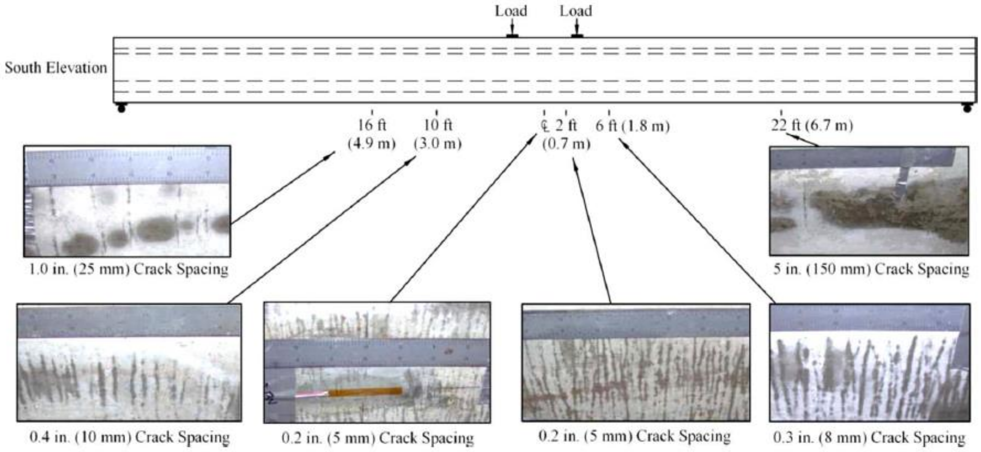

Figure 23 Cracking pattern [32]

Aravinthan et al. 2005 studied the flexural behavior of two-span continuous pre-stressed concrete girders with highly eccentric external tendons. The effect of tendon layout, loading pattern, casting method, and confinement reinforcements on the flexural strength and stress in external tendons was investigated. A series of experiments was carried out using a total of nine beams to investigate the flexural behavior of beams pre-stressed with highly eccentric external tendons. The test series consisted of six specimens with two-span continuous beams (Types A, B, and C) and three single-span beams (Type D). The two-span continuous beams are 10.4 m long, with two equal spans of 5.0 m. The major variables were the tendon layout, based on linear transformations, and the loading pattern on each span. Based on experimental results, it was concluded that the flexural behavior of beams is not affected by the linear transformation of tendon layout in both elastic and post-elastic loading ranges. The presence of confinement reinforcement enhances the ductility behavior but does not increase the ultimate strength of such beams. Frictional effects at the deviators had some effect in the case of unsymmetrically loaded beams due to the large deviation angle of the external tendons. Further, the stress increase in single-span beams was nearly the same as that of symmetrically loaded continuous beams, which supports previous findings by the authors [33].

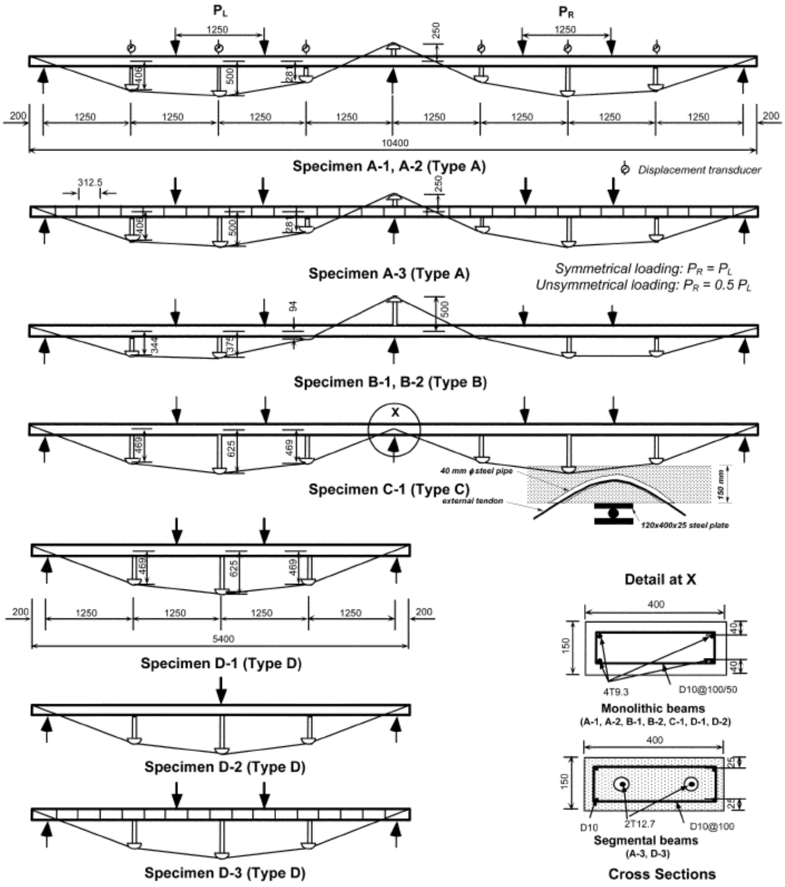

Figure 24 Details of test specimens [33]

Table 1 Summary of experiment results [33]

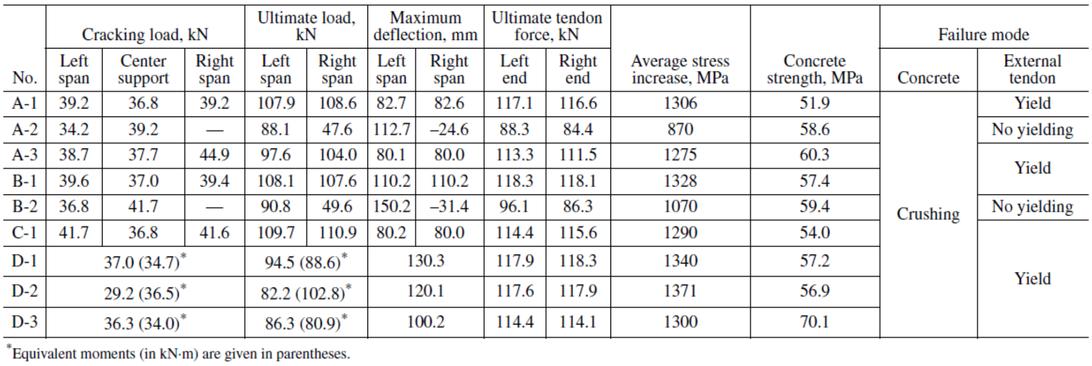

No.	Cracking load, kN			Ultimate load, kN		Maximum deflection, mm		Ultimate tendon force, kN		Average stress increase, MPa	Concrete strength, MPa	Failure mode	
	Left span	Center support	Right span	Left span	Right span	Left span	Right span	Left end	Right end			Concrete	External tendon
A-1	39.2	36.8	39.2	107.9	108.6	82.7	82.6	117.1	116.6	1306	51.9	Crushing	Yield
A-2	34.2	39.2	—	88.1	47.6	112.7	–24.6	88.3	84.4	870	58.6		No yielding
A-3	38.7	37.7	44.9	97.6	104.0	80.1	80.0	113.3	111.5	1275	60.3		Yield
B-1	39.6	37.0	39.4	108.1	107.6	110.2	110.2	118.3	118.1	1328	57.4		
B-2	36.8	41.7	—	90.8	49.6	150.2	–31.4	96.1	86.3	1070	59.4		No yielding
C-1	41.7	36.8	41.6	109.7	110.9	80.2	80.0	114.4	115.6	1290	54.0		Yield
D-1	37.0 (34.7)*			94.5 (88.6)*		130.3		117.9	118.3	1340	57.2		
D-2	29.2 (36.5)*			82.2 (102.8)*		120.1		117.6	117.9	1371	56.9		
D-3	36.3 (34.0)*			86.3 (80.9)*		100.2		114.4	114.1	1300	70.1		

*Equivalent moments (in kN·m) are given in parentheses.

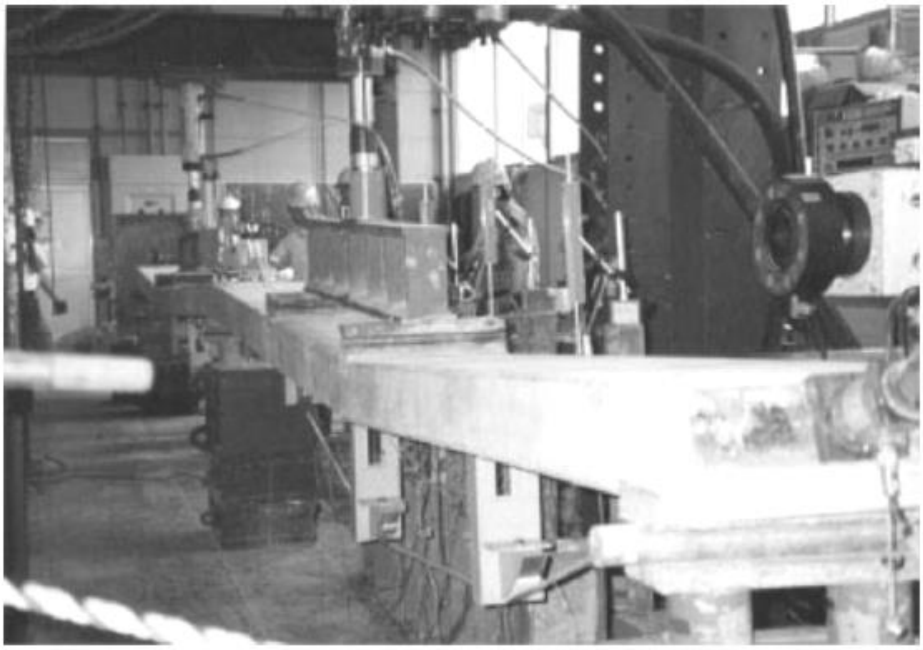

Figure 25 Testing of continuous beam specimen [33]

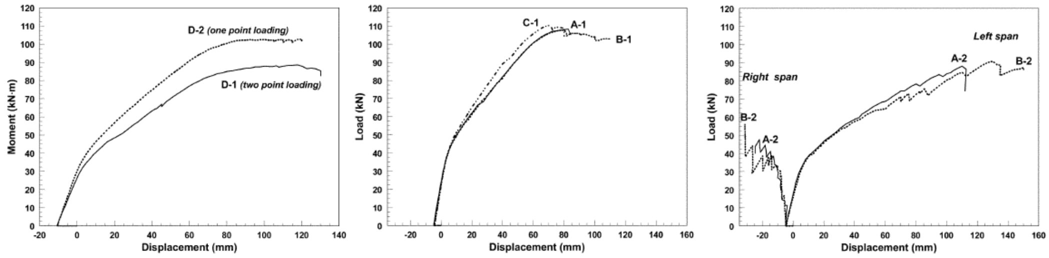

(a) Single span (monolithic beams) (b) Continuous beams (symmetrical loading) (c) Continuous beams (unsymmetrical loading)

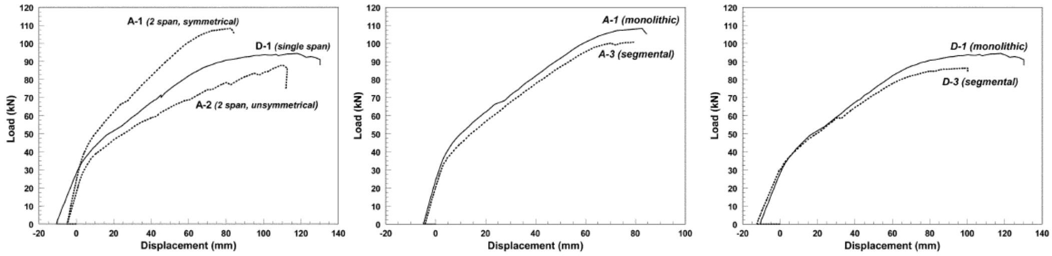

Figure 26 Load-displacement characteristics [33]

Murray et al. 2019 conducted a comprehensive study including detailed analysis and shear testing to failure was conducted on two AASHTO Type II girders obtained from the I-244 bridge over the Arkansas River in Tulsa after approximately 47 years in service. Small-scale girders with a matching design were also tested individually and as a composite bridge section to evaluate the effects of composite behavior in resisting shear. Additionally, a number of inverse techniques and non-destructive testing methods were evaluated to determine their applicability for determining material properties and detecting damage in prestressed concrete bridges. In all shear tests of the two full-size girders, the applied loads exceeded expected loads whether determined from shear capacity calculations, flexural capacity by strain compatibility, or design demands from AASHTO LRFD. Tests of the individual and composite small-scale girders indicated a significant increase in load carrying capacity for girders within a composite bridge section. A simple yet effective 1-D model was established to predict time dependent behaviors of pretensioned concrete and improvements were made to the backbone technique used for processing free vibration response data for nonlinear system identification and damage detection purposes through this project. The overall research provided important information on the structural and composite behavior of aged pre-stressed girder bridges critical to shear and on methods for identifying properties of aged members, structural health monitoring, and damage detection.

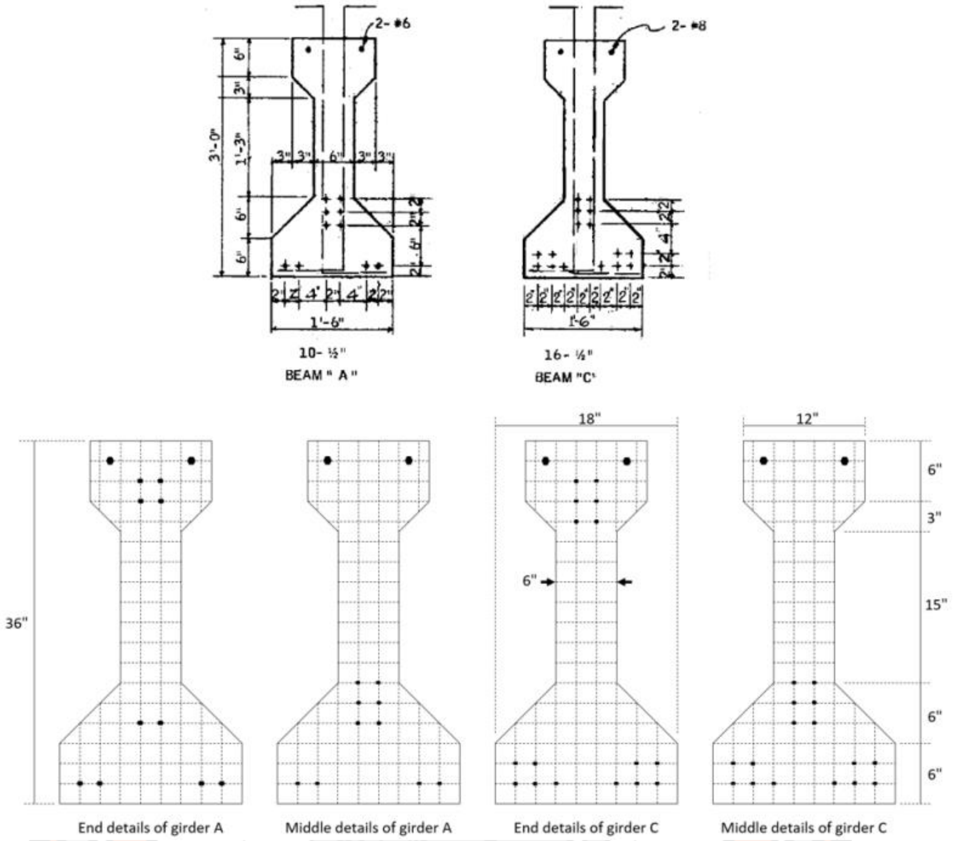

Figure 27 Two typical girder cross-sections, “A”, and “C” [34]

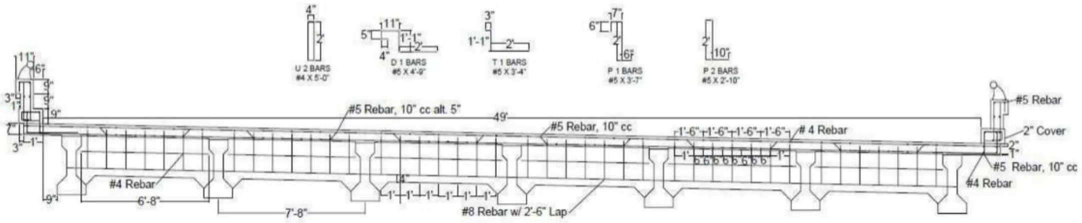

Figure 28 Whole section of the bridge section where girders A and C were taken [34]

Figure 29 Removal of girder C from the I-244 bridge over the Arkansas river in Tulsa, OK on September 4, 2013 (photo courtesy of Gary Quinonez with Manhattan Road & Bridge) [34]

Figure 30 Arrival of girders at Fears Lab on flatbed trailers on October 8, 2013 [34]

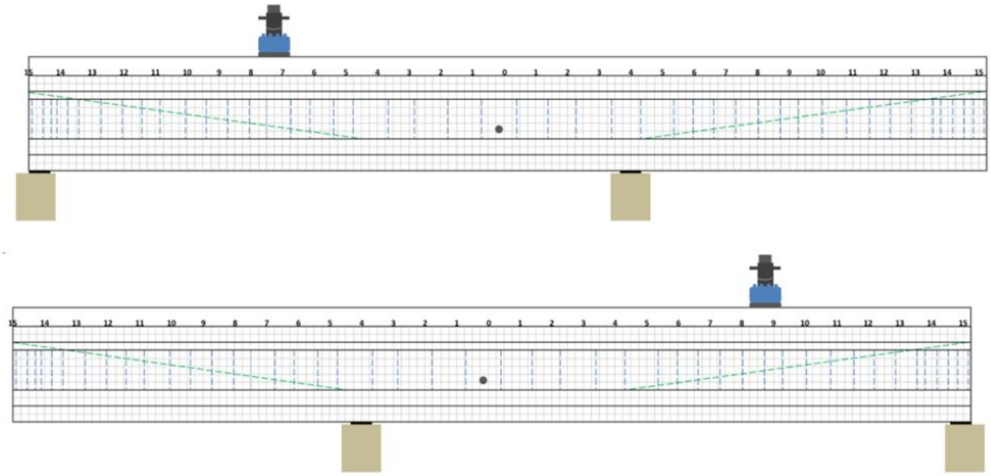

Figure 31 Overview of test setup for (top) shear test A1, and (bottom) shear test A2 [34]

Figure 32 Test C1 setup [34]

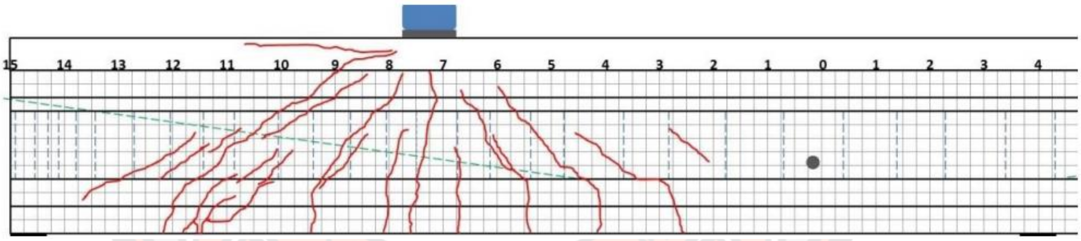

Figure 33 Shear test A1 cracking pattern [34]

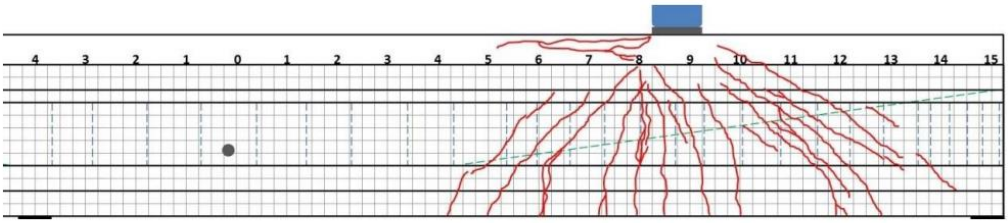

Figure 34 Shear test A2 cracking; strand rupture occurred at the 8 ft mark [34]

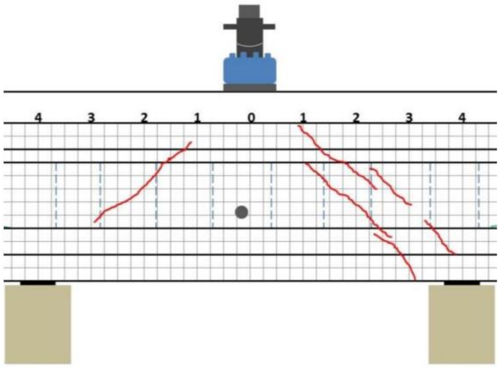

Figure 35: Cracking pattern for shear test A3 [34]

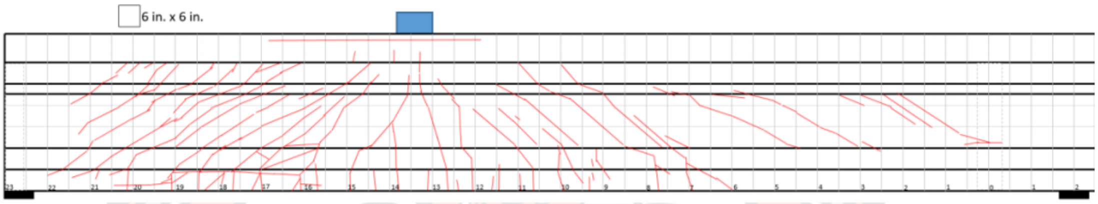

Figure 36 Test C1 cracking [34]

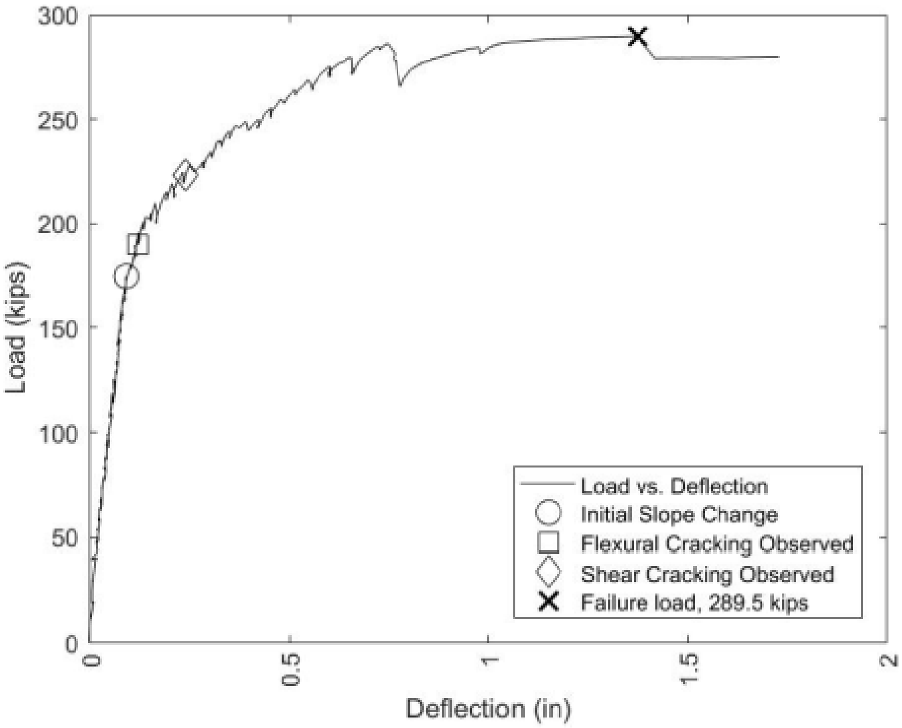

Figure 37 Load deflection plot for test A2 truncated at the failure point based on an average of the two wire pots [34]

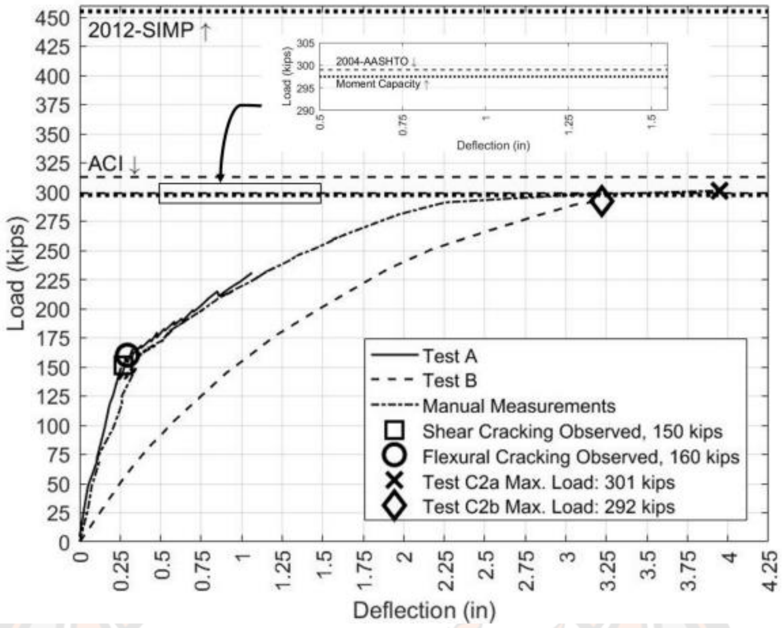

Figure 38 Load vs. deflection for test C2 [34]

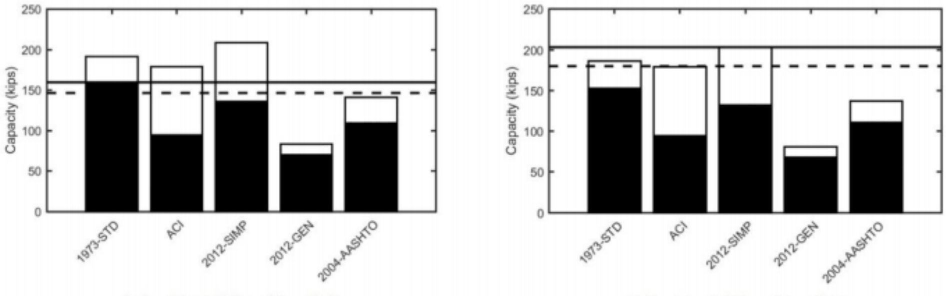

(a) Test A1: a/d = 2.5

(b) Test A2: a/d = 2.0

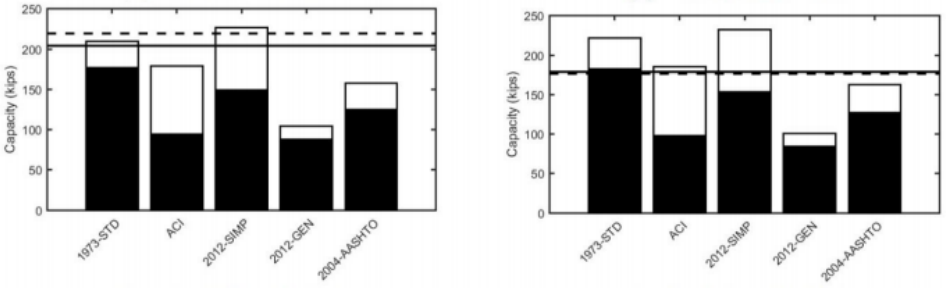

(c) Test C1: a/d = 3.0

(d) Test C2: a/d = 3.83

Figure 39 Tested capacities compared to code predictions [34]

2.2.2 Field Tests

Dymond et al. 2016 investigate the shear behavior of pre-stressed girders with both laboratory and field tests to develop recommendations for the design of pre-stressed girders. A numerical study was also performed in their study to develop finite element tools for the design of pre-stressed bridge girders. The laboratory investigation was conducted on a full sale simply supported four-girder bridge that featured a traffic barrier along one edge of the bridge a diaphragm on one end of the bridge. The bridge was subjected to a series of elastic tests used to validate the finite element modelling technique used in the study. The laboratory bridge was then loaded in the inelastic range of behavior. The presence of the traffic barrier and partial-depth end diaphragm was shown to affect the shear distribution in the elastic range of behavior. FEM results indicated that a composite traffic barrier carried shear force when the load was applied directly above the exterior girder near the traffic barrier. Finite element results investigated separately for the girder and deck indicated that the end diaphragm increased the amount of shear force in the girder near the point of applied load but decreased the amount of shear force in the girder near the end of the span. The end diaphragm did not affect the amount of shear forces in the deck near the point of applied load but increased the amount of shear forces in the deck near the end of the span.

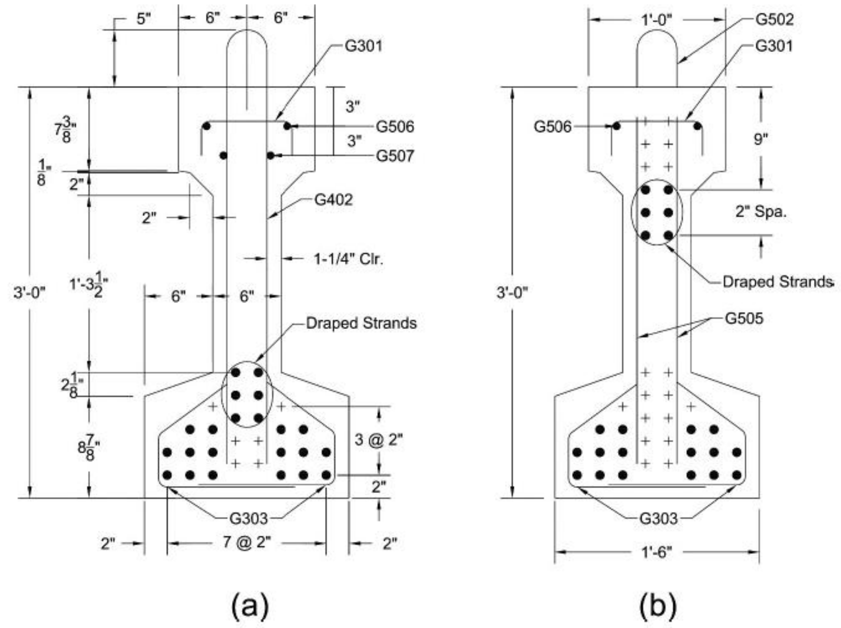

Figure 40 Laboratory bridge girder details (a) mid span and (b) end cross section details [35]

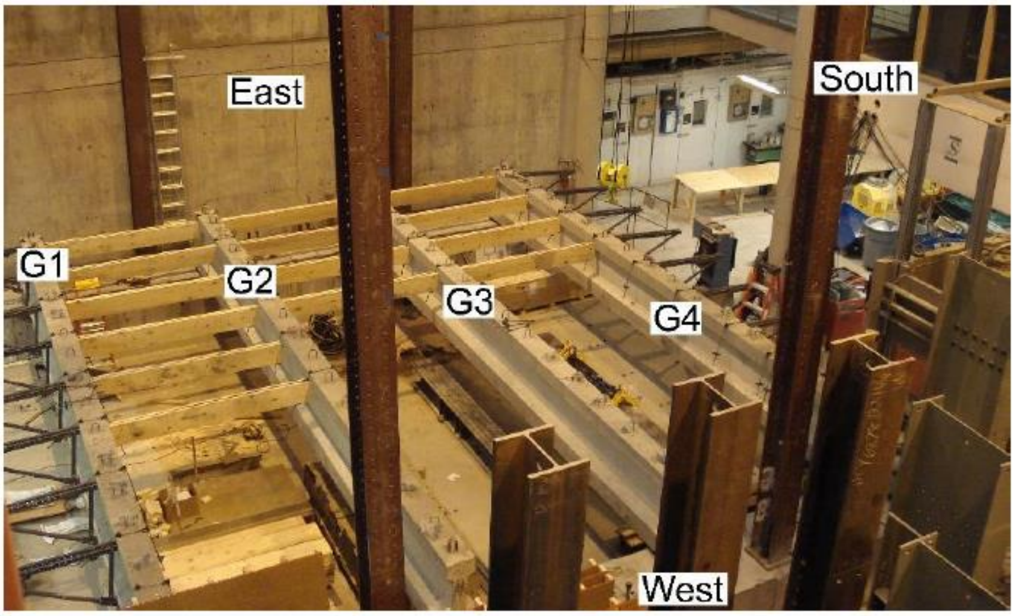

Figure 41 Laboratory bridge girder orientation [35]

Figure 42 Bridge deck placement and finishing [35]

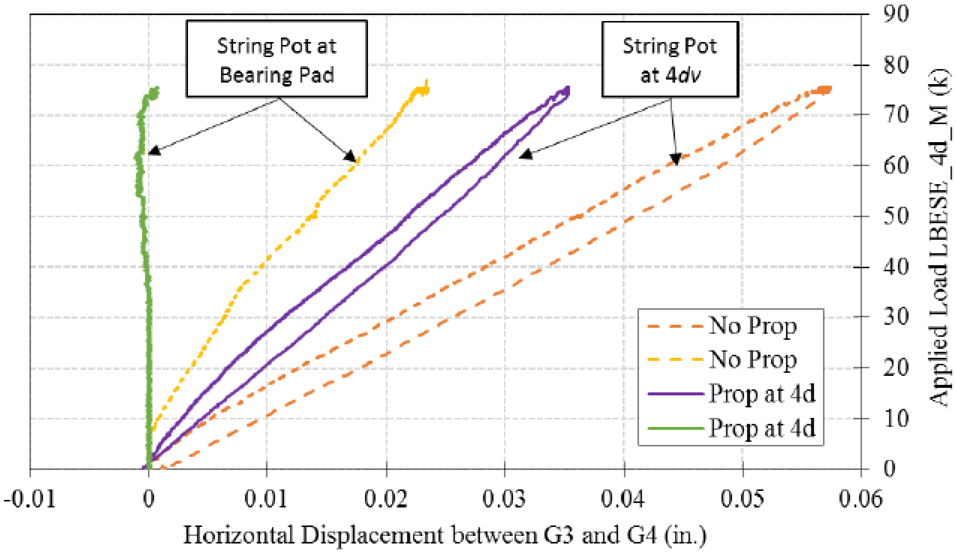

Figure 43 Influence of steel prop on girder horizontal displacement [35]

Figure 44 Web shear crushing and deck punching in G2 during LBUE looking north [35]

Bagge et al. 2018 performed full scale tests on three concrete bridges to investigate failure mode and to compare results with standard code models and advanced numerical methods. The tested bridges were, Lautajokk, a 29 year old one span (7 m) concrete trough bridge tested in fatigue to check the concrete shear capacity, Örnskldsvik, a 50 year old two span trough bridge (12 + 12 m) strengthened to avoid a bending failure, Kiruna Mine Bridge, a 55 year old five span prestressed concrete road bridge (18 + 21 + 23 + 24 + 20 m) tested in shear and bending of the beams and punching of the slab. For first bridge, the tests showed that the fatigue capacity of the bridge was much higher than what was predicted by the codes. Critical was the shear capacity in the connection of the slab to the longitudinal beams with no shear reinforcement in the slab. For second bridge, the failure was relatively ductile, Fig. 4. The recorded failure load P was 11,7 MN. For third case, In the test, the girders were first equally loaded up to total load of 12 MN, followed by increased load on the outer girder until failure at 13.4 MN. After a drop of the load, the inner girder was further loaded to failure at 12.8 MN. Extensive vertical and diagonal cracks were formed and both longitudinal non-prestressed reinforcement and vertical shear reinforcement yielded. In general, the structure behaved in a ductile manner and an appreciable residual load-carrying capacity remained after the test proving the bridge structure to be quite robust. Comparison of the test results and the analytical calculations indicates difficulties to accurately predict the load-carrying capacity [36].

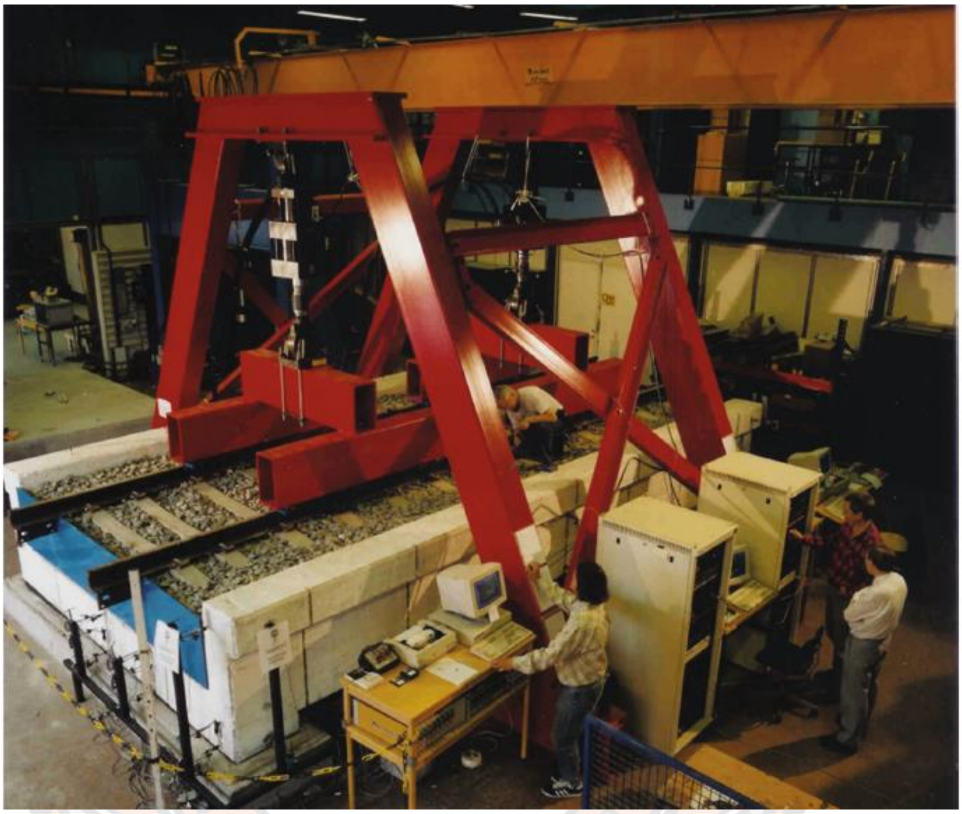

Figure 45 Full Scale Test of a 29 year old Railway Trough Bridge at Luleå University of Technology [36]

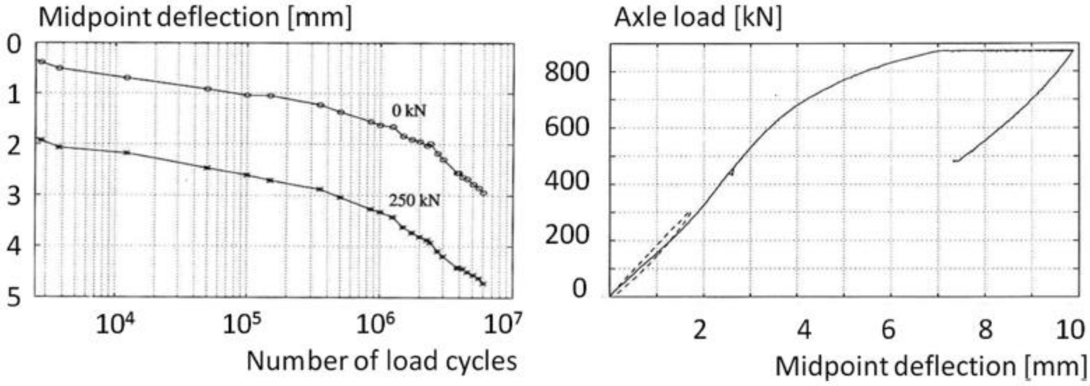

Figure 46 Mid-point deflection [36]

Figure 47 The tested railway bridge [36]

Figure 48 Photograph of the Kiruna bridge, view from north [36]

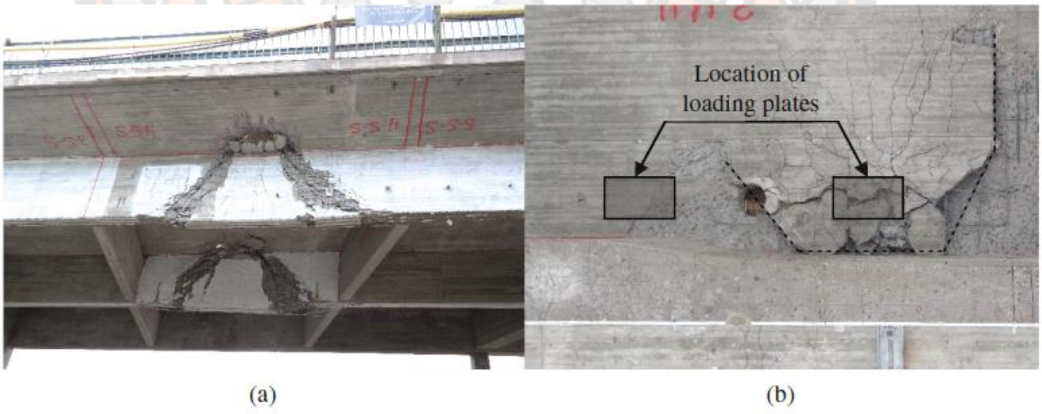

(a) (b)

Figure 49 Photograph of the Kiruna Bridge after test: (a) failure of the girders, view from south, and (b) failure of the slab, view from underneath [36]

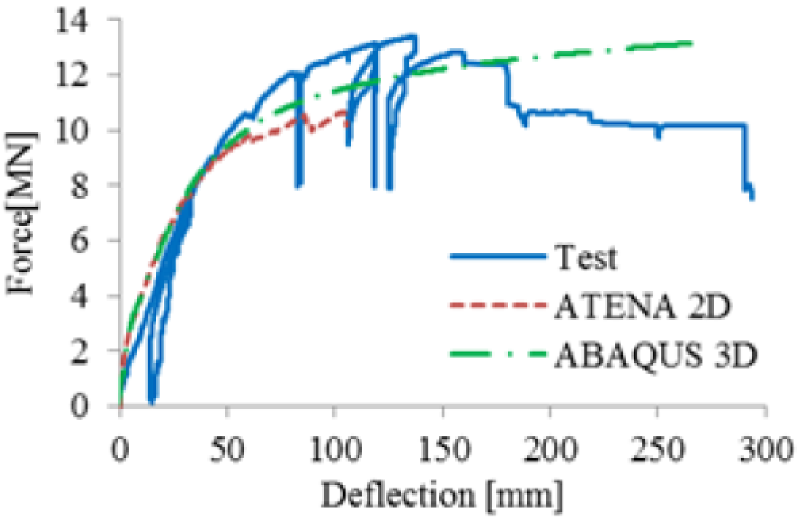

Figure 50 Load deflection curves for the failure test of bridge girders [36]

Abdel-Halim et al. 1987 investigated the overload behavior of pre-cast concrete segmental girder bridge. In their study both experimental and computer modelling was performed. One of the objectives of this research was to study the overload behavior in order to establish actual safety factors. The required loading the bridge in failure to conduction theoretical studies. An analytic procedure based on the finite element model (SAP IV) was developed to predict the complete load deformation response. The bridge was consisted of two identical simply supported girders with segments and joints. Each independent girder consisted of seventeen segments, which were tied together with longitudinal bar or strand post-tensioning tendons. The results indicate that the experimental deflections and strains at mid-span were always less than the corresponding finite element values. This indicated that the actual structure is stiffer than that predicted by theory.

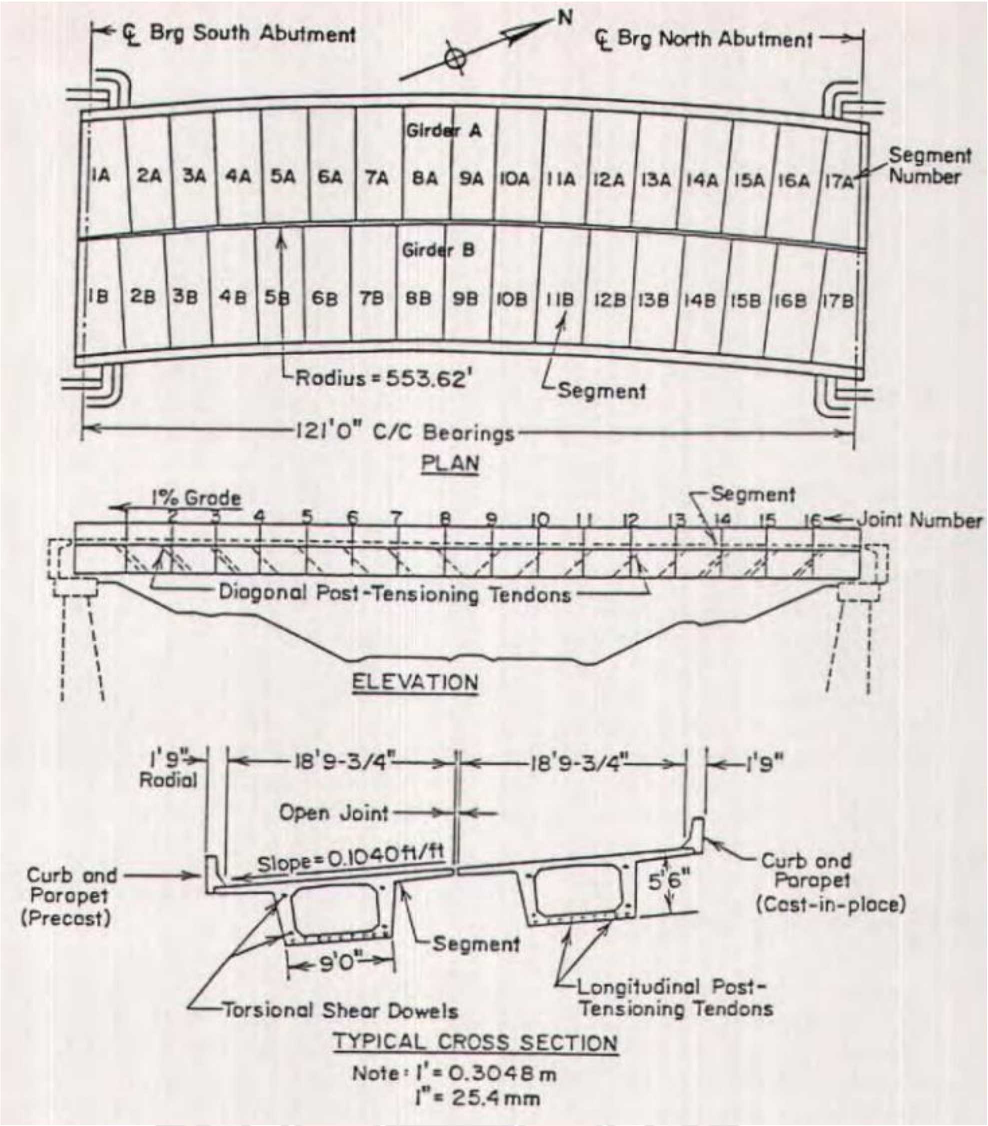

Figure 51 General plan, elevation and typical section of bridge [37]

Figure 52 Loading setup [37]

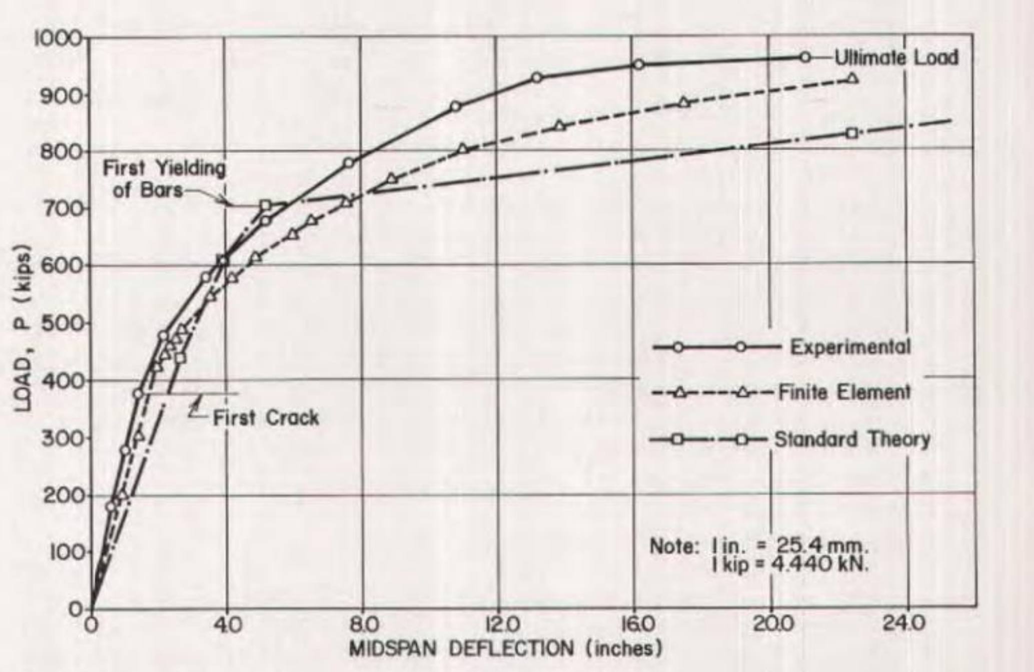

Figure 53 Load-deflection diagram of girder B [37]

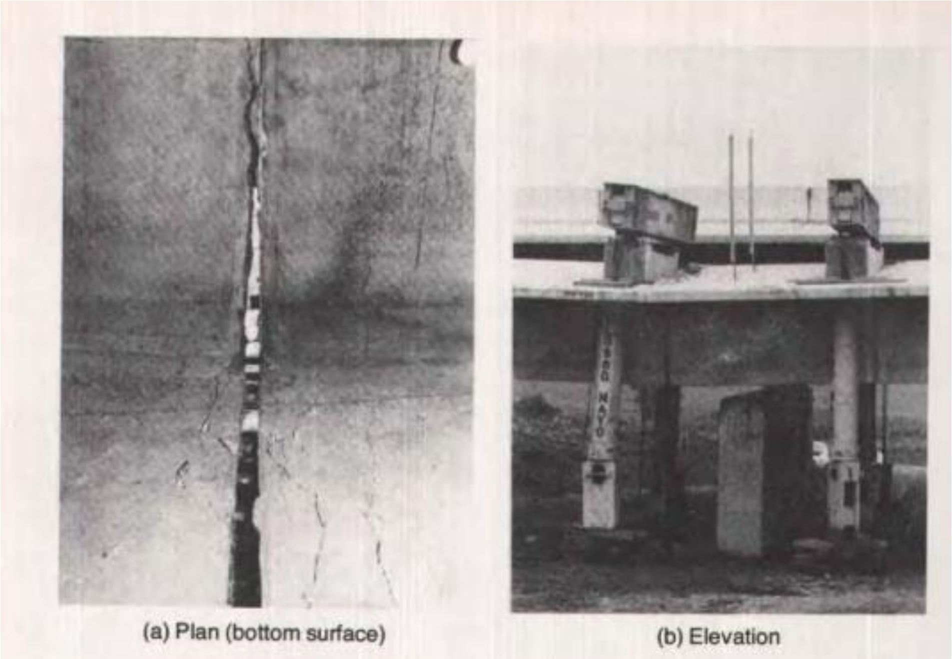
(a) Plan (bottom surface)
(b) Elevation

Figure 54 Failure mode of bridge [37]

Takebayashi et al. 1994 performed experimental investigation of the behaviour of precast segmental box girder bridges with dry joints and external tendons. A full-scale 45 m deck was erected for the test, and instruments were set up to monitor the deformation characteristics-such as deflection, joint opening, tendon slip at deviators, concrete and tendon strains-of the structure at various load stages.

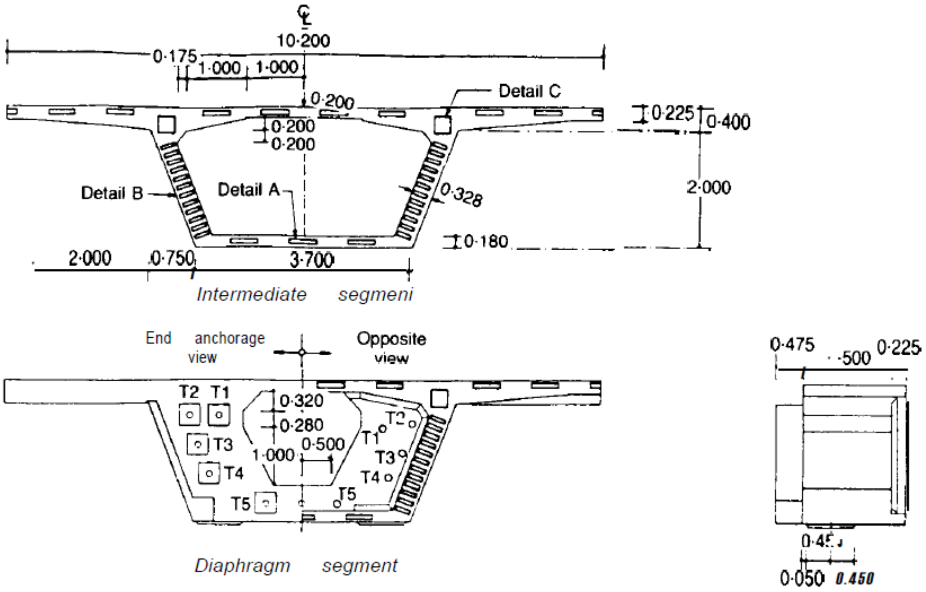

Figure 55 Details of segments [38]

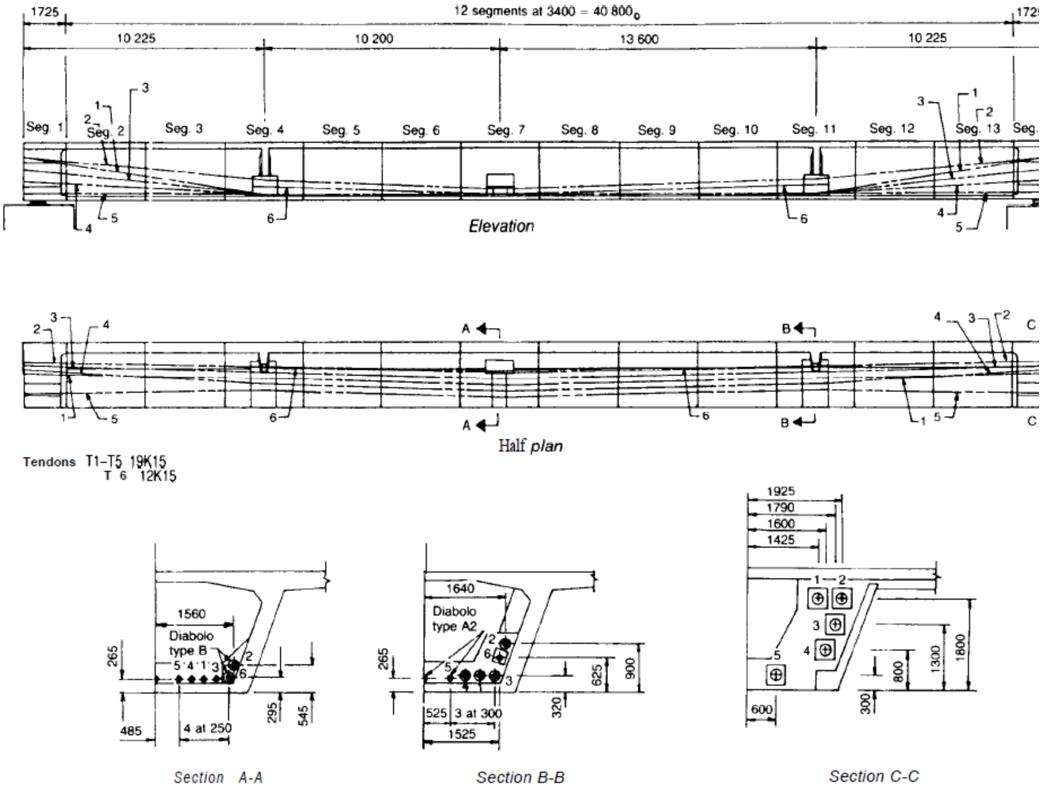

Figure 56 Tendon layout [38]

Figure 57 Loading setup [38]

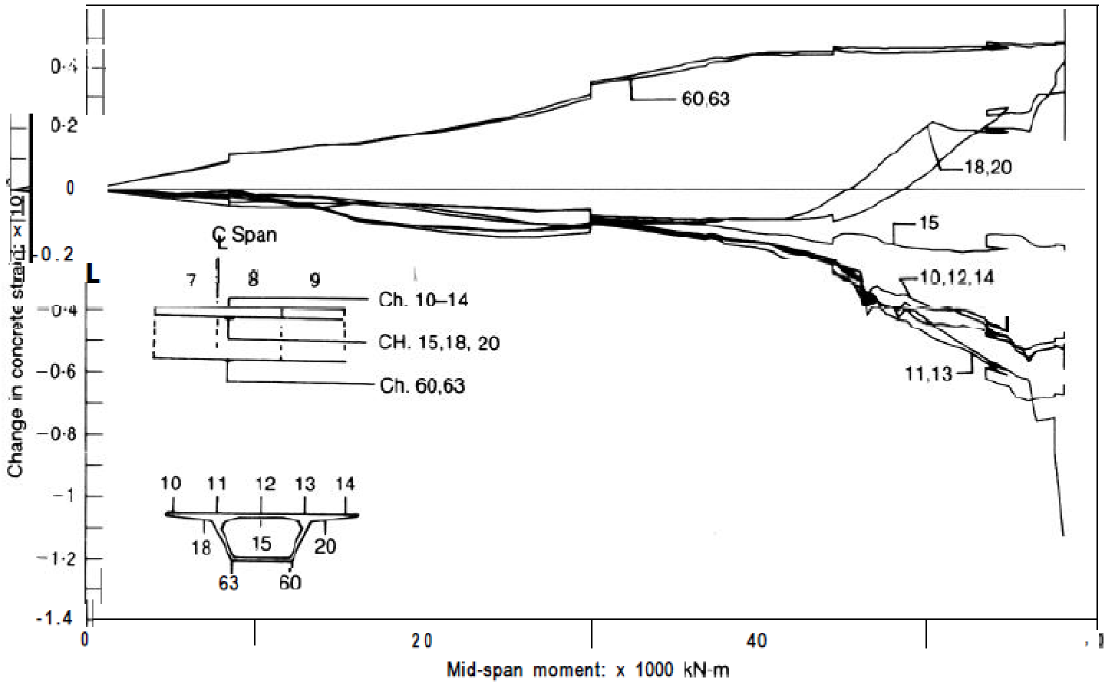

Figure 58 Experimental results [38]

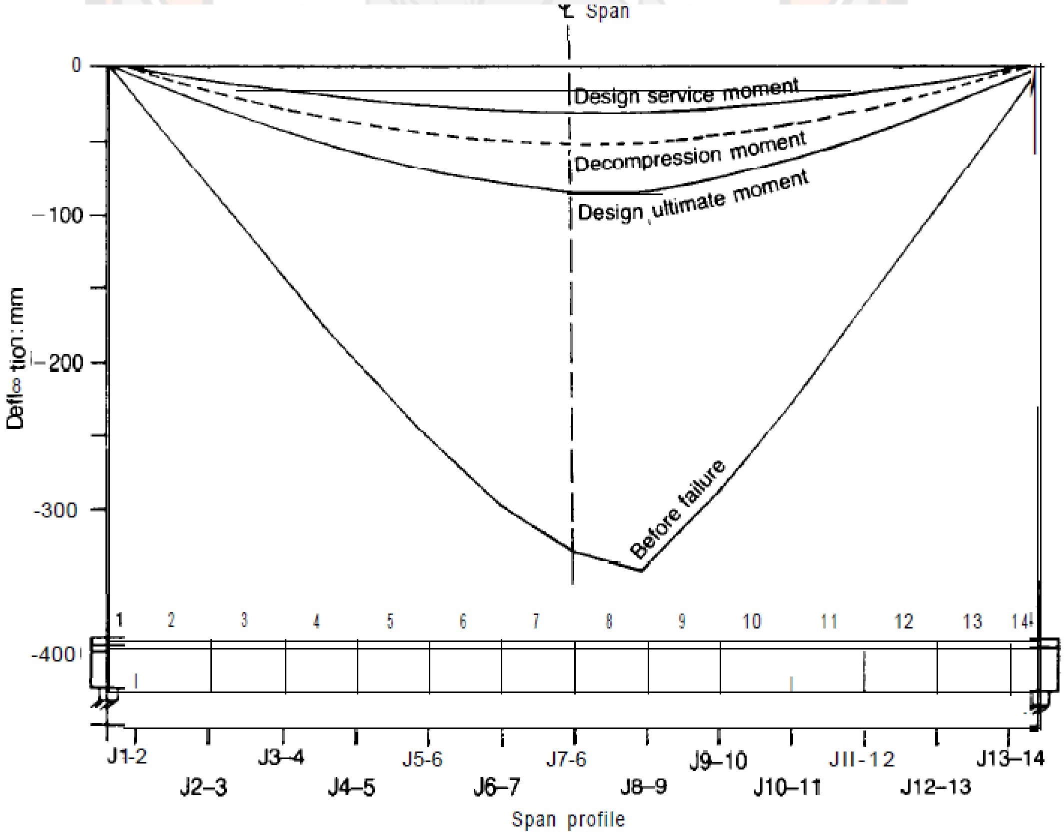

Figure 59 Deflection profile [38]

2.2.3 Finite element analysis

To date a large number of research efforts are available in the literature on the use of finite element analysis program ATEAN to simulate the structure response of reinforced concrete structures. A few of them are summarized below to highlight the main aspects of ATENA program.

Hashemi and Al-Mahaidi (2012) performed the experimental and finite element analysis of flexural behavior of FRP-strengthened RC beams using cement-based adhesives. The beam was tested under a four-point bending test with a loading span of 900 mm, and a total span of 2300 mm. In order to shed further light on the performance of the CFRP textile strengthened beams using cementitious adhesive, nonlinear finite element analysis was carried out using the software ATENA. Since the best result in the experiments was achieved by the CFRP textile strengthening scheme, the FE model was developed for this composite member only. The fracture model used in ATENA is based on the smeared crack formulation and crack band model. It employs the Rankine failure criterion and exponential softening in tension and variable shear retention factor with a rotated crack model for both the reinforced concrete and the mortar. The concrete and mortar were modeled with 2D plane stress elements with a fracture–plastic constitutive model, and the reinforcement was modeled based on discrete reinforcement for the longitudinal bars and CFRP material and smeared reinforcement for the stirrups. The authors concluded that the FE analysis showed a good consistency with experimental results, and it can be applied to other problems.

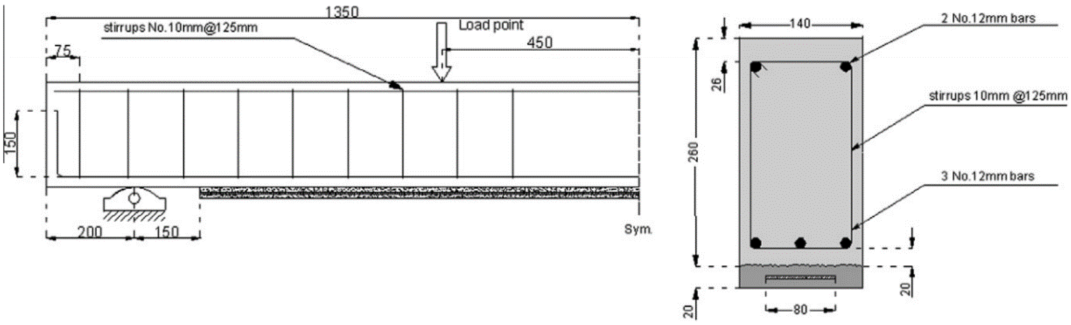

Figure 60 Details of test beams (units in mm) [39]

Table 2 Details of test beams [39]

Beam designation	No. of specimens	CFRP material	$n_f \times b_f \times t_f$[a]	Anchorage state	Bonding agent
Control	1	N/A	N/A	N/A	N/A
ESF	1	Fabric	2 × 80 × 0.176	✘	Epoxy
MSF	1	Fabric	2 × 80 × 0.176	✘	Mortar
MSR	1	Fabric	2 × 80 × 0.176	✔	Mortar
MTF	2	Textile	Equivalent FRP area to that of fabric	✓	Mortar

[a] $n_f \times b_f \times t_f$: number of layers × sheet width × thickness.

Table 3 Experimental test results [39]

Beam designation	Failure mode	Ultimate load (kN)
Control	Yielding of steel followed by secondary compression failure	121.2
ESF	Mid-span and end debond	161.7
MSF	Mid-span and end debond	132.1
MSR	Mid-span debond	138.7
MTF1	End and mid-span debond	151.9
MTF2	End and mid-span debond	155.2

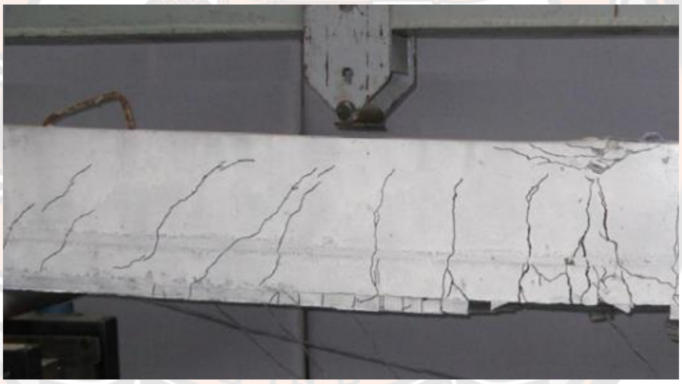

Figure 61 Typical failure mode of RC beam [39]

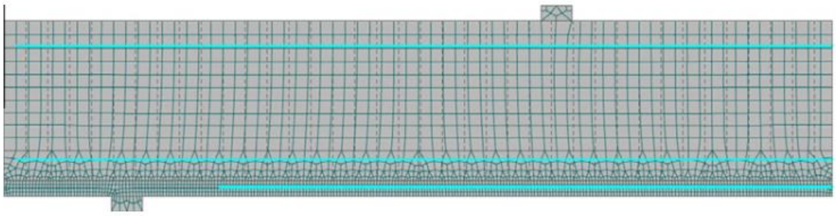

Figure 62 ATENA Finite element model [39]

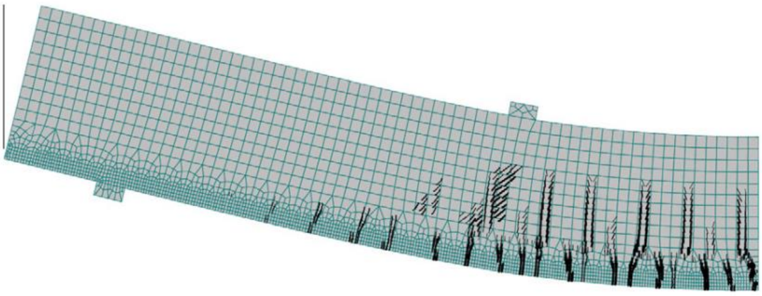

Figure 63 Crack pattern of finite element model [39]

Jendele and Cervenka (2006) conducted finite element modelling of reinforcement with bond in computer program ATENA. The purpose of this study was to add the interface model of slip to the existing set of material models, and extend the flexibility of simulation tools of reinforced concrete structures. Furthermore, the proposed method allows exploitation of the available formulas for bond slip in a rational way, whenever needed. The developed model is implemented in FEM package ATENA [40]. This is specialized software for nonlinear simulation of reinforced concrete structures. In this study, a pre-stressed panel SPIROLL manufactured by PREFA was analyzed. The panel is 3.2 m in length, 0.2 m high and 1.2 m wide. It is reinforced by 7 and 2 pre-stressed strands by along its bottom and surface, respectively. The panel was loaded by two shear forces applied approximately at 1/6 of the panel's span and was supported at a distance of 50 mm from its ends.. The slab panel was modelled and analyzed in ATENA program and different bond conditions were considered. Based on finite element analysis results, it was found that the experimentally obtained ultimate load was found about 7% higher than that calculated by the present FE model using reinforcement with strands. The overall calculated and measured failure mechanisms are quite similar [40].

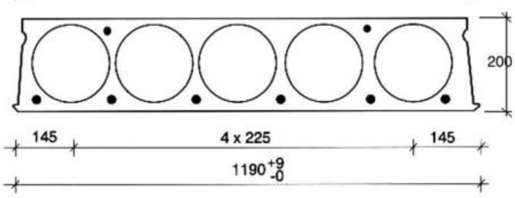

Figure 64 The pre-stressed R/C panel SPIROLL PPD 219 (units in mm) [40]

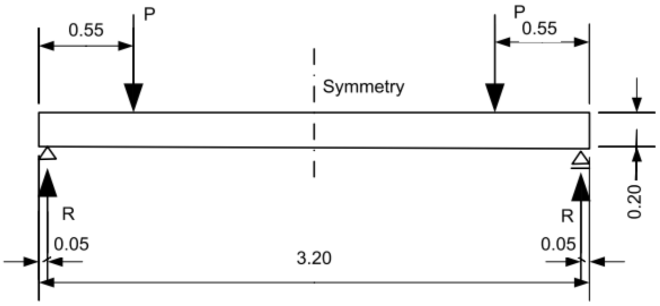

Figure 65 Static scheme of the analyzed panel–supports and loading [40]

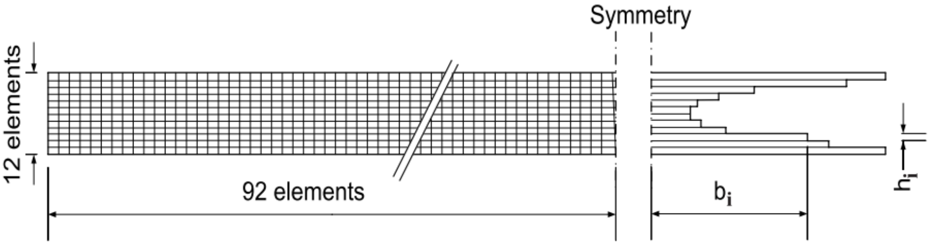

Figure 66 Finite element mesh and the model’s cross section [40]

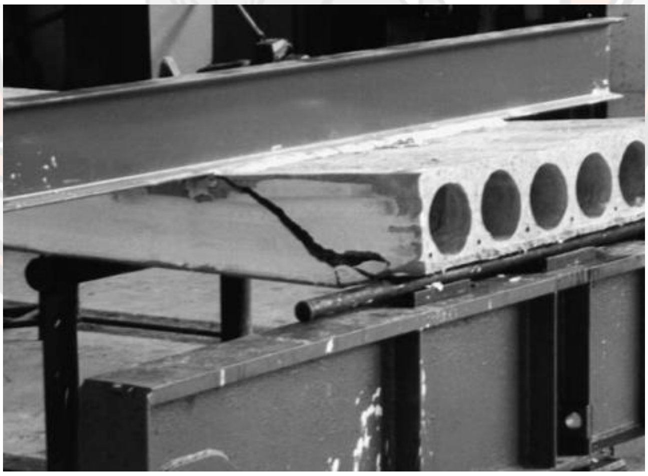

Figure 67 Cracks patterns observed in experiment [40]

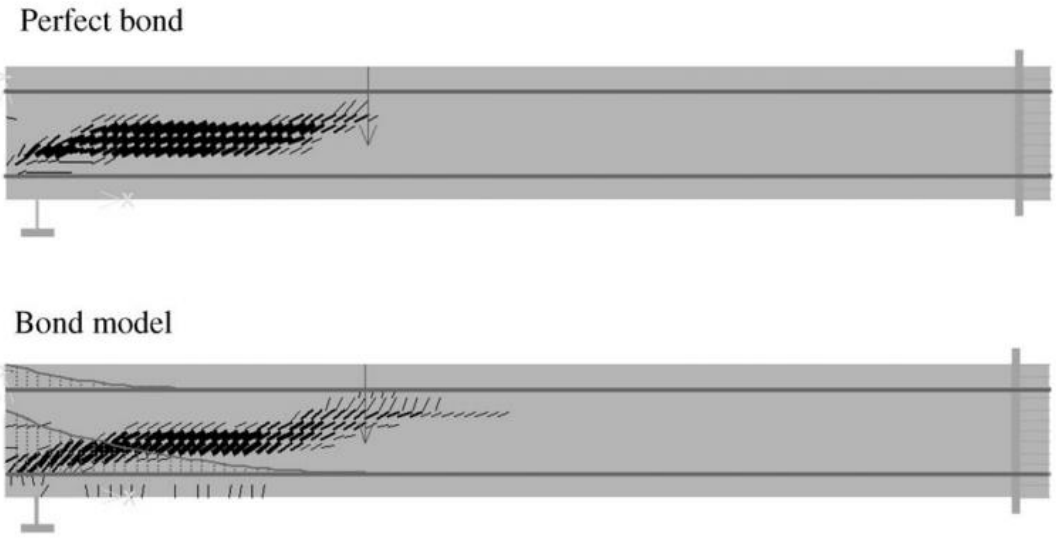

Figure 68 Cracks patterns observed in finite element analysis [40]

Jendele 2019 has conducted different studies to investigate the performance of the finite element models in ATEAN and compared the experimental results with the existing studies. Results showed a good comparison among ATENA and experimental results [20].

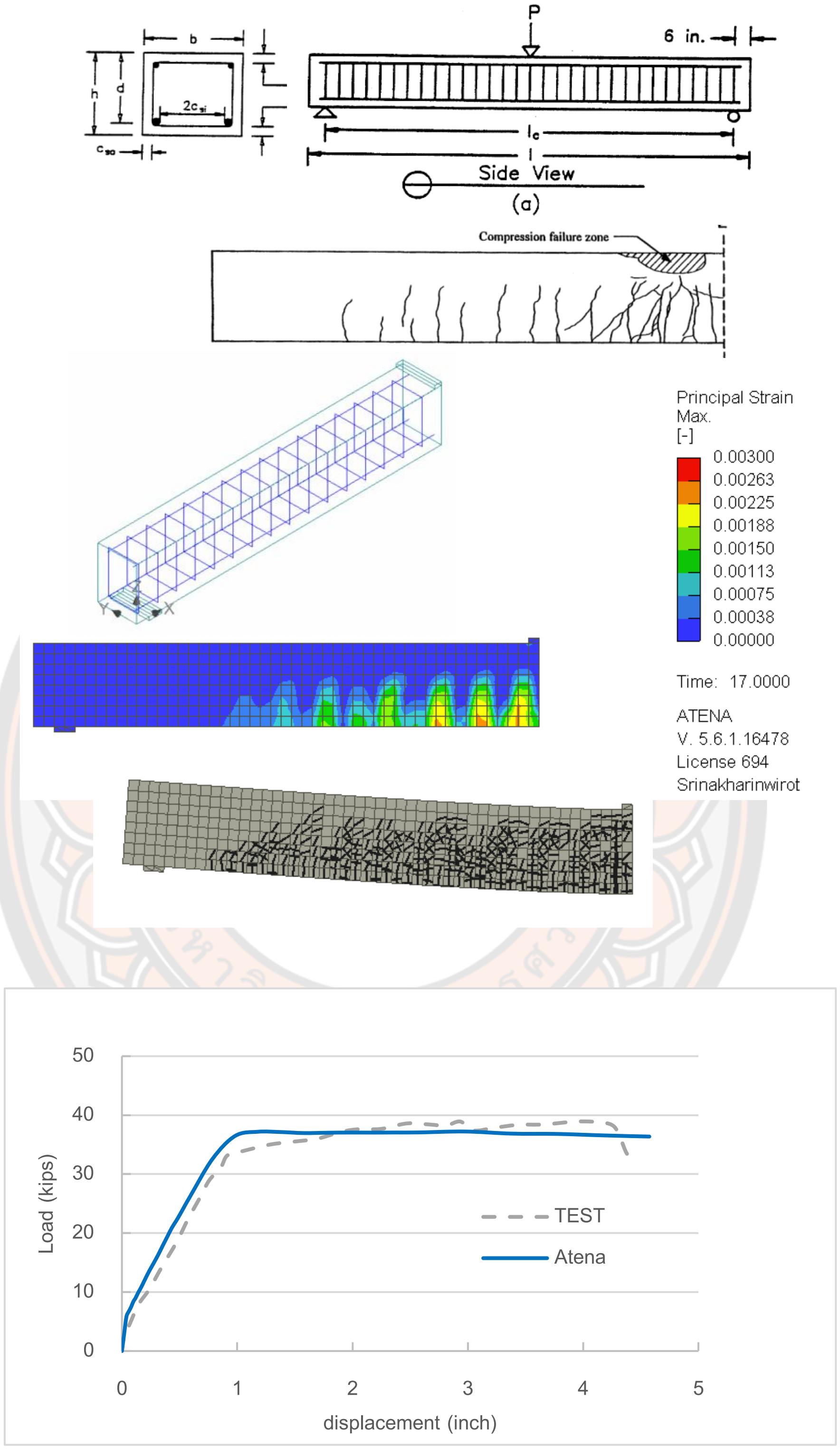

Figure 69 Comparison of FEM results with experimental results of Michael et al. 1998

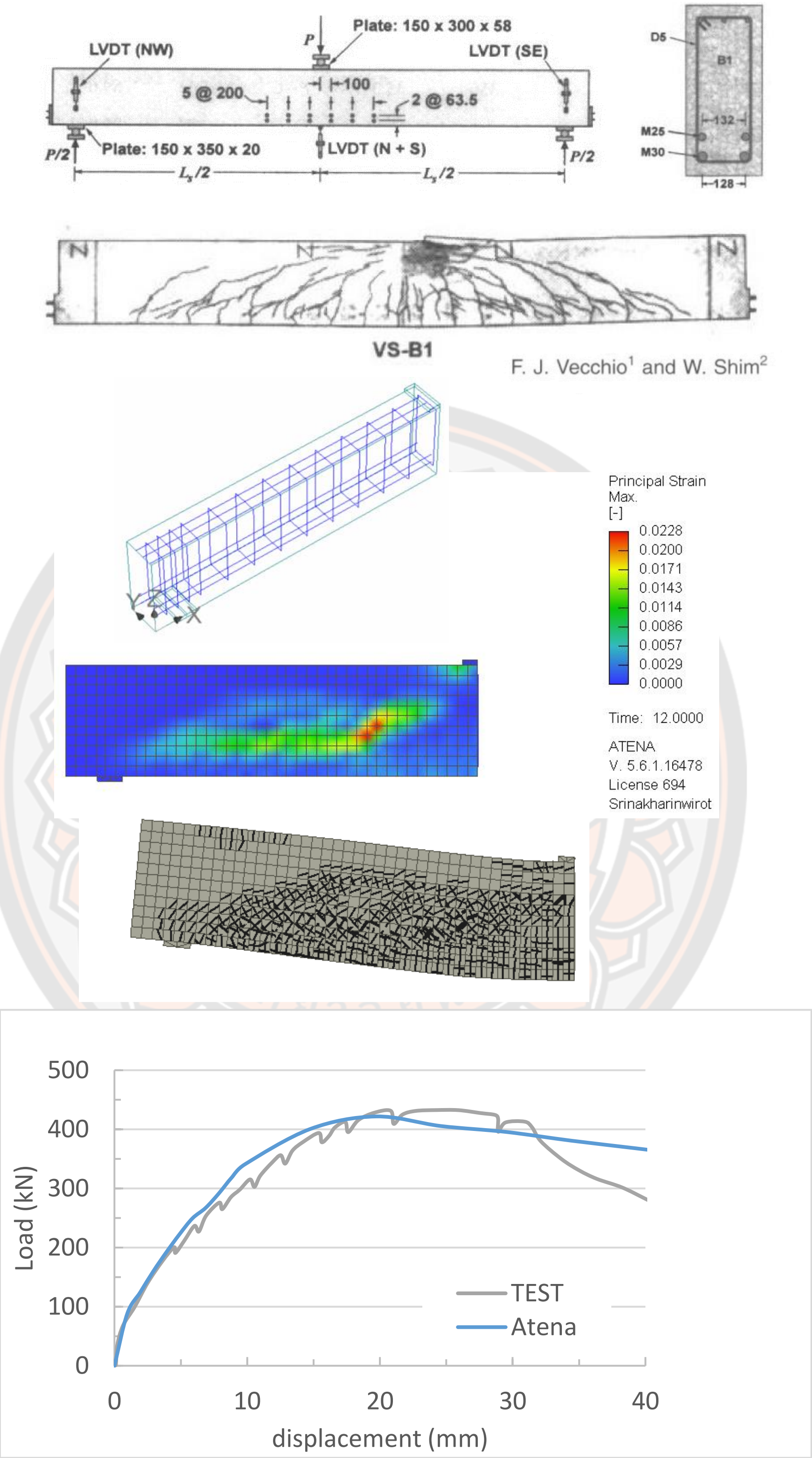

Figure 70 Comparison of FEM results with experimental results of Vecchio and Shim 2004 [41]

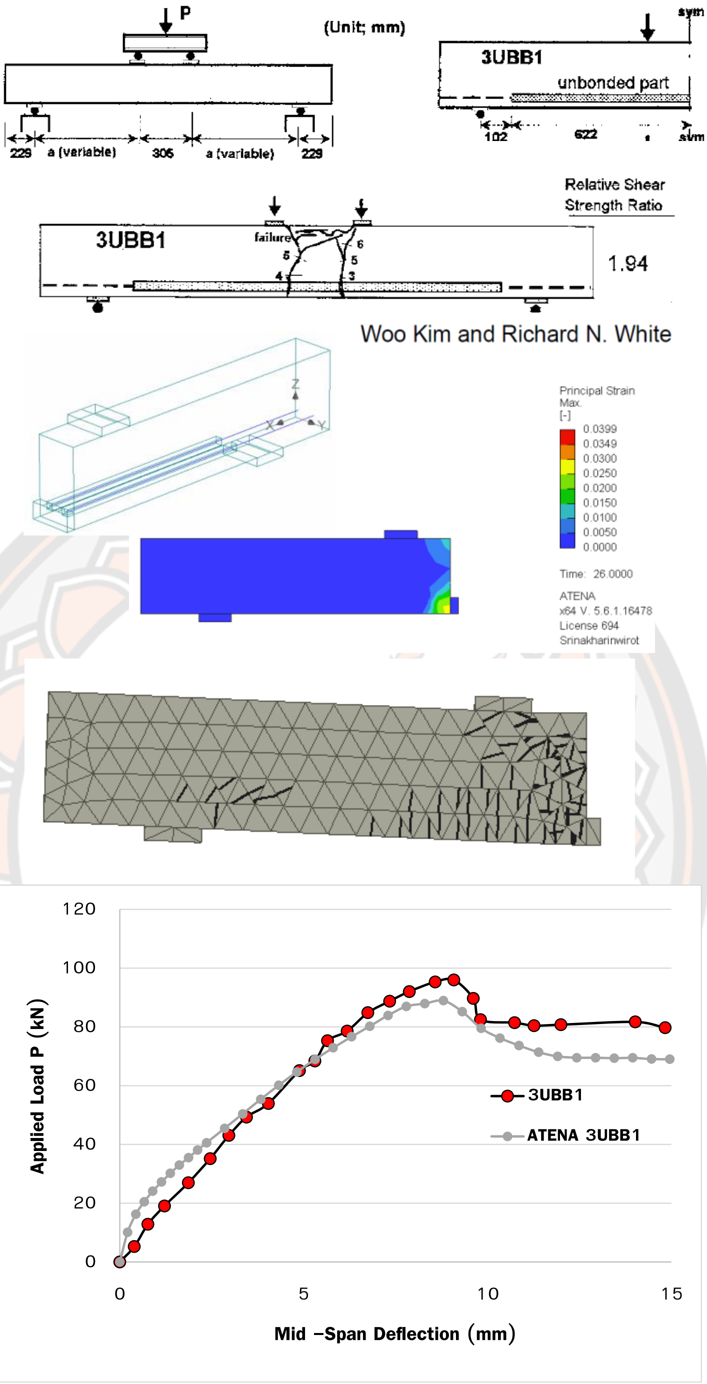

Figure 71 Comparison of FEM results with experimental results of Woo Kim et al. 1999

In another study, Chaimahawan et al. 2019 has conducted a detailed study on the analysis of the foundation in ATENA and compred the finite element results with the computer program SAFE. The results showed a good comparison among ATENA and SAFE results [42].

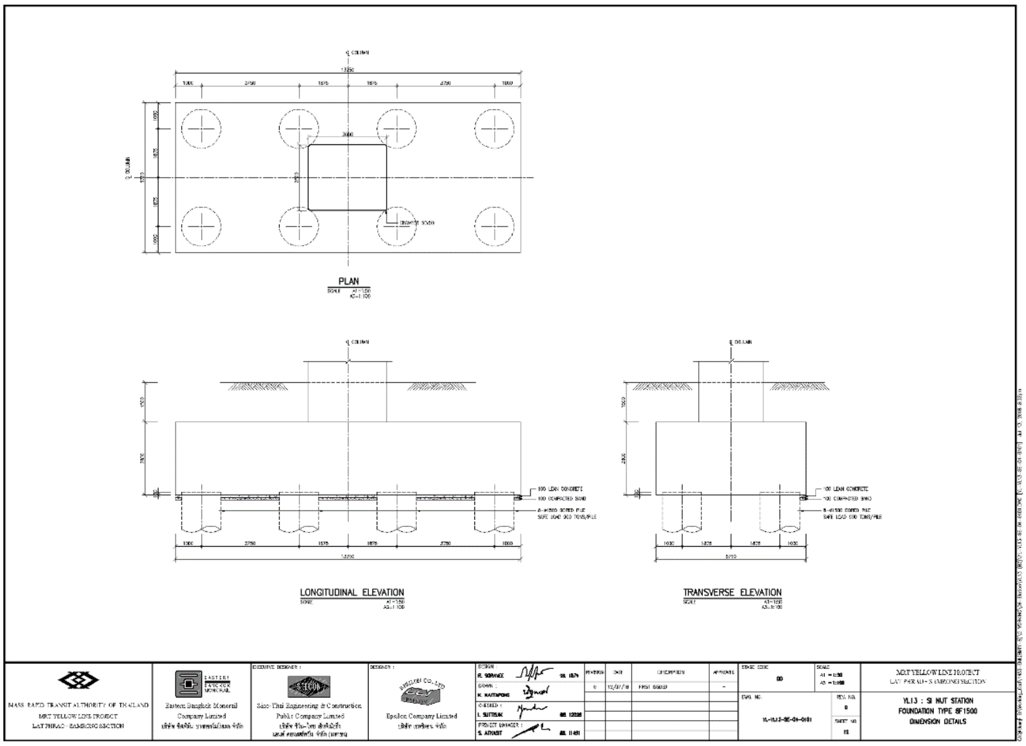

Figure 72 Details of foundation [42]

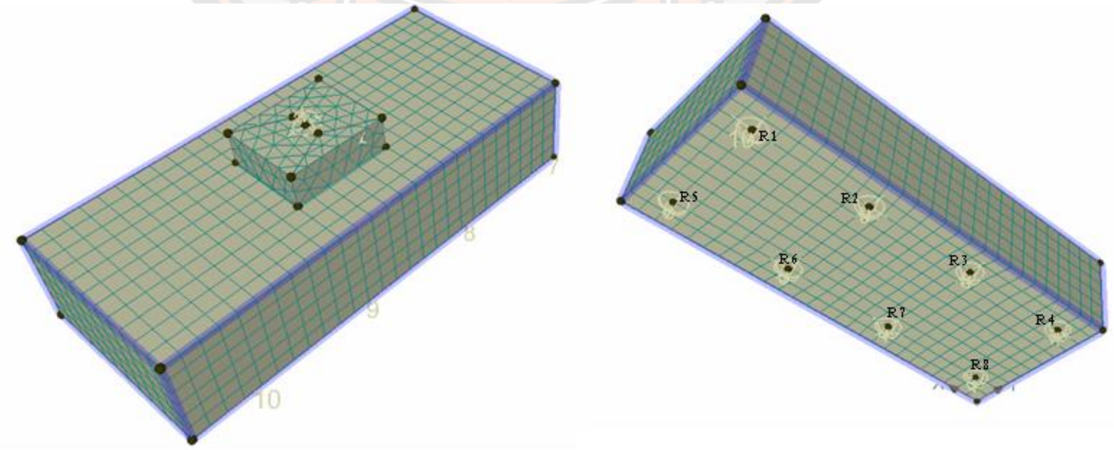

Figure 73 ATENA Finite Element Model [42]

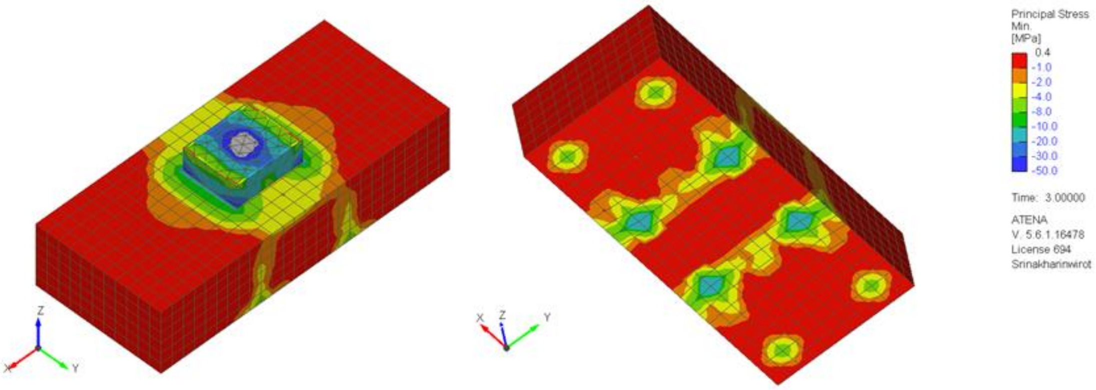

Figure 74 Stress distribution in ATENA [42]

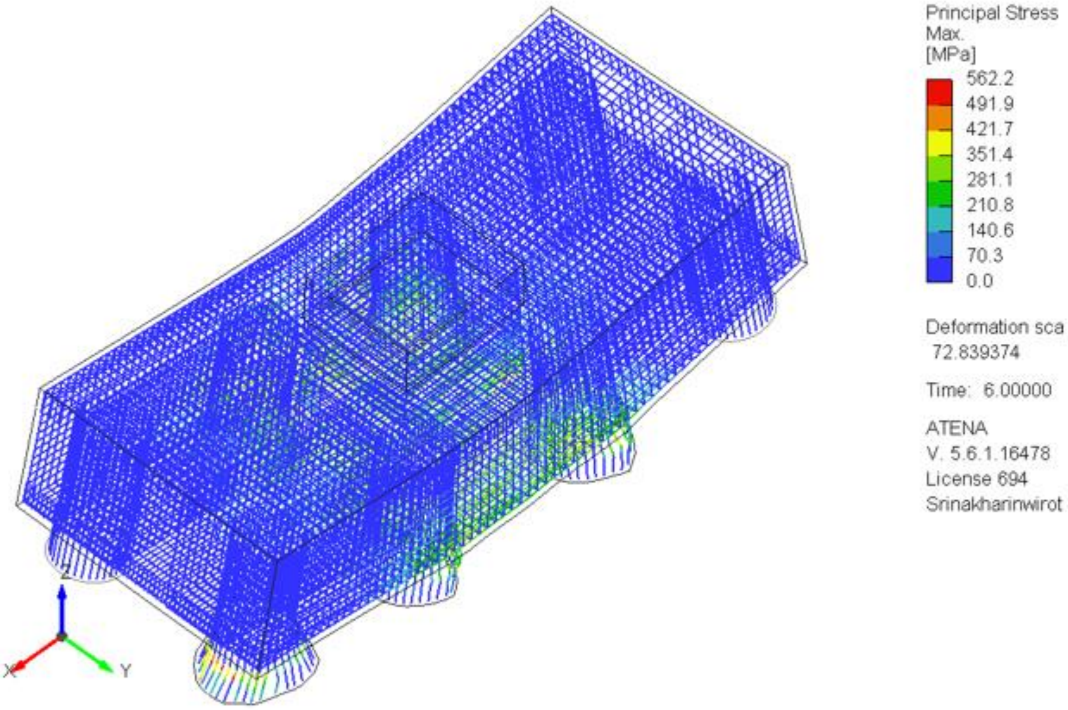

Figure 75 Stress distribution on steel bars [42]

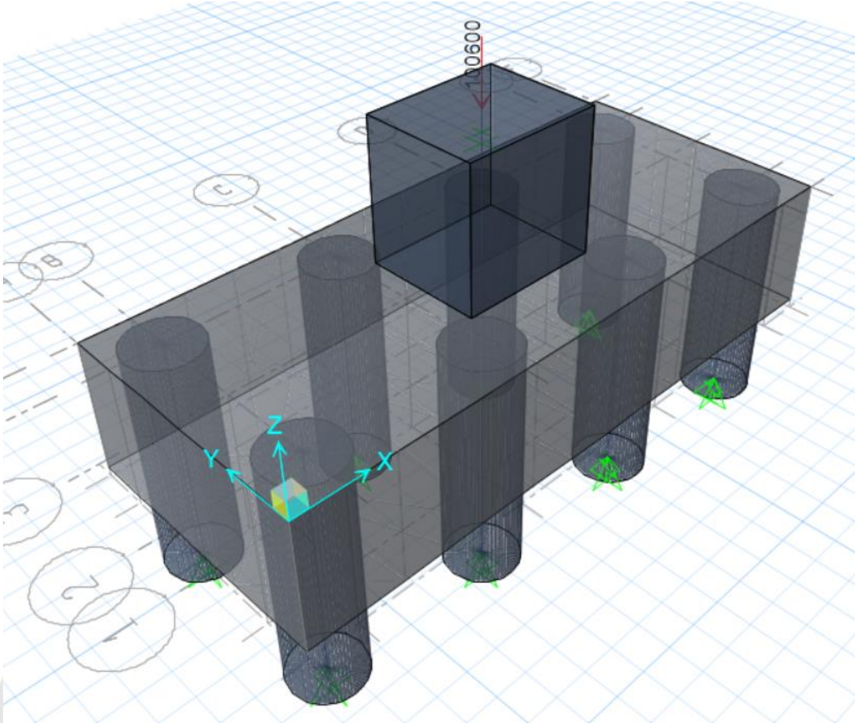

Figure 76 Finite Element Model in SAFE2 [42]

Table 4 Comparison of results [42]

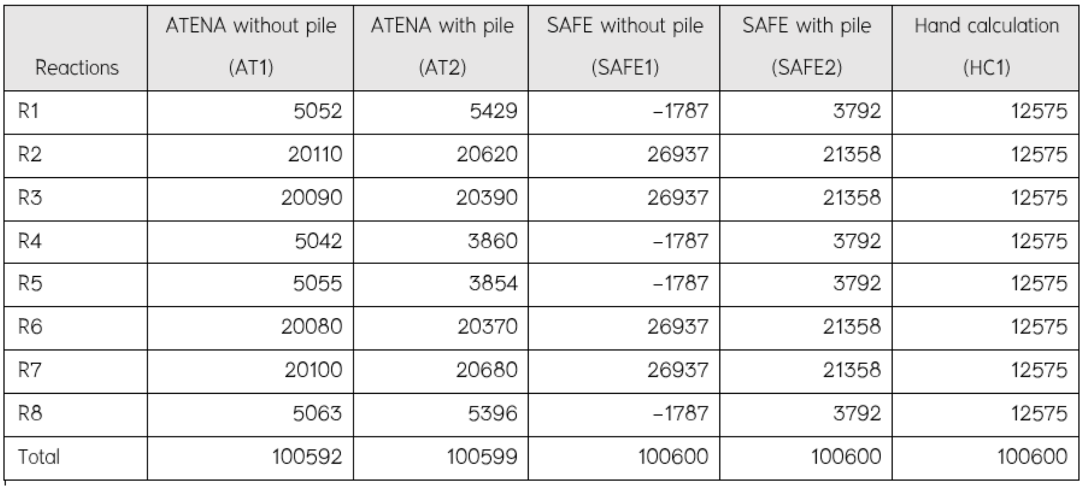

Reactions	ATENA without pile (AT1)	ATENA with pile (AT2)	SAFE without pile (SAFE1)	SAFE with pile (SAFE2)	Hand calculation (HC1)
R1	5052	5429	−1787	3792	12575
R2	20110	20620	26937	21358	12575
R3	20090	20390	26937	21358	12575
R4	5042	3860	−1787	3792	12575
R5	5055	3854	−1787	3792	12575
R6	20080	20370	26937	21358	12575
R7	20100	20680	26937	21358	12575
R8	5063	5396	−1787	3792	12575
Total	100592	100599	100600	100600	100600

2.3 Summary of literature review

The detailed review of existing research indicated that experimental response of different types of bridges and bridge girders such as pre-stressed concrete bridges, pre-stressed concrete I girder bridges and pre-stressed concrete girder bridges, have been extensively studied both in the laboratories and field environments. Some studies have also reported the performance of concrete segmental bridge technology keeping in view the sustainable bridge construction. Different researchers have also investigated the behavior of pre-stressed concrete bridges after few years of service. A few studies have also been conducted on the application of monorail bridge girders and their structural response in Japan. For the structural response of the monorail girders, small scale girders were constructed and tested in the laboratory. As per author’s knowledge, thee-span post-tension monorail girder system have not yet been used to construct the sky train system. In addition, the performance of the thee-span post-tension monorail girder system have not yet been investigated in the past. Further, different studies indicate that finite element analysis program ATENA is well capable to predict the structural responses of the reinforced concrete members which can be effectively used to study the behavior of the proposed system in this study.

Chapter III

Methodology

3.1 Part A: Large-scale Experimental Program

3.1.1 Construction details of the Monorail bridge girder

The characteristic details of the newly proposed Full-scale Precast Post-tensioned Continuous (FPPC) Girder for straddle monorail are shown in Fig. 77. The investigated FPPC Girder represents the actual size, design and construction of a monorail transit system (Yellow and Pink Line Monorail Projects) in Bangkok, Thailand. The FPPC girder is mainly comprised of three reinforced concrete (RC) hollow haunched girders (one interior and two exterior girders), four piers or supports, two pier segments, four wet joints and four bearings at each support, as shown in Fig. 77. A total of three spans, i.e. right exterior span, middle span and left exterior span were considered to construct the FPPC girder. The length of the exterior spans was 30.65 m and the length of the interior span was 31.40 m. The construction details for both right and left exterior girders were identical, as shown in Fig. 78. The total length of the exterior girders was 29.95 meters. The width and height of the exterior girder at the ends were 690 mm and 2000 mm, respectively. The width and height of the exterior girder at the middle were 690 and 160 mm, respectively. The size of the hollow opening at the middle of the right exterior girder was 270 x 1100 mm (width x height). The construction details for the interior girder are shown in the Fig. 78b. The total length of the interior girder was 30.0 m. The sectional details, such as the width and height of the interior girder, were identical to the exterior girders. Both the interior and exterior girders were supported at the intermediate piers or supported through wet joints and pier segments, as shown in Fig. 78. However, exterior girders were directly placed at the external piers or supports. The size of pre-cast pier segment was 1000 x 690 x 2000 mm (length x width x height), as shown in Fig. 79 (a) and Fig. 79 (b). Special shear keys were provided at the face of the pier segments to enhance the bond strength between the wet joint and pier segments, as shown in Fig. 79(c). Further, the space between the pier segments and bridge girders was filled with high strength non-shrink cement grout. This connection is referred to as a wet joint in this study. The length of the wet joint was 20 cm. The width and depth of wet joints were kept equal to the size of adjacent girders. A total of four piers or supports were constructed to support the pier segments and RC hollow haunched girders. A special system or bearing was designed to connect the pier segment with the bridge pier, as shown in Fig. 80. Deformed bars (DB) were used for all components such as girders, bridge piers and pier segments. The details for the reinforcing bars of the girder and pier segments are shown in Fig. 81.

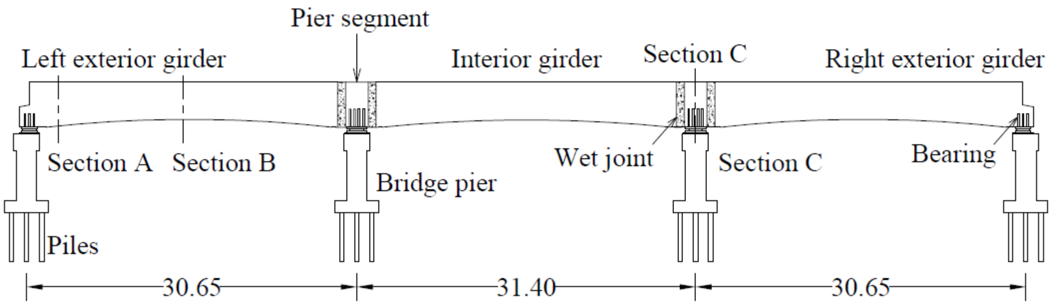

Figure 77 Typical details of the FPPC girder (units: meters).

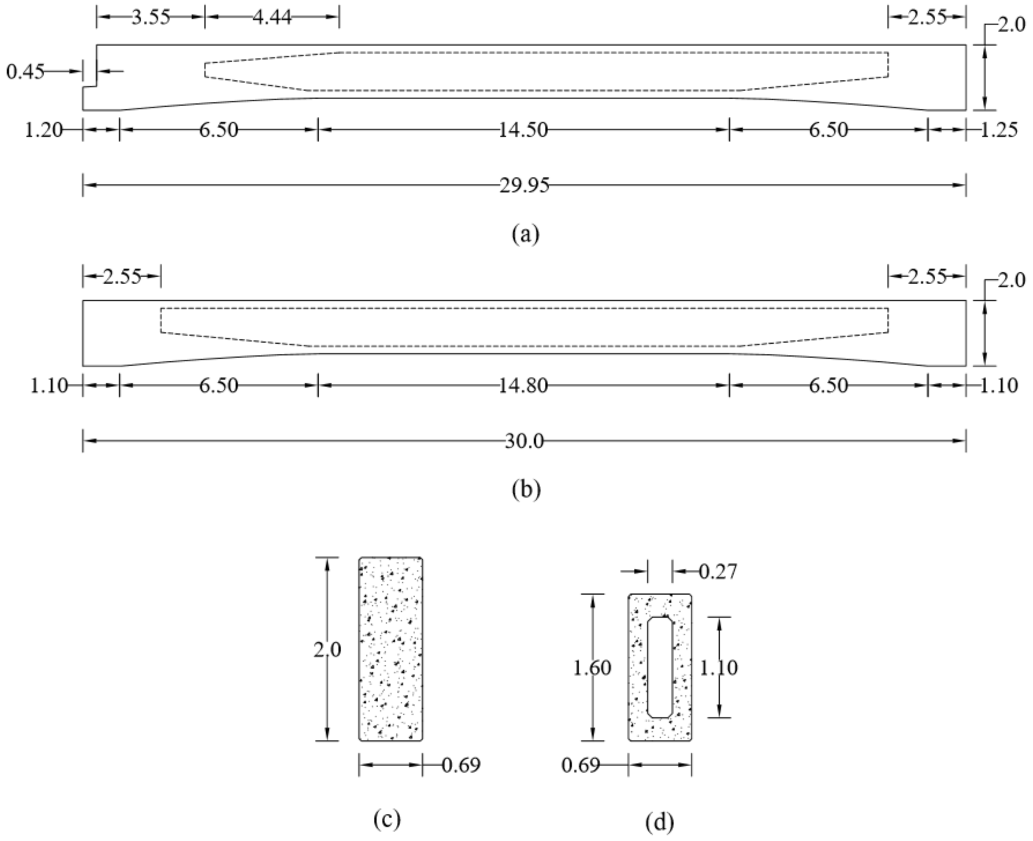

Figure 78 Dimensional details of precast girders (a) exterior girder, (b) interior girder, (c) end section, and (d) middle section (units in metres).

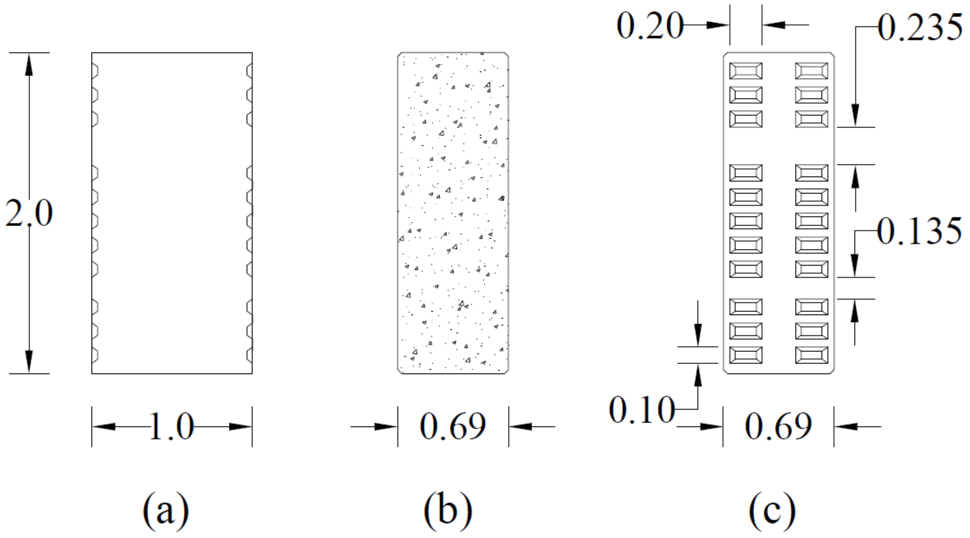

Figure 79 Details of pier segment (a) longitudinal section, (b) cross section, and (c) right\left end view (units in metres).

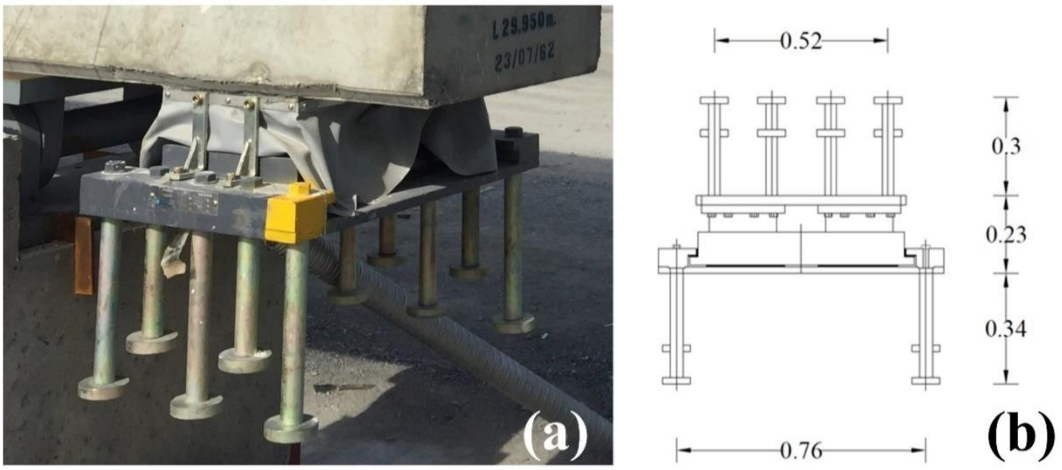

Figure 80 Typical details of end bearing (a) Typical view of end bearing, and (b) Typical details of end bearing.

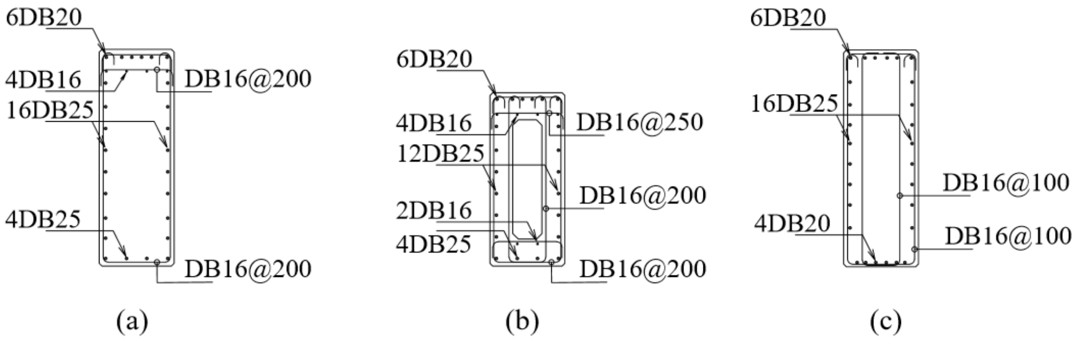

Figure 81 Reinforcement details (a) girder section at the end, (b) girder section at the middle, and (c) pier segment section.

3.1.2 Details of post-tension tendons

In this study, the FPPC girder was constructed in such a way that four post-tension tendons (T1, T2, T3 and T4) were passed through all three girders (right and left exterior girders and interior girder) and pier segments to develop the three-span continuous post-tension girder, as shown in Fig. 82. In addition to the continuous tendons, short-length post-tension tendons (T5 and T6) were also provided at the pier segments to connect the exterior and interior girders, as shown in Fig. 82. Short-length post-tension tendons were provided to resist negative moments at the continuous supports. Special-purpose steel plates and grips were used to hold the post-tension tendons, as shown in Fig. 83.

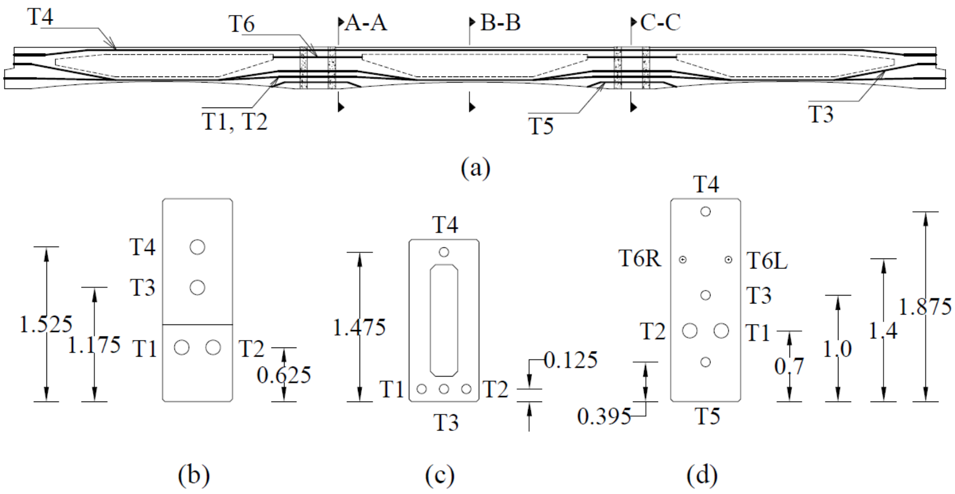

Figure 82 Details of posttension tendons: (a) geometry and reinforcement layout of the test-structures, (b) section at A-A, (c) section at B-B, and (d) section at C-C.

Figure 83 Typical post-tensioning of the FPPC girder.

The tensioning of the continuous tendons T1, T2, T3 and T4 were performed at the right extreme ends. Whereas, the tensioning of short tendons i.e., T5 and T6 were performed through special purpose ducts which were provided at the front, back and bottom sides as shown in Fig. 84.

(a) Front view

(b) Bottom view

Figure 84 Special purpose ducts, a) at front side and b) at bottom side

3.1.3 Material properties

In this study, high strength (HS) ready-made concrete was used to construct the exterior and interior girders, pier segments and piers or supports. Standard cylindrical specimens of size 150 mm diameter and 300 mm height were cast and tested to determine the compressive strength of concrete. Meanwhile, special-purpose non-shrink cement grout was used for the construction of wet joints to minimize the cracking and crushing of the concrete. The mix components of concrete are given in Table 5, while the average values for the compressive strength and tensile strength of concrete at the testing age are given in Table 6 for each component of the FPPC girder. Deformed steel bars (DB) were used for longitudinal and transverse reinforcement in all components. Three samples of each size were tested following ASTM A615 standards [43] to obtain the mechanical properties, such as yield and ultimate tensile strength. Seven-wire strands were used for the post-tensioning of the three-span post-tensioned girder. Five samples of seven-wire strands were tested following ASTM A416 standards [44] to obtain the mechanical properties, such as yield and ultimate tensile strength. The mechanical properties of both deformed steel bars and seven-wire strands are given in Table 7. A special kind of cement grout was used to fill the post-tensioning ducts. The compressive and tensile strength of cement grout were determined by essential guidelines of ASTM standards C109 [45] and C307 [46], respectively. The average compressive strength of cement grout was 45 MPa and average tensile strength of cement grout was 5.6 MPa.

Table 5 Details of concrete ingredients.

Ingredients	Cement	Aggregates		Water
		Fine	Coarse	
Quantity (kg/m^3)	380	710	1,100	210

Table 6 Average compressive strength of components FPPC girder.

Components	Compressive strength (MPa)	Tensile strength (MPa)
Left exterior girder	65	7.1
Right exterior girder	64	6.9
Interior girder	65	7.2
Pier segments	62	6.4
Wet joint	45	5.2

Table 7 Mechanical properties of steel bars and wire strands.

Steel bars and or wire strands	Yield strength (MPa)	Ultimate tensile strength (MPa)
DB16	420.0	480.0
DB20	420.0	520.0
DB25	440.0	560.0
7-wire strand	1500.0	1800.0

3.1.4 Preparation of test specimens

The FPPC girder was constructed and tested at the casting yard of Sino-Thai Engineering and Construction Public Company Limited (STECON), located in Saraburi Province, Thailand. According to the design requirements of the interior and exterior beams, special steel formwork was prepared for the construction of the girders to achieve a non-uniform shape or haunched curve along the length. At the middle of the formwork, a bottom haunch was introduced to get the bottom arch of the beams, as shown in Fig. 85 (a). Steel reinforcement was fabricated separately to meet the design requirements, which was placed inside the steel formwork using a special crane, as shown in Fig. 85 (b). In addition, a special foam was provided in the steel reinforcement to create the inside hollow section of both the interior and exterior beams. High strength ready-made concrete was used to cast all girders. Steel formworks were removed after 12 hours of concreting the beams and continued the ambient curing for 28 days before the fabrication of a three-span FPPC girder (Fig. 86). Parallel to the beam construction, construction of the pier segments and foundations was also carried out at the casting yard. A total of four foundations were constructed to support the three-span post-tensioned girder, whereas a total of twelve foundations were constructed to support the reaction frames. All foundations were constructed by using pre-cast piles (Fig. 87(a)) and driven using a pile hammer. At the top of the driven piles, a thick concrete mat (pile cap) was constructed to transfer the load from the pier segments to the piling. In the case of the foundations for reaction frames, steel bolts were embedded in pile caps to fix the reaction frame, as shown in Fig. 87 (b). In the case of foundations of a three-span post-tensioned girder, however, a column with one-meter height was constructed at the top of pile caps to support the pier segments. After the completion of the foundation work, beams and piers were installed and aligned accurately over the column piers. Subsequently, post-tensioning was carried out after placing the continuous post tension wires through all three beams. Finally, wet joints were constructed along with the filling of the post-tension ducts. A typical view of the FPPC girder is shown in Fig. 88.

Figure 85 Construction details of the monorail girders: (a) formwork and (b) installation of the steel cage.

Figure 86 Typical monorail girders.

Figure 87 Construction details of the foundations (a) pre-cast piles foundation, and (b) pile caps.

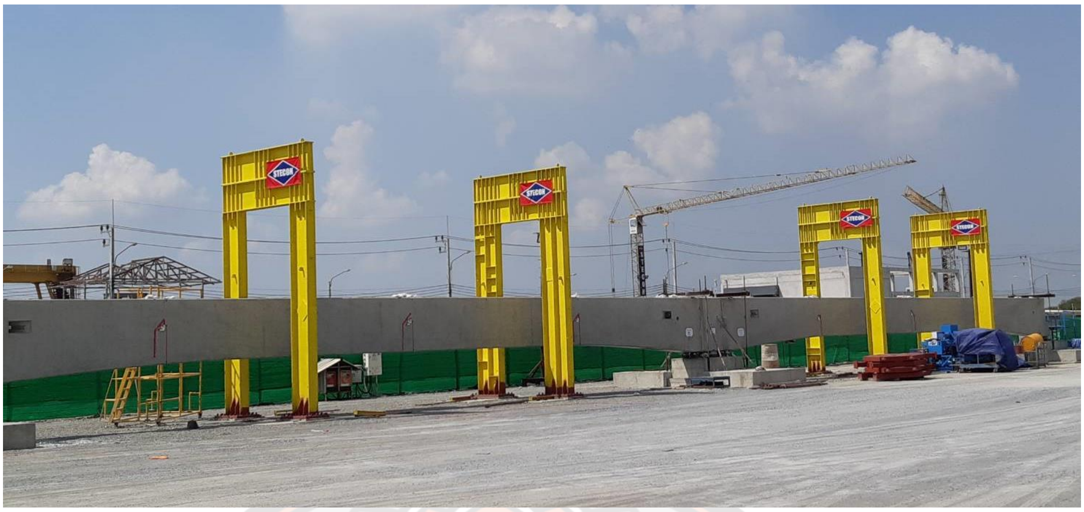

Figure 88 Typical view of the FPPC monorail bridge girder.

3.1.5 Instrumentation details

The deflection of the FPPC girder was measured by using Linear Variable Differential Transducers (LVDTs). The LVDTs were installed at different locations (Fig. 89). A total of eighteen (six for each girder) LVDTs were installed to measure the downward and or upward deflection of the interior and exterior girders. Among the six LVDTs for each girder, two of them were installed at the mid locations, two at the right side (at a distance equal to one-third of span) and two at the left side at a distance equal to one-third of the span, as shown in Fig. 89 (a) and Fig. 89 (b). Typical installation of LVDTs is shown in Fig. 90 (a). Further, a total of eight LVDTs were installed in the lateral direction at each support (2 at each support, one at top and one at bottom) to capture the out-of-plane movement of the three-span post-tension girder, as shown in Fig. 89 (c). Crack gauges were installed at different locations to determine the crack width. A total of four crack gauges (one at each wet joint) were installed to record the crack width at the location of the wet joints, as shown in Fig. 89 (a) and Fig. 89 (d). The typical installation of the crack gauge is shown in Fig. 90 (b). Also, one LVDT was installed in vertical direction on each pier to monitor the settlement of the piers as shown in Fig. 91.

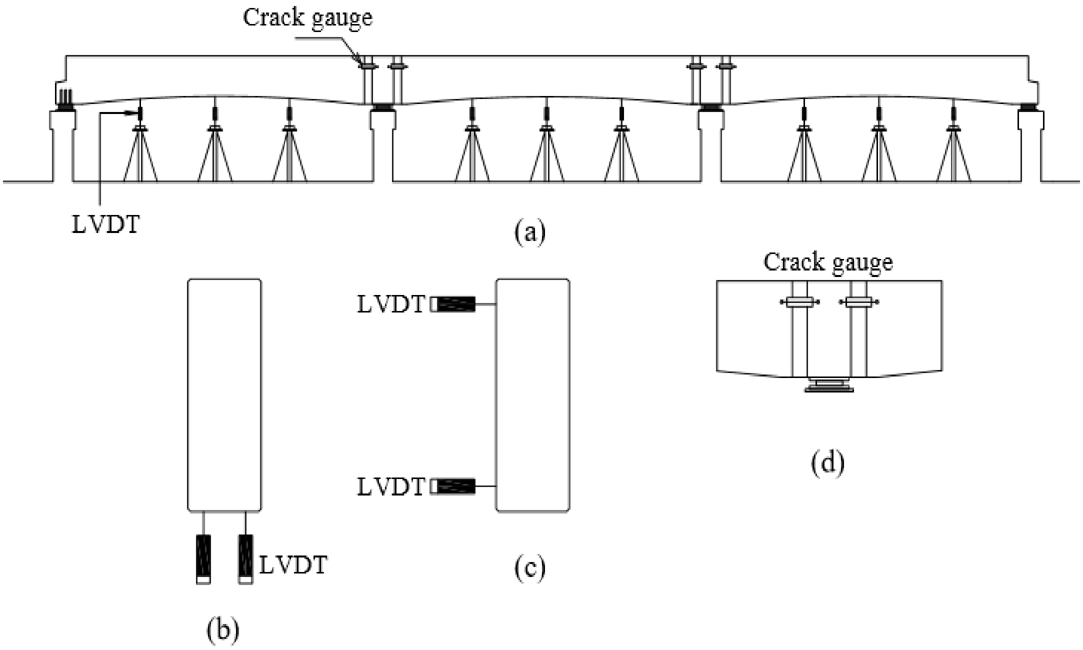

Figure 89 Typical details of LVDTs and crack gauges (a) overall display, (b) section at mid location, (c) section at pier segment, and (d) display of crack gauges.

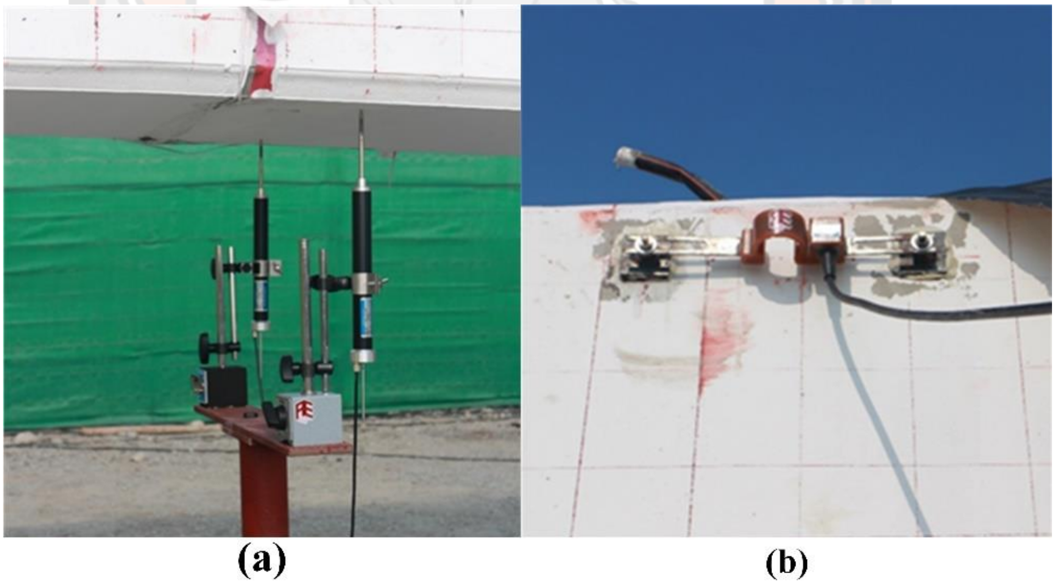
(a) (b)

Figure 90 Typical installation of LVDTs and crack gauges; (a) Installation of LVDTs and (b) Installation of crack gauges.

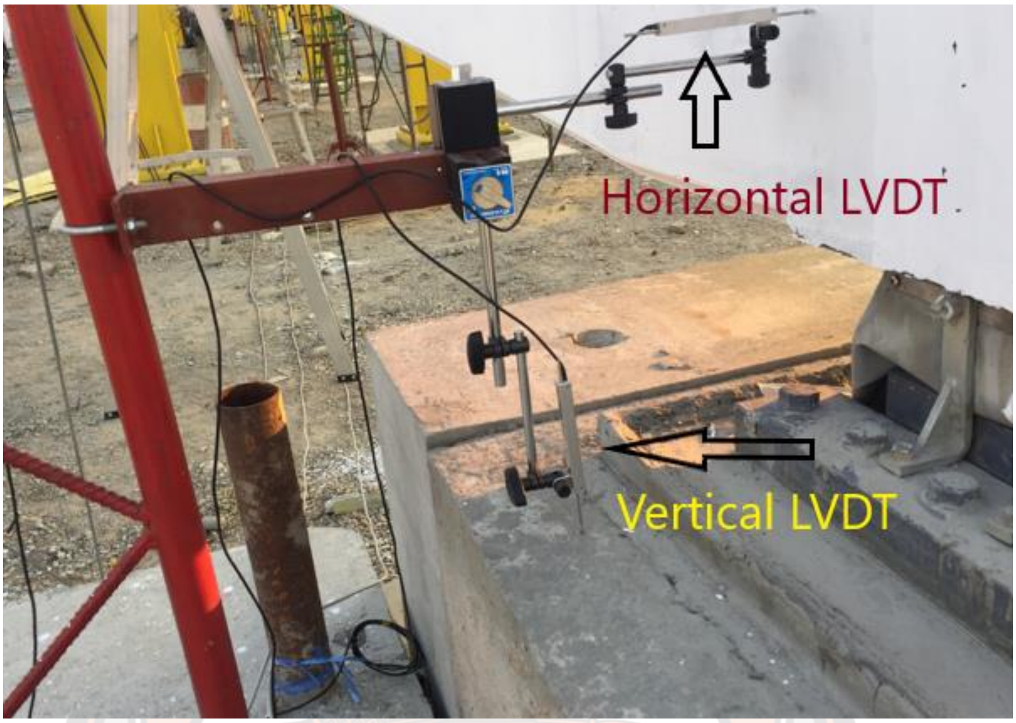

Figure 91 Typical installation of vertical and horizontal LVDTs

3.1.6 Strain of Longitudinal steel bars

In this experimental investigation, the strain on the longitudinal steel bars were measured by using steel strain gauges (gauge length = 5 mm). The steel strain gauges were installed at three locations i.e. middle of each girder as shown in figure 92. At each location a total number of 4 steel strain gauges were installed as shown in figure 93.

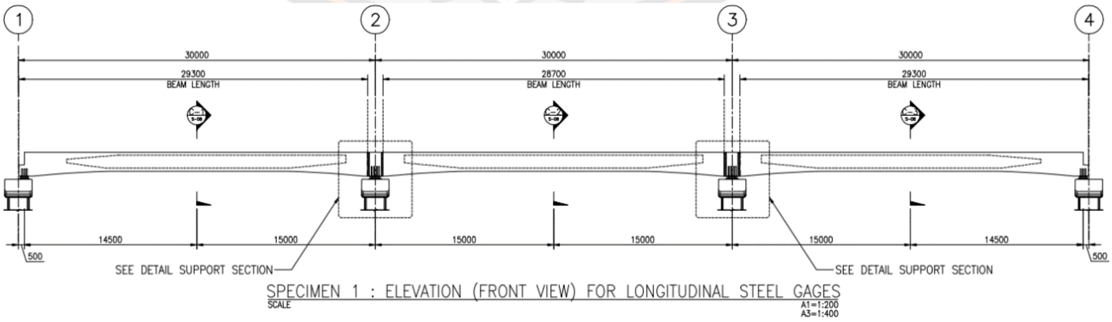

Figure 92 Typical details of steel strain gauges (longitudinal steel bars)

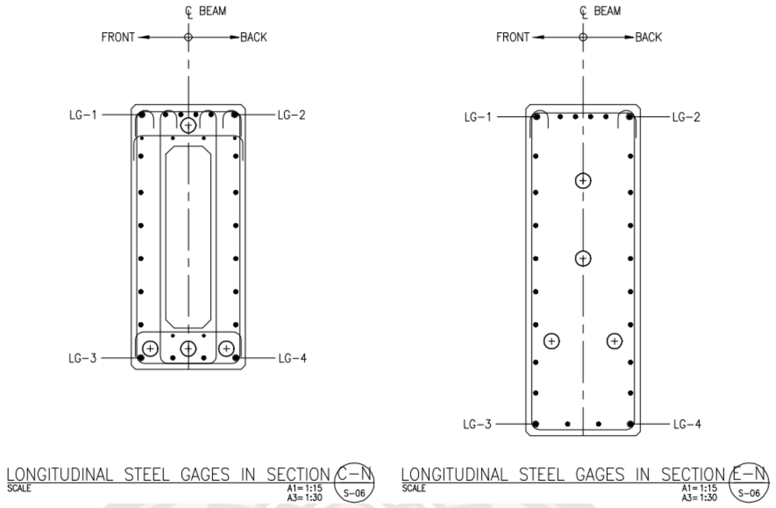

Figure 93 Sectional details of steel strain gauges (longitudinal steel bars)

3.1.7 Strain of Vertical steel bars

In this experimental investigation, the strain on the vertical steel bars were measured by using steel strain gauges (gauge length = 5 mm). The steel strain gauges were installed at eighteen locations i.e. middle of each girder as shown in figures 94 and 95. At each location a total number of two steel strain gauges were installed as shown in figures 96.

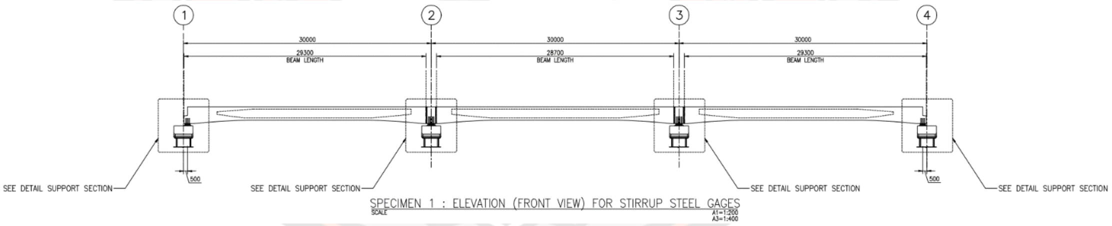

Figure 94: Typical details of steel strain gauges (vertical steel bars)

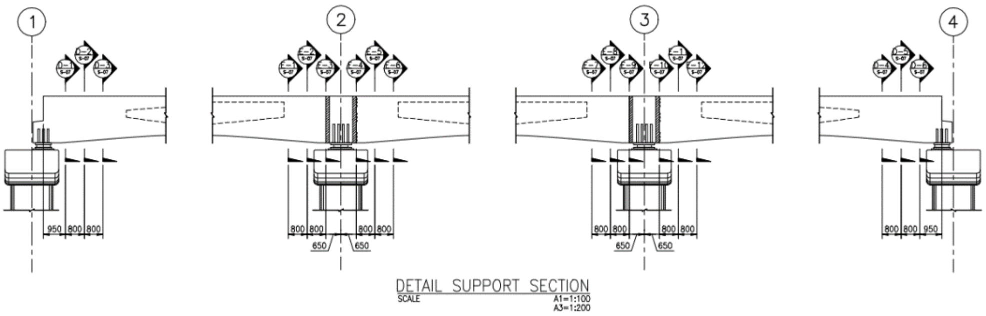

Figure 95 Typical details of locations (vertical steel bars)

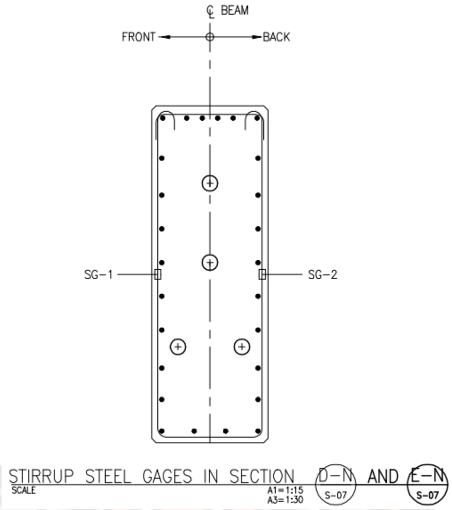

Figure 96 Sectional detail of steel strain gauges (vertical steel bars)

3.1.8 Strain of post-tension tendons

In this experimental investigation, the strain on the post-tension tendons were measured by using steel strain gauges (gauge length = 5 mm). The steel strain gauges were installed at the five locations i.e. middle and support of each girder as shown in figure 97. At middle location, total number of twenty strain gauges and at support location total number of eight strain gauges were installed as shown in figures 98 and 99.

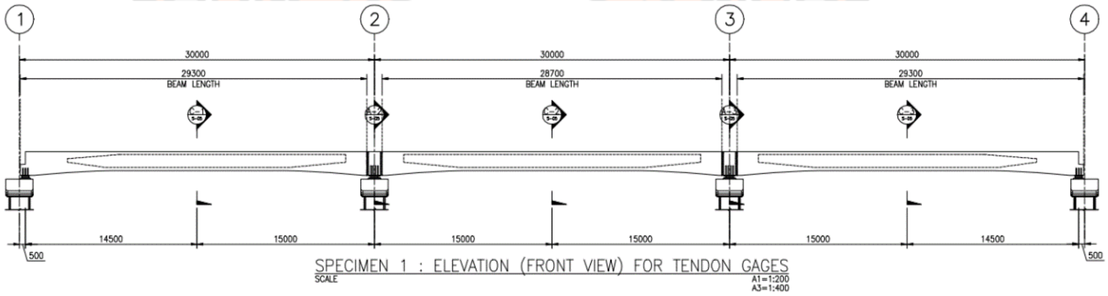

Figure 97 Typical details of steel strain gauge on post-tension tendons

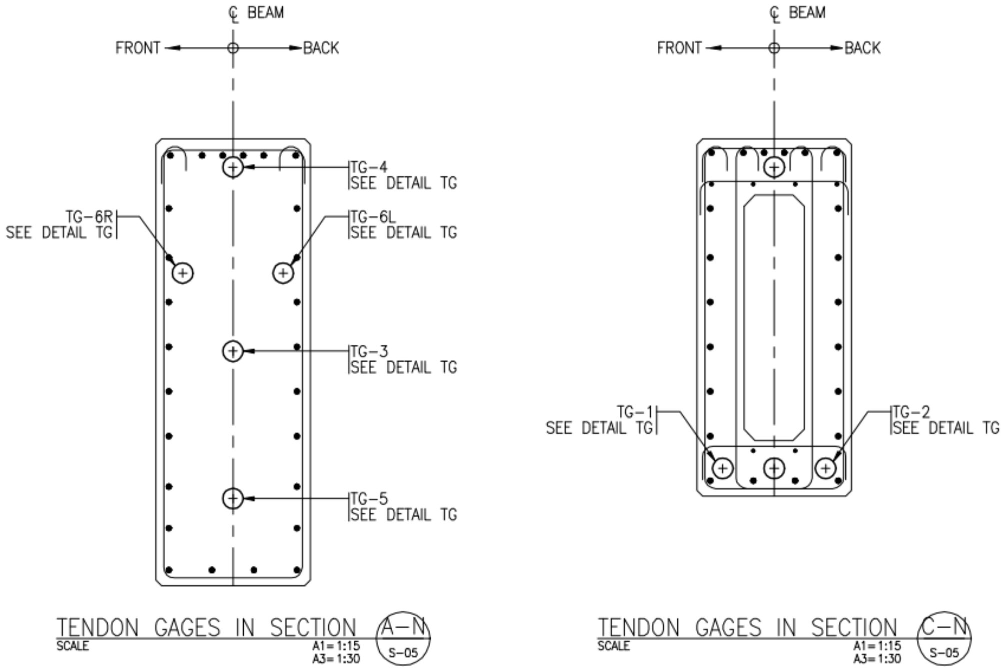

Figure 98 Sectional details of steel strain gauge on post-tension tendons

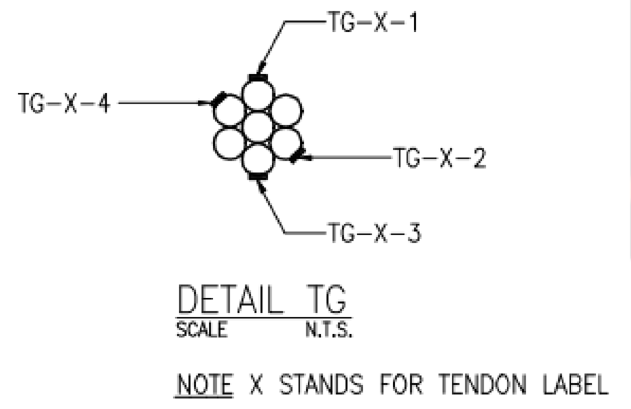

Figure 99 Numeric details of steel strain gauge on post-tension tendons

3.1.9 Loading setup

The three-span post-tensioned girder was subjected to four different types of loading conditions to accurately investigate the structural performance of all components in the three-span post-tensioned girder such as external and interior girders, pier segments, and wet joints. In the first type, two-point load up to service limit was applied at the right exterior beam, as shown in Fig. 100(a). In the second type, two-point loading was applied to the service limit at the interior girder, as shown in Fig. 100 (b). In the third type, four-point loading was applied to the service limit in such a way that two-point loading was applied at the left exterior beam and two-point loading at the middle girder at the same time, as shown in Fig. 100 (c). Finally, in the fourth type, four-point loading was applied to failure or the ultimate state in such a way that two-point loading was applied at the left exterior beam and two-point loading at the middle girder at the same time, as shown in Fig. 100 (c). Precast Post-tensioned Continuous (FPPC) girder is basically designed and constructed for the monorail train. The service load considered in this study is derived from the live load of the train, passenger's capacity and other standard parameters following the standard guides lines of ACI-343.1R-12 [47] and AASHTO LRFD Bridge Design Specifications 2014 [48]. The typical design load patterns (such as axle loads and distances between axles) and dimensional details of the monorail train are shown in Fig. 101 and Tables 8 and 9. For all loading types, pre-calibrated hydraulic jacks of capacity 250 Ton were mounted on the steel reaction frames. The load intensity was recorded by using pre-calibrated load cells, which were placed under the pistons of hydraulic jacks. The load was monotonically increased at a rate of 4 kN/min for each loading type. The initiation and propagation of the cracks were visually observed and recorded through photographs during the test. The load and displacement ordinates adopted in this study are graphically shown in Fig. 102.

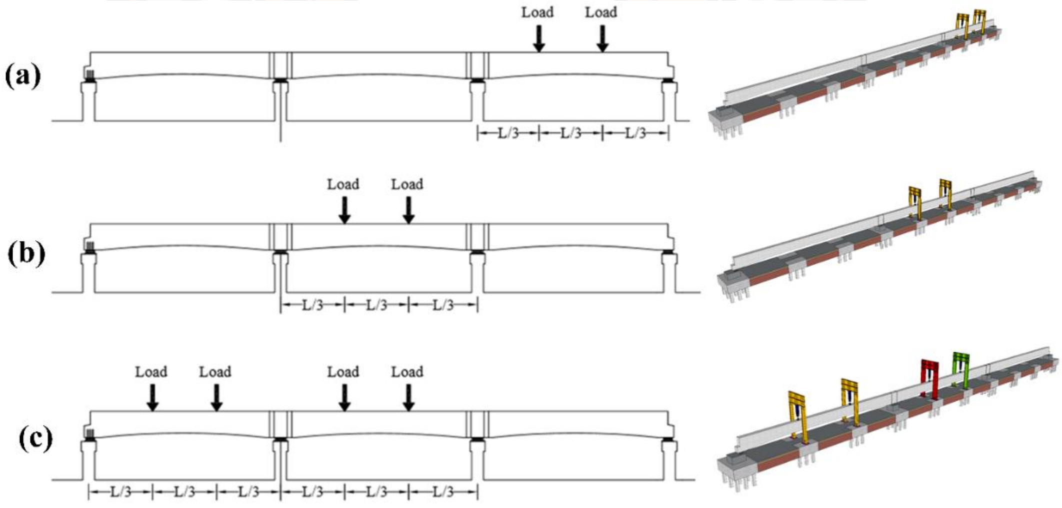

Figure 100 Details of the loading scenario setup.

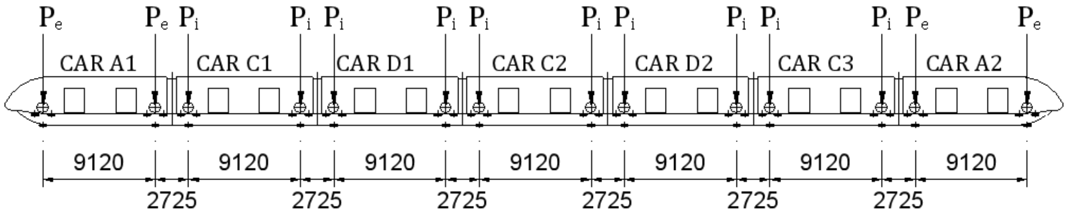

Figure 101 Details of the axle loads (Units: mm)

Table 8 Monorail axle loads

Load conditions	Axle load Pe (kN)	Axle load Pi (kN)
Empty	73.5	68.6
Seated	78.0	76.2
Seated + 6 Passengers/m^2	117.2	117.9
Seated + 8 Passengers/m^2	130.2	131.9

Table 9 Monorail dimensional details

Description	Distance (mm)
Car A1 and A2 Length (end car, including bellows)	13392
Car C1, C2, D1 and D2 Length (including bellows)	11845
Width over thresholds (static)	2951
Floor to ceiling height	2100
Guidebeam width	690

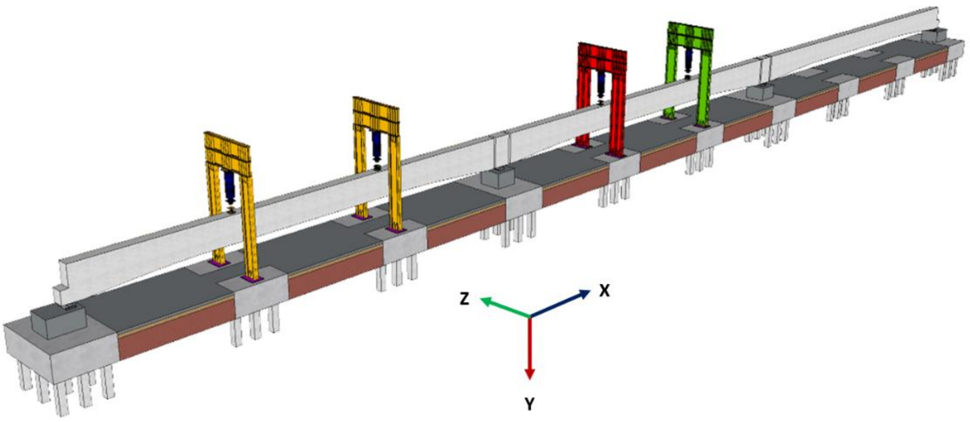

Figure 102 Details of typical ordinates

3.2 Part B: Small-scale Experimental Program

3.2.1 Test Matrix

A total of 9 reinforced concrete beams with and without hollow openings were tested in this study. Table 10 presents details of the test matrix adopted. Beams were categorized into three main groups depending upon the presence or configuration of adopted strengthening scheme. Each group contained 3 beams: one without any opening i.e., having a solid cross-section, one with an internal opening of 50 x 50 mm and one with an internal opening of 100 x 100 mm. All openings were made to coincide with the geometric center of beams. Figure 103 presents typical characteristics of tested beams in each group. To increase the flexural strength of beams with internal openings, group 2 and 3 beams were strengthened with CFRP sheets. Configuration of CFRP sheets was varied in group 2 and 3. Group 2 beams were strengthened with a single CFRP layer applied to their tension sides only thereafter called as configuration A (SCA). Beams of group 3 were strengthened with a U-shaped CFRP sheet applied to their tension sides thereafter called as configuration B (SCB). Adopted layout of CFRP sheets is shown in Figure 104. Figure 105 presents 2 beams in inverted position strengthened with CFRP sheet on tension side only (left) and in U-shape (right). Nomenclature of beams was chosen to represent beam's ID, presence/size of internal opening, and the configuration of CFRP sheet in chronological order. For instance, B04-SS-SCA represented beam number 4 (B04) with solid section (SS) strengthened with CFRP sheet applied in configuration A.

The reinforced concrete beams were designed following the standard guidelines of ACI standards. However, the hollow sections i.e., openings were selected in such a way to facilitate the proper concrete cover for steel bars on each face of beam. Each beam measured 250 x 300 mm in cross section to 300 mm in length. On tension side, each beam was reinforced with 2 DB-16 (16mm) steel bars while 2 DB-12 (12mm) bars were provided in compression zone. On account for flexural strength as an objective parameter, each beam was provided with sufficient shear reinforcement. Shear reinforcement consisted of round steel bars of 6 mm diameter (RB6) spaced at 100 mm near supports. Spacing of stirrups was increased to 200 mm towards the zone of low shear demand as shown in Figure 103. All beams were incorporated with a concrete cover of 20mm. To avoid stress concentrations near sharp corners, corners were rounded to a radius of 30mm to avoid premature rupture of CFRP.

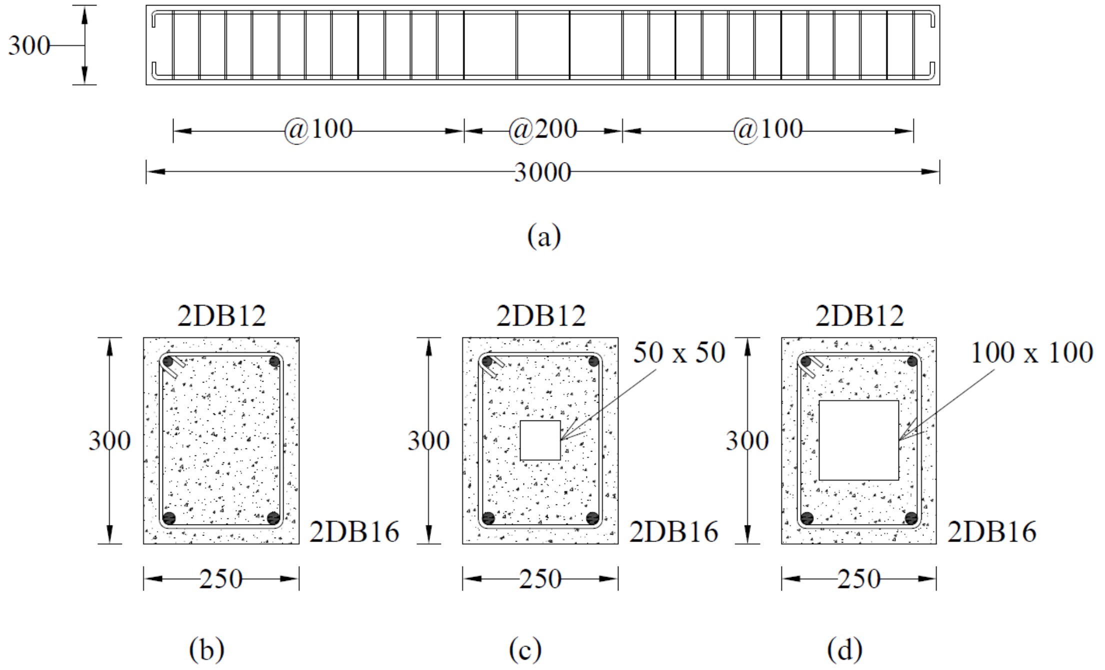

Figure 103 Typical beams in each group

Table 10 Test matrix

Beam ID	Square Opening Side Dimension (mm)	CFRP Configuration
B01-SS-CON	-	-
B02-HS50-CON	50	-
B03-HS100-CON	100	-
B04-SS-SCA	-	Tension side
B05-HS50-SCA	50	Tension side
B06-HS100-SCA	100	Tension side
B07-SS-SCB	-	U-shape
B08-HS50-SCB	50	U-shape
B09-HS100-SCB	100	U-shape

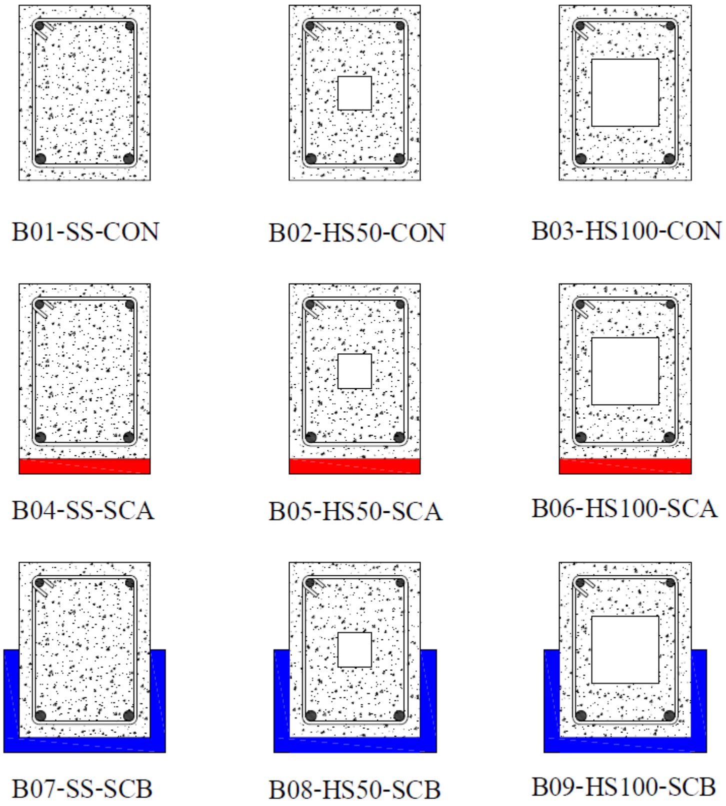
B01-SS-CON
B02-HS50-CON
B03-HS100-CON
B04-SS-SCA
B05-HS50-SCA
B06-HS100-SCA
B07-SS-SCB
B08-HS50-SCB
B09-HS100-SCB

Figure 104 Layout of CFRP sheets

Figure 105 Application of CFRP sheet on bottom of beams (left) tension side only (right) u-shape sheet

3.2.2 Material Properties

All beams were cast from a single batch of ready-mix concrete. Slump test revealed a value of 120 mm. Standard cylinders were cast as per the recommendations of ASTM C39 / C39M - 21 and average 28-days compressive strength was found to be 35 MPa. DB-16 and DB-12 deformed steel bars were used for bottom and top longitudinal reinforcement, respectively. Vertical reinforcement consisted of round steel bars having 6 mm diameter. Their mechanical properties were found following the protocols of ASTM A615 / A615M – 2Click or tap here to enter text.. Table 11 presents measured mechanical properties of steel reinforcement. Properties of CFRP sheets were determined as per ASTM D7565 / D7565M - 10(2017) provisionsClick or tap here to enter text.. Thickness of CFRP sheet was 1.67 mm with measured ultimate tensile strength and strain as 350 MPa and 1.5%, respectively. Elastic modulus of CFRP sheet was found to be 250 GPa. Properties of epoxy resin used to bond CFRP sheet with beams were provided by manufacturer. Provided tensile strength and strain of epoxy resin were 50 MPa and 2.5%, respectively.

Table 11 Measured mechanical properties of steel reinforcement

Steel Bar	Yield Strength (MPa)	Ultimate Strength (MPa)
RB-6	250	350
DB-12	400	500
DB-16	420	550

3.2.3 Construction and Strengthening

The construction of the 9 beams was done in the Laboratory. First the plywood framework was applied for exact dimensional specifications of the beams. Then, foam of required sizes (50 x 50 mm x mm, 100 x 100 mm x mm) was cut and placed in the framework (Figures 106 and 107). The wires were used to ensure the stability of the foams so that they should get displaced during the concrete pouring process. The concrete pouring was done using conventional methods of pouring and hand vibrators were used to decrease the vapors and void spaces in the concrete for the sake of compaction. After 24 hours the framework was removed and curing process of the concrete was continued for 7 days. During the curing process, the concrete beams were wrapped with the help of burlap sack in order to ensure that proper curing process is done. After the curing process, the sides of the beams were grinned to make them smooth in order to prepare them for the application of the FRP material. The FRP was applied using conventional methods with the help of hand lap and brush. First, the epoxy resin was applied on the required surface where it was required to apply the FRP, then FRP was applied using conventional approach (hand lap and brush). After the application of the FRP, again the epoxy resin was applied to make sure that there is exact bond between the concrete and FRP layers.

Figure 106 Installation of foam in steel bars

Figure 107 Installation of steel bars in formwork

3.2.4 Instrumentation & Load Setup

A four-point bending loading was applied to each beam as schematically shown in Figure 108. Monotonically increasing load was applied that generated a constant-moment region within the middle 500mm of beams. Three Linear Variable Differential Transducers (LVDT) were attached at the bottom of each beam to measure their vertical deflections while two LVDTs were attached to each support to measure their uplifts. 5-mm Strain gages were attached to top and bottom longitudinal reinforcement at midspan as shown in Figure 109. A 60-mm strain gage was also attached to concrete at the bottom side of each beam at its midspan. A load-controlled setup was adopted with load applied using a hydraulic jack whose intensity was measured with a 50kN load cell placed concentrically underneath it. Figure 110 shows actual setup during test.

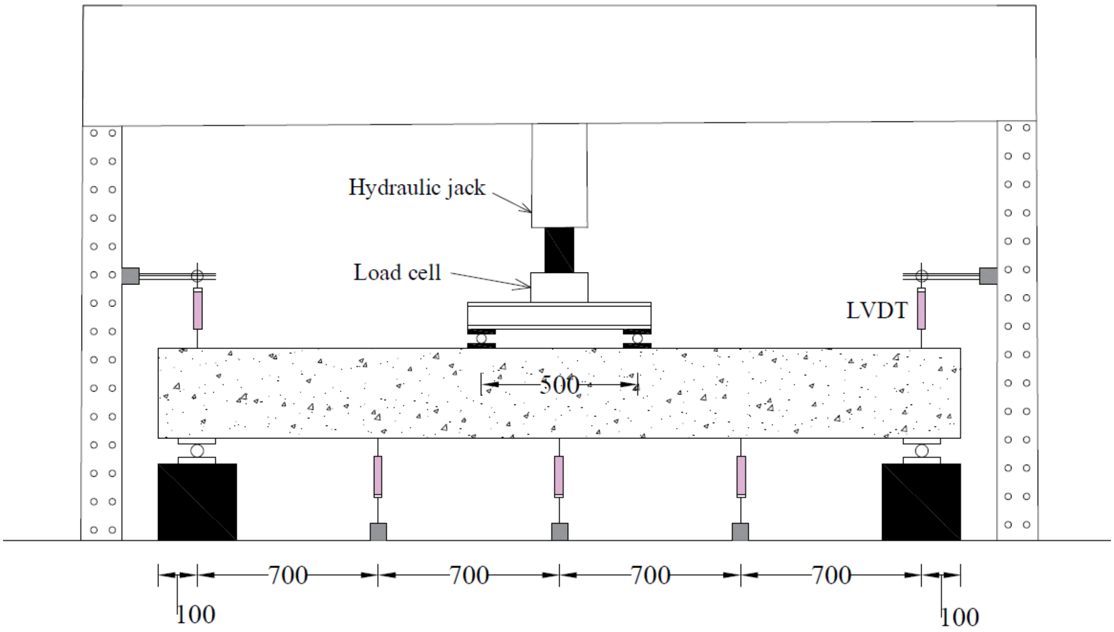

Figure 108 Load setup (units mm)

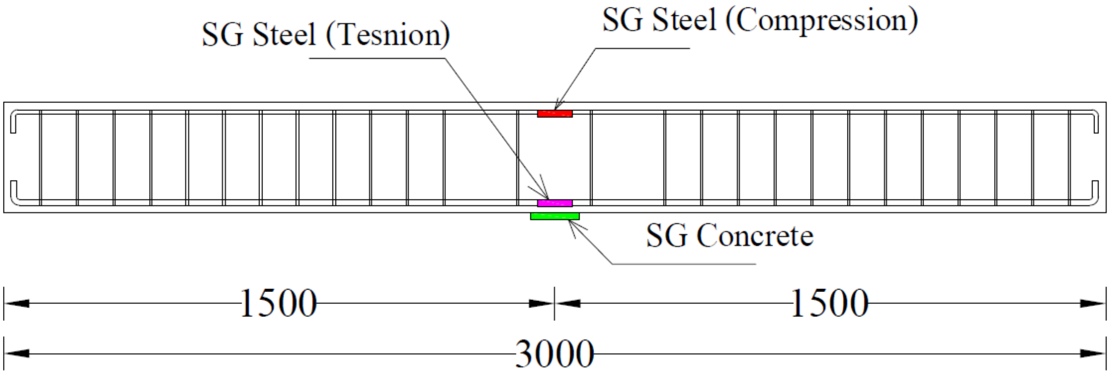

Figure 109 Position of strain gages (units mm)

Figure 110 Actual test setup

3.3 Part C: Finite Element Analysis of Large-Scale Girders

In this study, finite element analysis (FEA) of FPPC monorail bridge girder was performed by using a computer program ATENA which is a computational tool for nonlinear engineering analysis of bridges and culverts [49-51]. The FEA allows for easier modeling of complex geometrical and irregular shapes [52-54]. The computer program ATENA contains different built-in material models for concrete, steel and other materials. In this study, the built-in fracture-plastic constitutive material model CC3DNonLinCementitious2 was used to model concrete. The material properties of steel bars and PT tendons were assigned using built-in CCReinforcement material model in a multi-linear plastic stress-strain relationship. At the first load step the body force and the pre-stressing were applied. In the following loading procedure, a prescribed load was increased step by step. More details on built-in material models can be found in ATENA Theory (Cervenka et al. 2002). A typical finite element model of FPPC monorail bridge girder is shown in Fig. 111 and application of the load is shown in Fig. 112. The material properties used in the finite element analysis are summarized in Tables 12 and 13.

Table 12 Average compressive strength of components FPPC girder.

Components	Compressive strength (MPa)	Tensile strength (MPa)
Left exterior girder	65	7.1
Right exterior girder	64	6.9
Interior girder	65	7.2
Pier segments	62	6.4
Wet joint	45	5.2

Table 13 Mechanical properties of steel bars and wire strands.

Steel bars and or wire strands	Yield strength (MPa)	Ultimate tensile strength (MPa)
DB16	420.0	480.0
DB20	420.0	520.0
DB25	440.0	560.0
7-wire strand	1500.0	1800.0

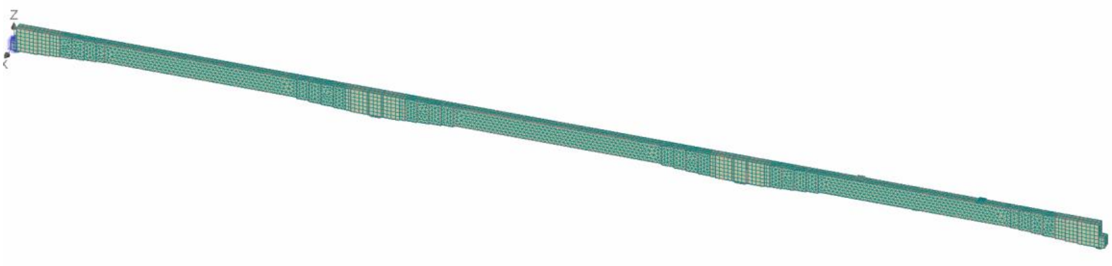

Figure 111 Typical finite element model (FEM) of FPPC bridge girder

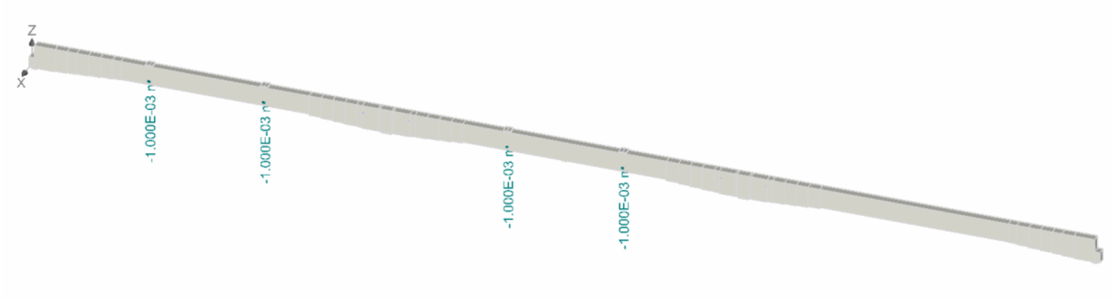

Figure 112 Application of load on FEM – Load on left exterior and middle interior girder

Chapter IV

Experimental Results

4.1 Part A

In terms of girder deflection, out-of-plane movement, crack width and ultimate failure modes, the experimental results are discussed in the following sections. The experimental results are discussed with reference to Fig. 113. In this case, specific labels are used to represent the locations of piers or supports (P01 to P04), bearings (B-01 to B-04), LVDTs for each girder (L-01 to L-09) and wet joints (W-01 to W-04).

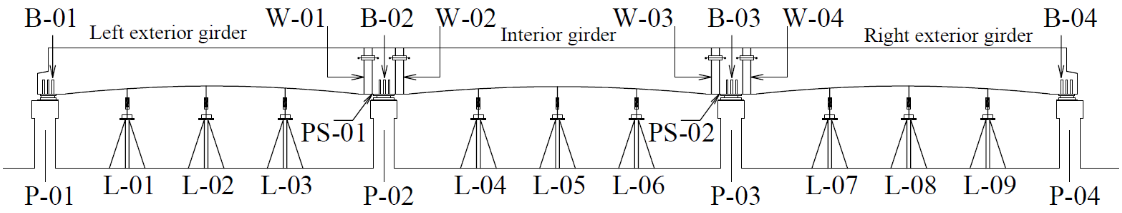

Figure 113 Layout of FPPC girder.

4.1.1 Load versus deflection responses

4.1.1.1 Type One

In this load case, two-point load under service limits was applied at the right exterior girder, and deflection of all girders (right exterior girder, interior girder and left exterior girder) was recorded by using LVDTs at different locations. Due to the applied load, only the downward deflection of the right exterior girder was observed, whereas both the interior and left exterior girders remained un-deflected. The load versus deflection responses (Y direction) of right exterior girder are shown in Fig. 114. In this case, the highest deflection of 23.0 mm was observed at the mid of right exterior girder. The highest observed deflection is significantly less than the permissible limits (i.e., L/1000). The lowest deflection of 14.0 mm was observed towards the continuous end (i.e., point A), and moderate deflection of 16.0 mm was observed towards the discontinuous end. Further, it can be seen that the load versus deflection responses at all locations of the right exterior girder are linear, indicating no yielding of the steel bars or tensile cracking of the concrete. The results proved that the design and construction details of the FPPC girder system are adequate under service loads.

4.1.1.2 Type Two

In this load case, two-point load under service limits was applied at the interior girder and deflection of all girders (right exterior girder, interior girder and left exterior girder) was recorded by using LVDTs at different locations. Due to the applied load, only the downward deflection of the interior girder was observed, whereas both left and right exterior girders remained un-deflected. The load versus deflection responses (Y direction) of the right exterior girder are shown in Fig. 115. In this case, the maximum deflection of 21.0 mm was observed at the middle of the interior girder (i.e., L-08). The highest observed deflection is significantly less than the permissible limits (i.e., L/1000, where L is span length). Deflection towards both continuous ends was observed as 12.0 mm. Similar to the right exterior girder, the loads versus deflection responses at all locations of the interior girder are linear, indicating no yielding of the steel bars or tensile cracking of the concrete. The results proved that the design and construction details of the FPPC girder are adequate against service load.

4.1.1.3 Type Three

In this case, the service load was applied at both the left exterior girder and interior girder at the same time. For each girder, two-point load under service limits was applied and deflection of all girders (right exterior girder, interior girder and left exterior girder) was recorded by using LVDTs at different locations. Due to the applied load, only the downward deflection of the left exterior girder and interior girder was observed, whereas the right exterior girder remained un-deflected. The load versus deflection responses (Y direction) of right exterior girder and interior girder are shown in Figs. 116 and 117, respectively. Overall, the downward deflection of the interior girder was observed higher than the left exterior girder. For both girders (Right exterior girder and interior girder), the maximum deflection was observed at the middle locations (i.e., locations L-02 and L-05). In the case of the left exterior girder, the lowest deflection of 4.9 mm was observed at the discontinuous end (i.e., Location L-01).

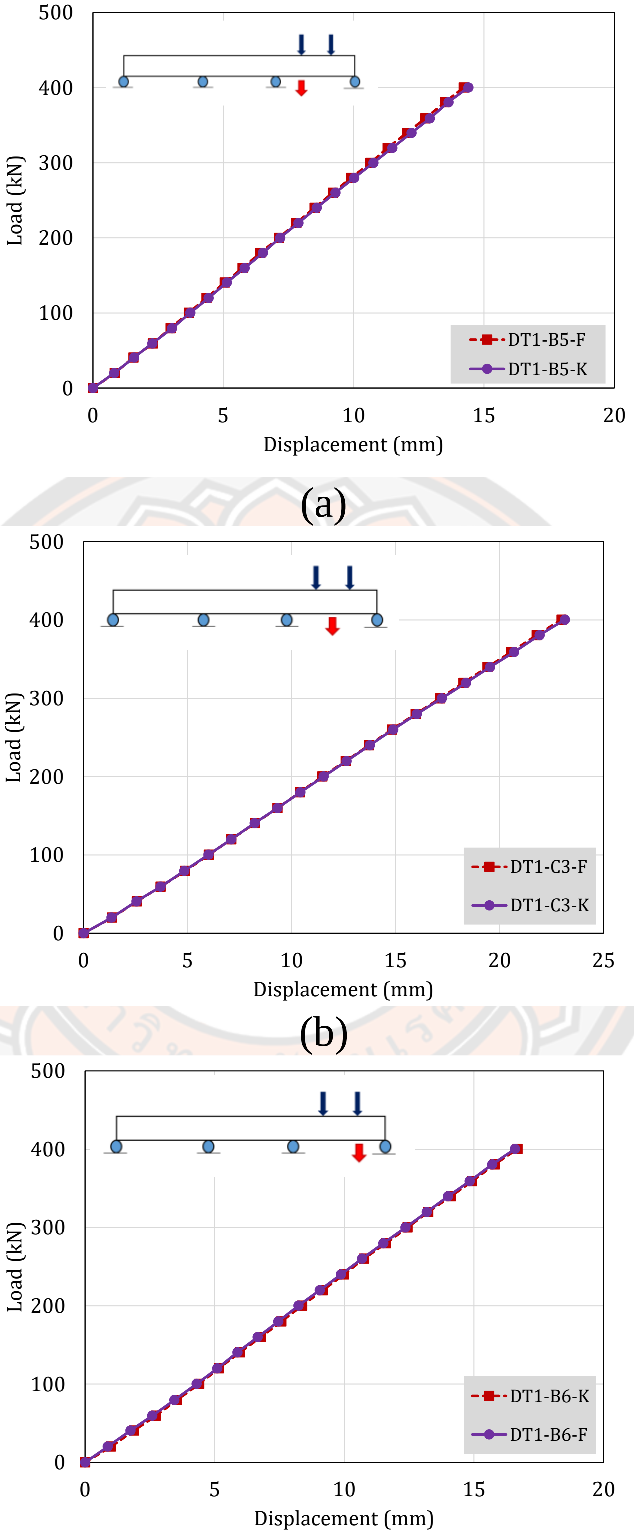

(a)

(b)

(c)

Figure 114 Load versus deflection responses (Y direction) - Load at the right exterior girder.

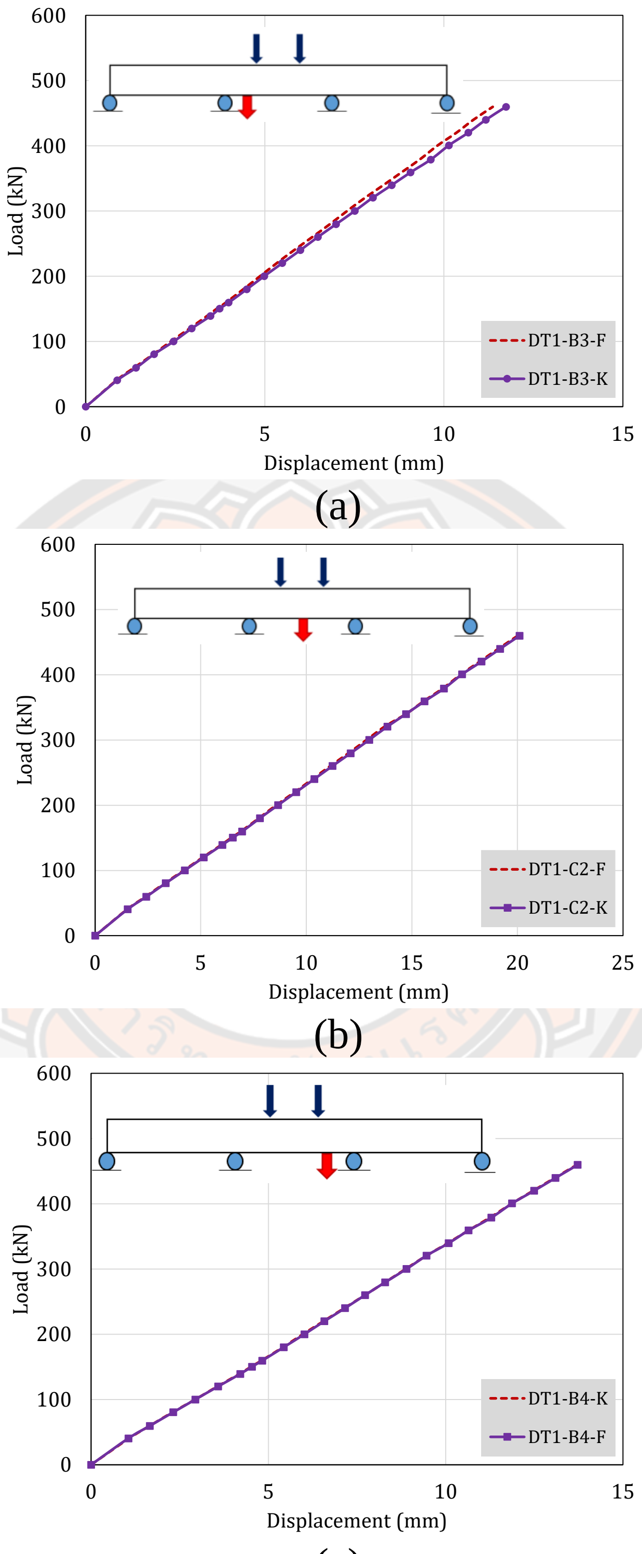

(a)

(b)

(c)

Figure 115 Load versus deflection responses (Y direction) - Load at the middle interior girder.

In the case of the interior girder, the lowest deflection was observed at location L-04. In general, the maximum deflection of both girders is observed less than the permissible limits. Also, the load versus deflection responses (Y direction) at each location is observed to be essentially linear under four-point loading.

4.1.1.4 Type Four

In this case, the monotonic load was applied at both the left exterior girder and interior girder until ultimate failure of the FPPC girder to access the ultimate load-carrying capacity and failure modes. In order to avoid damage to the LVDTs and other equipment, only the mid-span deflection of the interior girder was recorded at location L-05 by using a string potentiometer. The load versus mid-span deflection response (Y direction) of interior girder is shown in Fig. 118. The ultimate load of FPPC girder was recorded as 2600 kN and corresponding ultimate deflection was observed as 210 mm. The ultimate load of the FPPC girder was observed higher than the design load. Further, it can be seen that the load versus deflection response of interior girder is bilinear. The first linear part (with high stiffness) was observed until 550 kN and then, at this stage, the first flexural crack was perceived at the middle of the interior girder at location L-05.

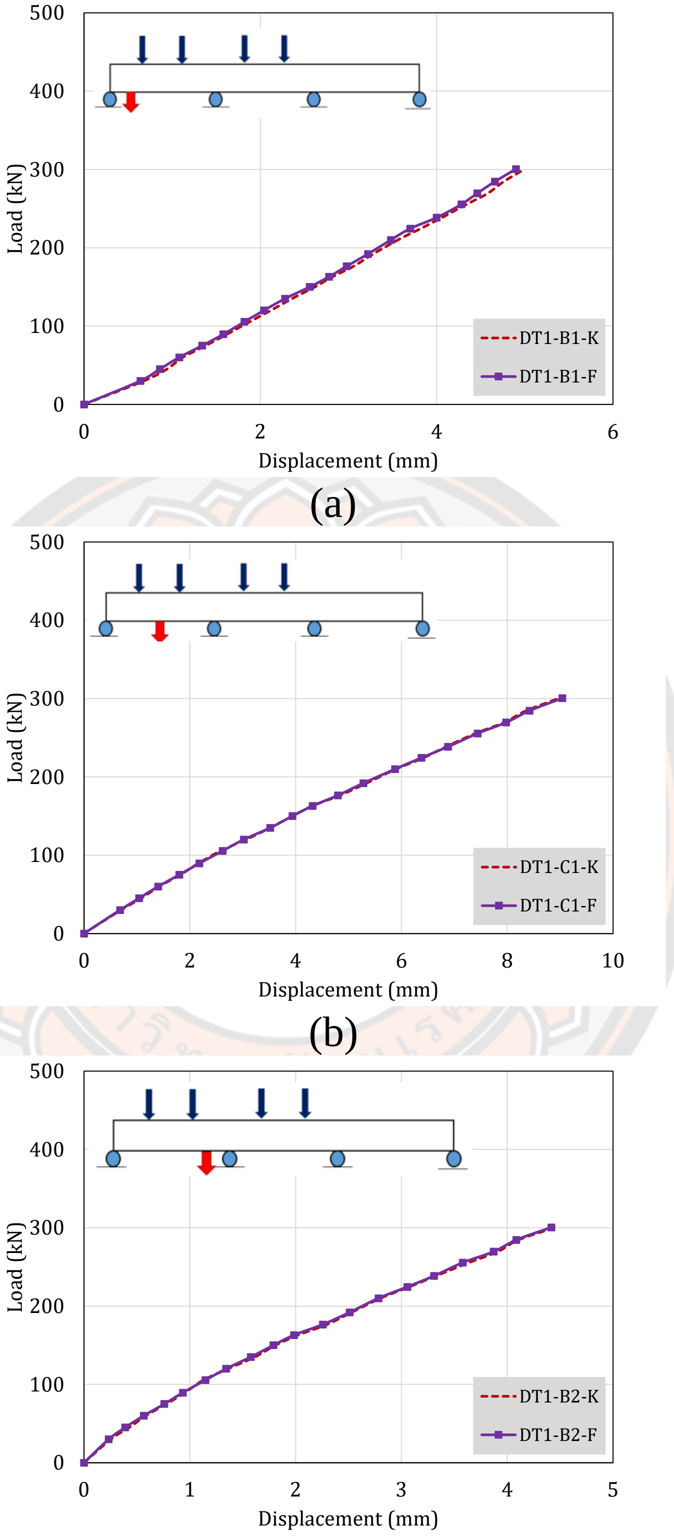

(c)

Figure 116 Load versus deflection responses of left exterior girder (Y direction)

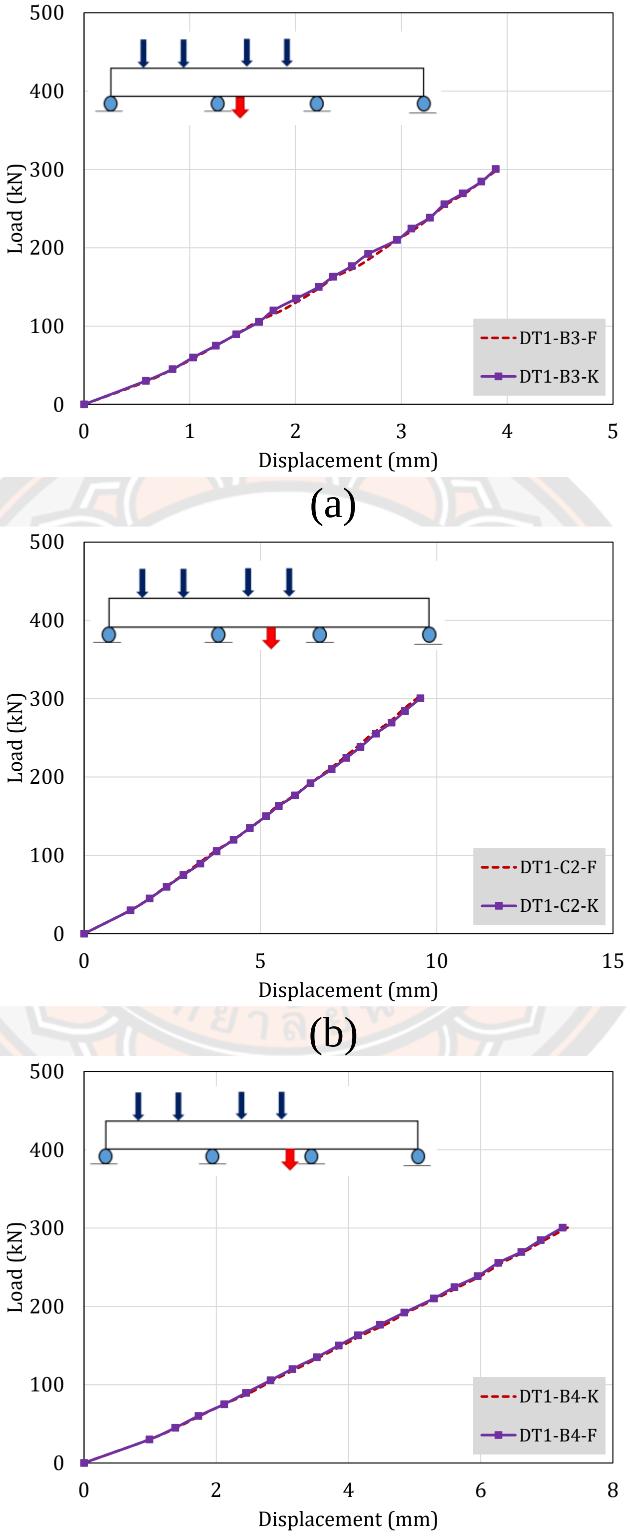

(a)

(b)

(c)

Figure 117 Load versus deflection responses of middle interior girder (Y direction)

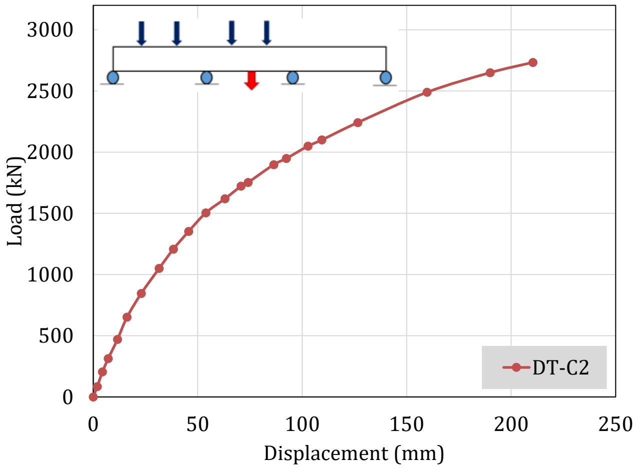

Figure 118 Load versus deflection response of middle interior girder (Y direction)

4.1.2 Out-of-plane movement of FPPC girder

In this study, LVDTs in the lateral direction were installed at the pier segments and dis-continuous ends of the exterior girders to monitor the out-of-plane movement (Z direction) of the FPPC girder during each load case. Regarding load versus out-of-plane movement (Z direction), the experimental results are shown in Figs. 27-29. In the case of loading condition Type-01, out-of-plane movement was only observed at pier segment number 02 i.e., PS-02. All other locations such as PS-01 and discontinuous ends remained rigid, and out-of-plane movement was not observed. The observed out-of-plane movement was minimal and less than 0.5 mm at both locations of pier segment number 02, as shown in Fig. 119. In contrast to loading condition Type-01, out-of-plane movement was observed at both pier segments in the case of loading condition Type-02, as shown in Fig. 120. However, the maximum value of out-of-plane movement was much lower than the loading condition Type-01 because the load was applied at the middle girder and distribution of the load was towards both the right and left exterior girders. Further, in the case of loading condition Type-03, the out-of-plane movement was observed at discontinuous end of left exterior girder and both pier segments, as shown in Fig. 121. In this case, the highest out-of-plane movement was recorded at pier segment number 02 i.e., PS-02 as compared to the other locations. However, observed out-of-plane movement was minimal and less than 0.5 mm at all locations. The test results indicate that the design and construction details of the FPPC girder are adequate to resist out-of-plane movement under service load conditions.

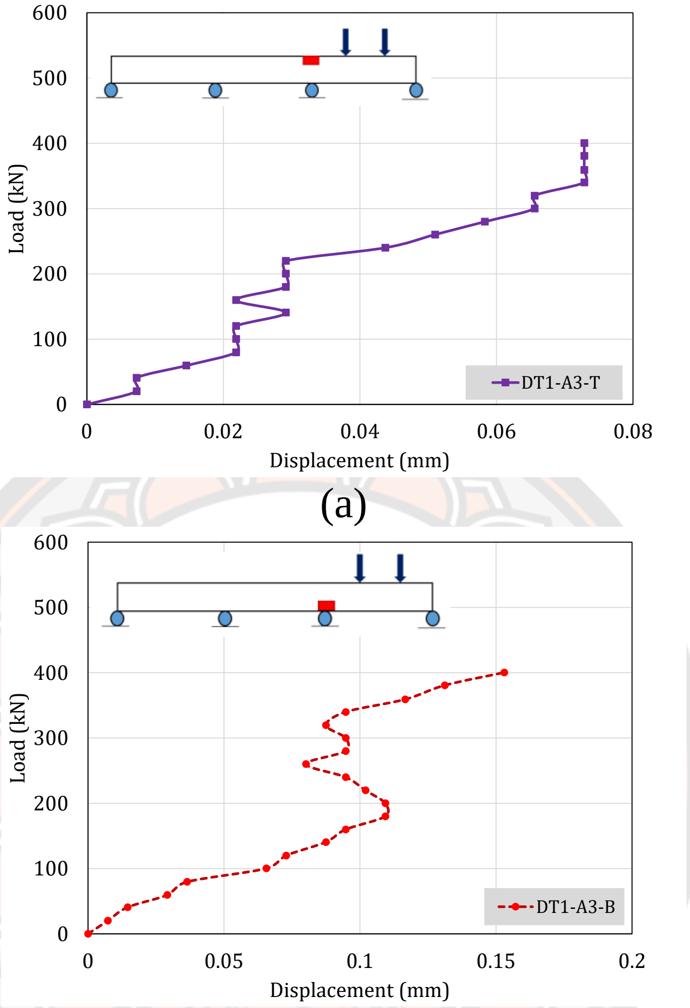

(a)

(b)

Figure 119 Load versus out-of-plane movement (Z direction) - Load at the right exterior girder.

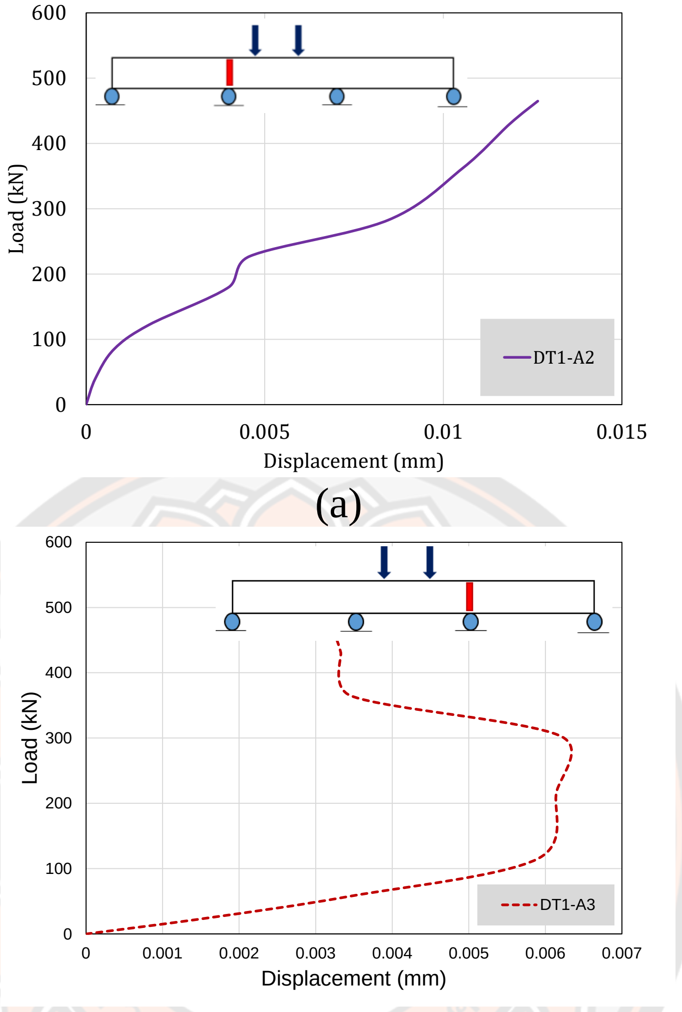

(a)

(b)

Figure 120 Load versus out-of-plane movement (Z direction) - Load at the interior girder.

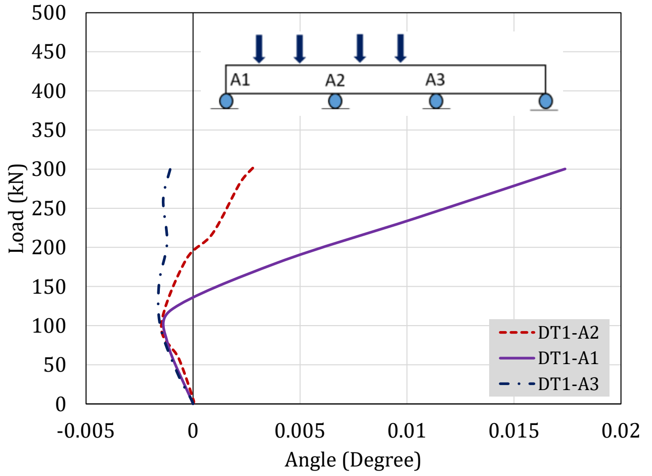

Figure 121 Load versus out-of-plane movement (Z direction) - Load at the left exterior and interior girder.

4.1.3 Performance of Wet Joint

In order to observed the performance of the wet joints, four crack gauges (one on each wet joint) were installed to observe the initiation and propagation of cracks at the location of the wet joints. The experimental results, in terms of load versus crack width, are shown in Figs. 122-124. In the case of loading condition Type-01, maximum crack width of 0.18 mm was observed at wet joint W-04, and minimum crack width of 0.009 mm was observed at wet joint W-01, as shown in Fig. 122. In the case of loading condition Type-02, however, the crack width was also larger at wet joint W-04 than the crack width at wet joint W-01, as shown in Fig. 123. This could be because the right exterior girder was already loaded to service load under loading condition Type-01. Further, the maximum crack width was also observed at wet joint W-04 in the case of loading condition of Type-04, as shown in Fig. 124. Although crack widths were recorded at each wet joint, the observed values were much smaller than the permissible limits (For reinforced concrete sections, a maximum design crack width of 0.3 mm is recommended in BS 8110, mainly for aesthetic reasons). This indicates that the considered wet joints are suitable to safely transfer the loads.

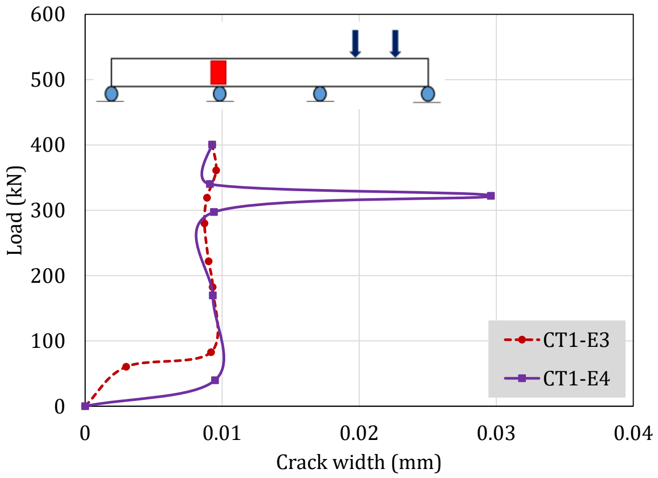

(a)

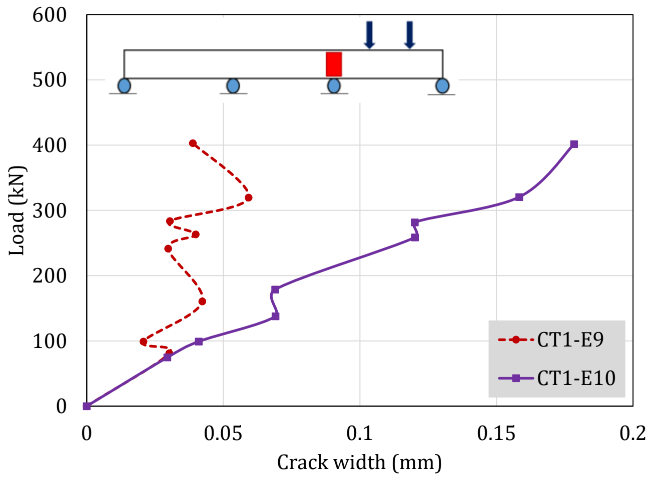

(b)

Figure 122 Load versus crack width (Loading condition Type-01)

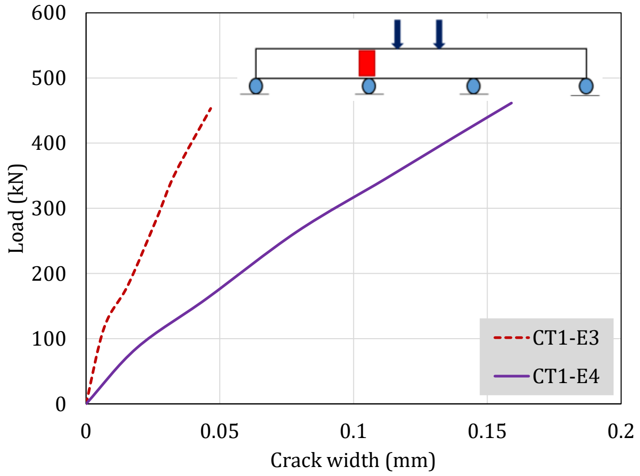

(a)

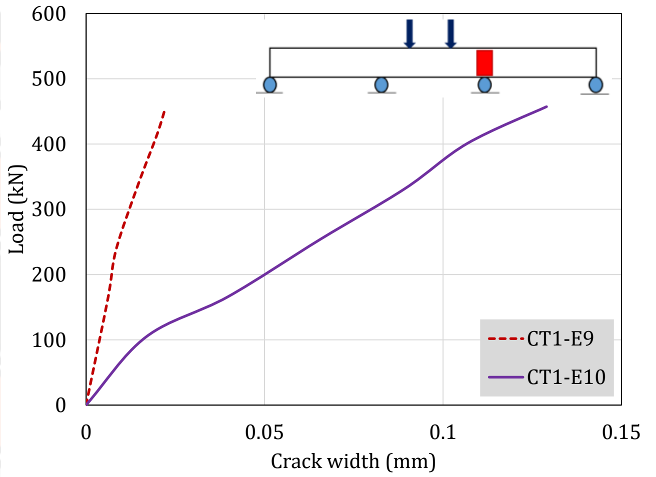

(b)

Figure 123 Load versus crack width (Loading condition Type-02)

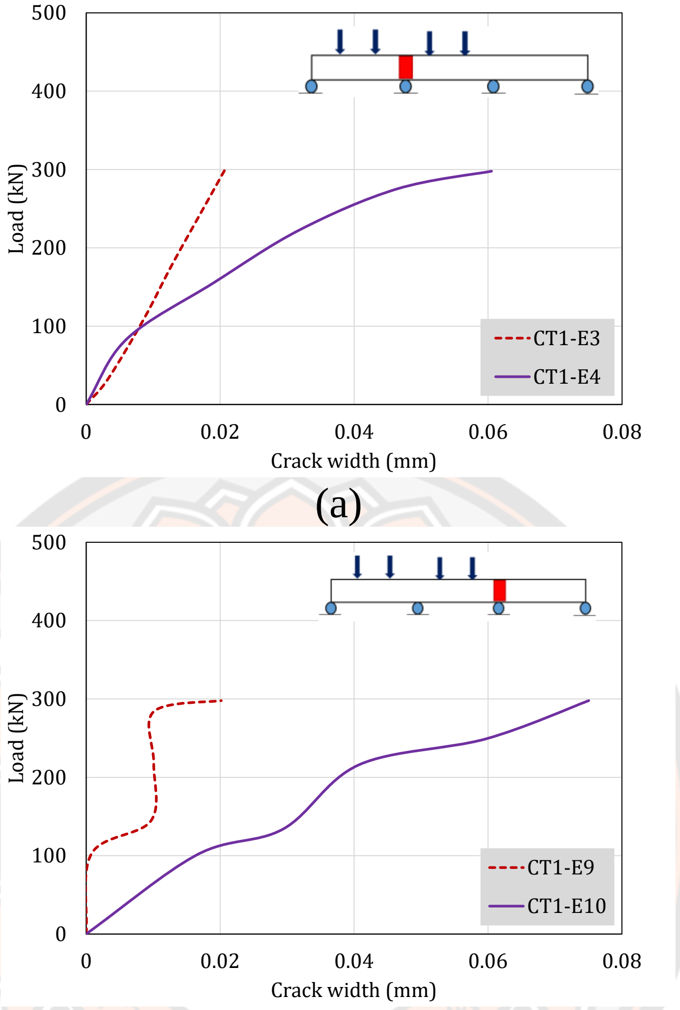

(a)

(b)

Figure 124 Load versus crack width (Loading condition Type-03)

4.1.4 Settlement of Piers

In this study, vertical LVDTs were installed on piers to observe the settlement of the piers during different loading conditions. The settlement of the piers was not observed in this study and readings on each LVDTs were constantly observed as zero. This indicates that the design of piers and foundations was adequate to resist the applied service and ultimate load conditions.

4.1.5 Strain of Longitudinal Steel Bars

4.1.5.1 Type One

4.1.5.1.1 Location E10-12

At each location, strain gages were attached to both the top and bottom longitudinal steel bars. Positive values of strains were referred to the tension while negative values were associated with compression. Therefore, positive values at supports showed strains at top longitudinal bars while positive values at mid-span represented the response of bottom longitudinal bars. As shown in Figure 125, maximum tensile strain recorded was around 90 microns while maximum negative strain was around 140 microns. Since this loading reflected the response under service limit state, strain response showed a linear relationship with the applied load.

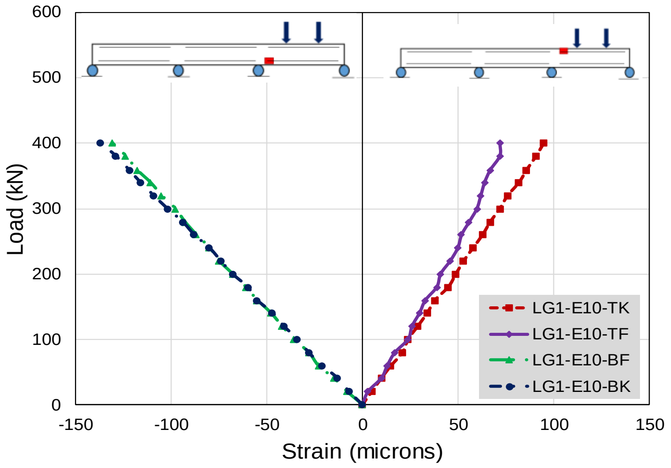

Figure 125 Strains values recorded at location E10 (Loading Setup SP-1-L01)

4.1.5.1.2 Location C3

Location C3 corresponds to the midspan of the right exterior span. Maximum positive strain recorded was around 200 microns while the corresponding negative value was 220 microns (Figure 126). Again, due to limitation applied on the load to be within service limit, strains exhibited a linear response with the applied load.

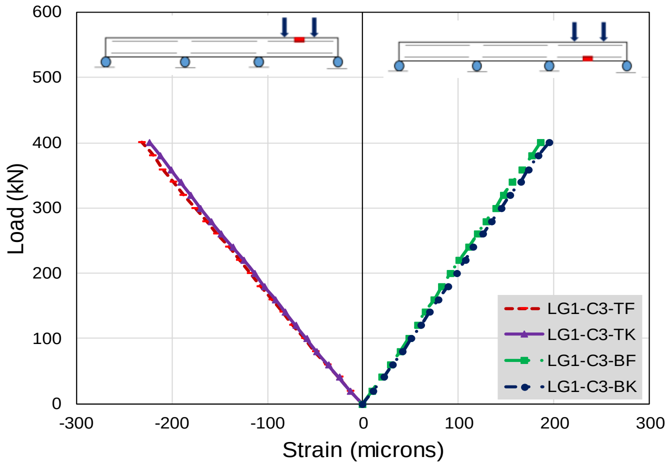

Figure 126 Strains values recorded at location C3 (Loading Setup SP-1-L01)

4.1.5.2 Type Two

4.1.5.2.1 Location E4-E6

This location corresponds to the interior face of left interior support. Maximum positive and negative strains recorded were limited to 75 and 60 microns, respectively. Further, owing to the nature of applied load, strains exhibited linear relationship with the applied load (Figure 127).

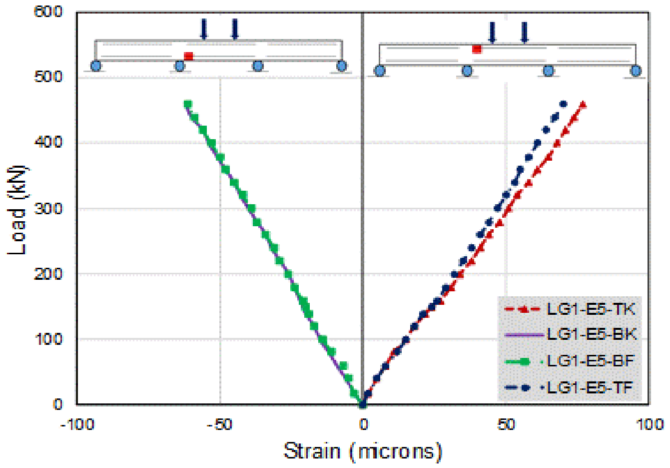

Figure 127 Strains values recorded at location E5 (Loading Setup SP-1-L02)

4.1.5.2.2 Location E7-E9

This location corresponds to the interior face of right interior support. Maximum positive and negative strains recorded under service loads were 95 and 72 microns, respectively (see Figure 128) and again exhibited linear relationship with the applied load.

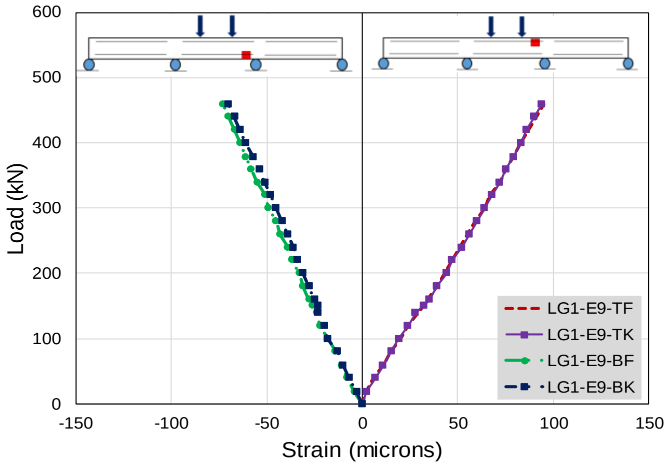

Figure 128 Strains values recorded at location E9 (Loading Setup SP-1-L02)

4.1.5.2.3 Location C2

Strains recorded at middle of the interior span were referred with C2 as shown in Figure 129. Both positive and negative strains reached 180-190 microns and were noticeably higher than those recorded at interior faces of interior supports. Nonetheless, since the load was constrained to service limit, strains showed a linear response with the applied load.

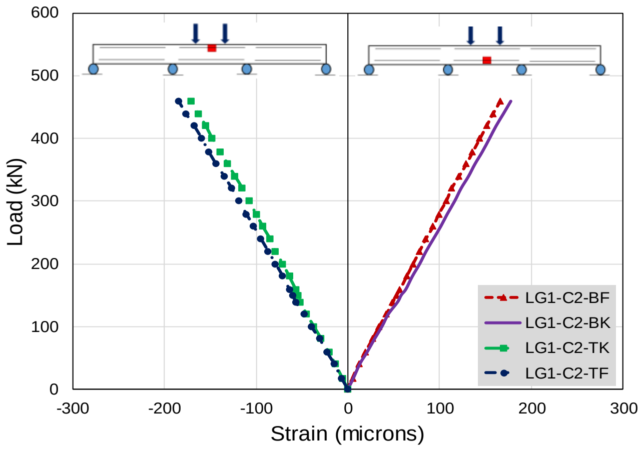

Figure 129 Strains values recorded at location C2 (Loading Setup SP-1-L02)

4.1.5.3 Type Three

4.1.5.3.1 Location E1-E3

This location corresponds to exterior face of left interior support. Maximum positive and negative strains were approximately 120 microns as shown in Figure 130. Strains recorded showed linear relationship with the applied service load.

4.1.5.3.2 Location E4-E6

Maximum positive and negative strains recorded at this position under 4-point service load were limited to 105 and 110 microns, respectively exhibiting linear response with the applied load (Figure 131).

4.1.5.3.3 Location E7-E9

Maximum strains recorded at this position were quite low as compared to strains at other locations under the same load. Both positive and negative strains were limited to 50 microns (see Figure 132) substantially lower than the yield strain.

4.1.5.3.4 Location C1

Location C1 corresponds to the middle of left exterior span. Maximum positive and negative strains were limited to 75 and 90 microns, respectively (see Figure 133) under 4-point service load. Strains remained linear with the applied load up till the service limit.

4.1.5.3.5 Location C2

Maximum positive strain recorded at location C2 and under 4-point service load was limited to 90 microns while its corresponding negative recorded value was 105 microns. Again, strain-load behavior remained linear for both positive and negative strain values. It is to be mentioned that strain values recorded at this position and under 2-point service loads were significantly higher reaching around 190 microns (see Figure 134).

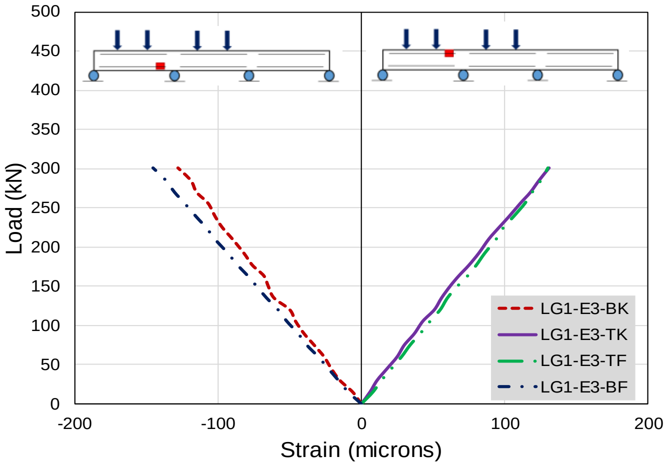

Figure 130 Strains values recorded at location E3 (Loading Setup SP-1-L03)

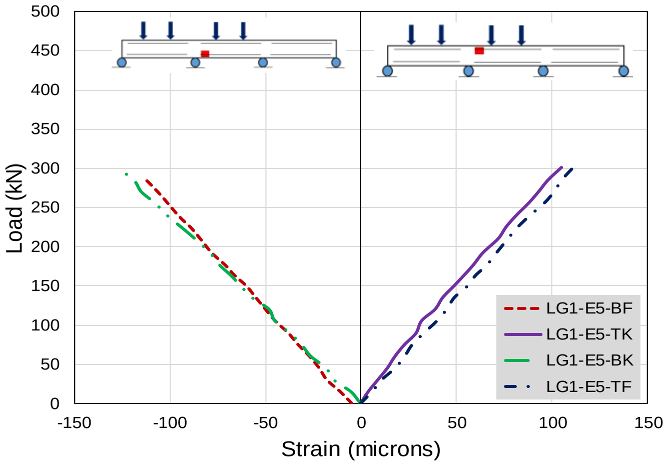

Figure 131 Strains values recorded at location E5 (Loading Setup SP-1-L03)

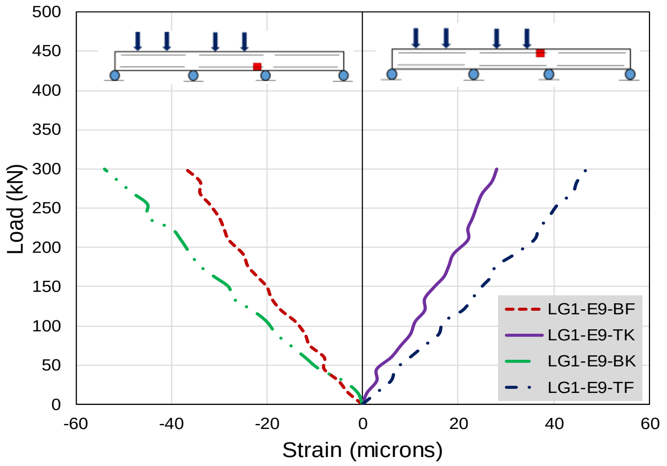

Figure 132 Strains values recorded at location E9 (Loading Setup SP-1-L03)

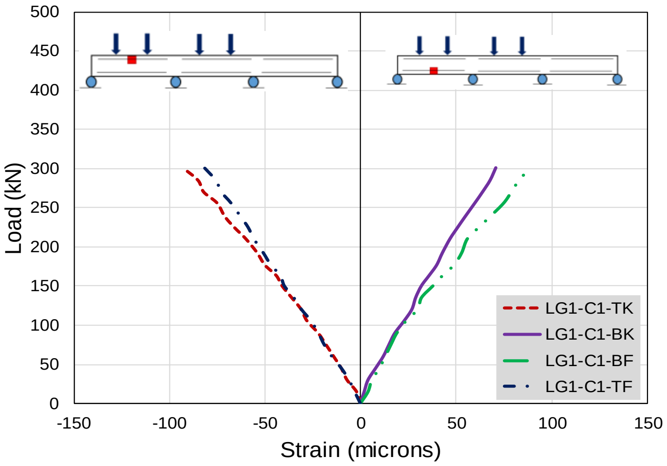

Figure 133 Strains values recorded at location C1 (Loading Setup SP-1-L03)

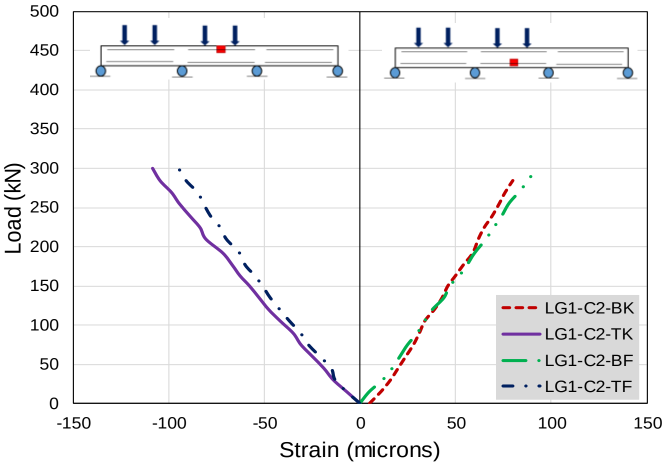

Figure 134 Strains values recorded at location C2 (Loading Setup SP-1-L03)

4.1.5.4 Type Four

4.1.5.4.1 Location E1-E3

At the exterior face of left interior support, maximum strain was recorded for the top longitudinal steel bars which were subjected to negative bending. Maximum positive strain recorded was around 1800 microns which is less than the yield strain of steel bars. On negative side, maximum recorded strain was limited to 950 microns (Figure 135).

4.1.5.4.2 Location E4-E6

Maximum positive and negative strains recorded at the interior face of left interior supports were 1500 and 800 microns, respectively. These strains were found to be significantly higher than those recorded under the same loading setup with load limited to service limits (see Figure 136).

4.1.5.4.3 Location E7-E9

Under 4-point loading at ultimate state, maximum positive and negative strains recorded at the interior face of right interior support were 200 and 350 microns, respectively. These strains were noticeably lower than those recorded at other supports and under the same loading (Figure 137).

4.1.5.4.4 Location C1

At location C1, positive and negative strains exhibited similar response at ultimate load under 4-point loading. However, maximum strains obtained in both directions were limited to 750 microns significantly lower than the yield strain (see Figure 29). Nonetheless, these strains were substantially higher than those recorded at the same location and loading setup but maximum load limited to service state (see Figure 138).

4.1.5.4.5 Location C2

At location C2, maximum positive recorded strain was lower than that recorded at location C1. However, negative strain achieved similar value to that of its counterpart at location C1. As shown in Figure 139, strain-load relation remained linear and maximum recorded strains did not achieve yield plateau. Maximum positive and negative strains recorded at this location and under 4-point ultimate load were 500 and 750 microns, respectively.

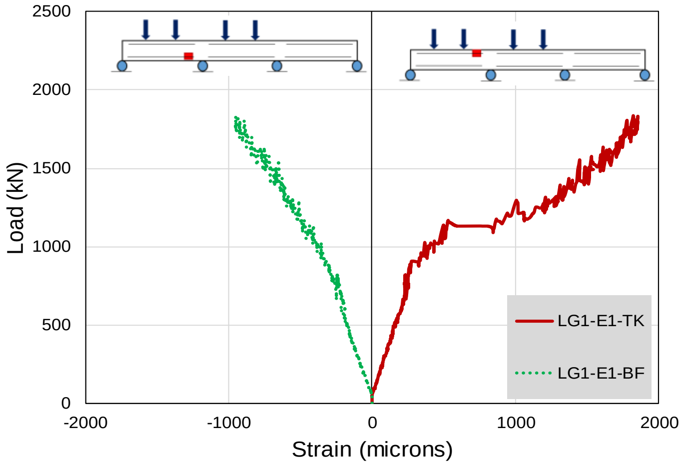

Figure 135 Strains values recorded at location E1 (Loading Setup SP-1-L04)

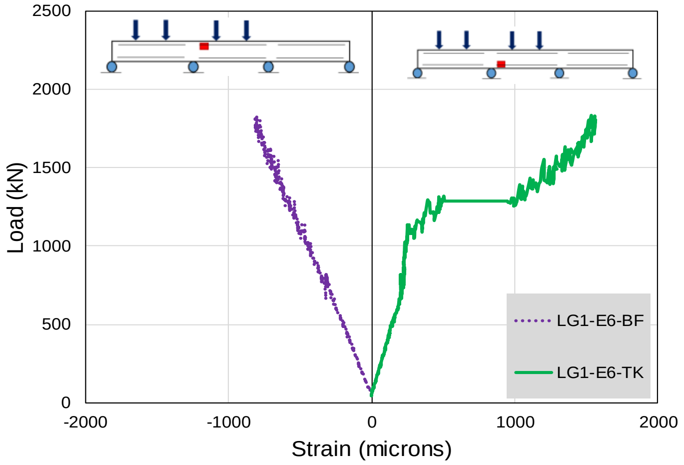

Figure 136 Strains values recorded at location E6 (Loading Setup SP-1-L04)

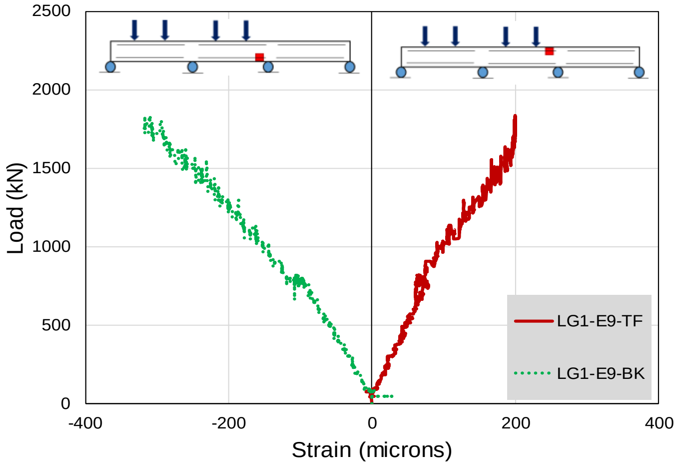

Figure 137 Strains values recorded at location E9 (Loading Setup SP-1-L04)

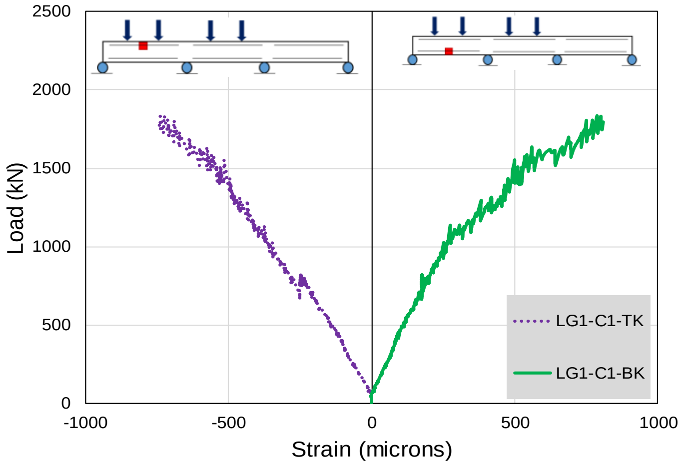

Figure 138 Strains values recorded at location C1 (Loading Setup SP-1-L04)

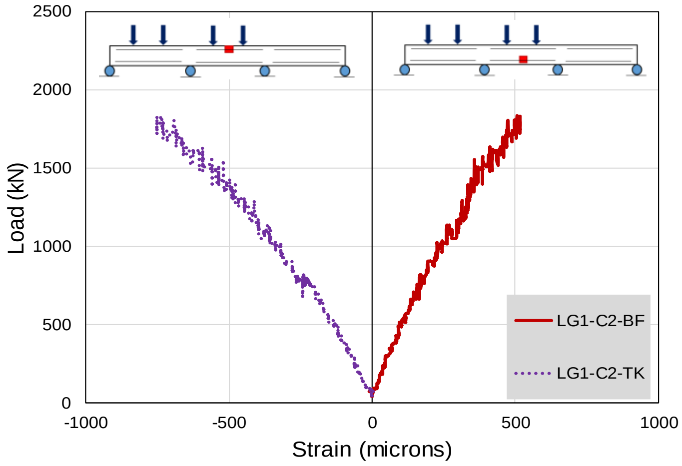

Figure 139 Strains values recorded at location C2 (Loading Setup SP-1-L04)

4.1.6 Transverse Reinforcement Strains

Strain gages were also mounted on stirrups of each specimen near their supports. At each support, strain were measured on 3 different stirrups. For each stirrup, one strain gage was attached to the front vertical side while another was attached to the back vertical side named SG1 and SG2, respectively. Further nomenclature of stirrup strain gages is shown in Figure 40.

4.1.6.1 Type One

This loading setup corresponds to the application of 2-point service load at right exterior span of specimen SP-1 (see Figure 14a). Corresponding strain gages in this load setup were E10-E12 (i.e., at exterior face of first right interior support) and D4-D6 (i.e., at right exterior support). Figure 140 shows stirrups strain distribution versus applied load for D4-D6. It can be seen that maximum strain recorded was below 100 microns which is significantly lower than the yield strain of stirrups. Recorded strains at location E10-E12 are presented in Figure 141. Maximum strains recorded here were noticeably lower than those recorded at D4-D6 with maximum value limited to 17 microns.

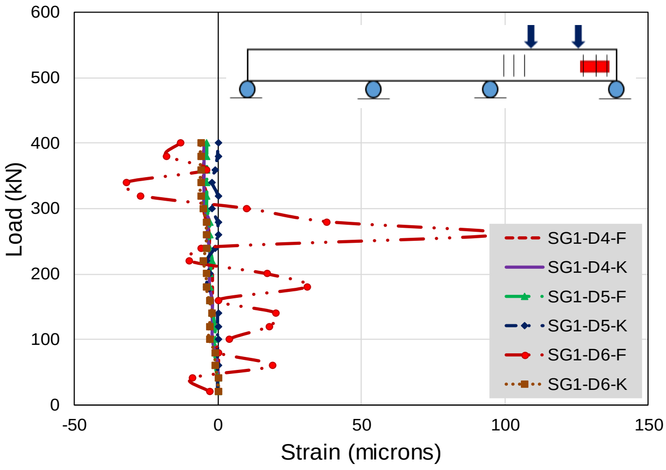

Figure 140 Stirrups strains recorded at D4-D6 (at right exterior support under loading setup SP-1-L01)

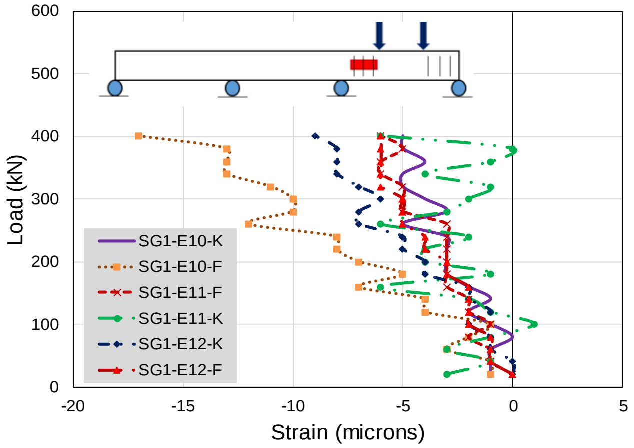

Figure 141 Stirrups strains recorded at E10-E12 (at exterior face of 1st right interior support under loading setup SP-1-L01)

4.1.6.2 Type Two

This load setup corresponds to the application of 2-point service load at interior span of specimen SP-1. Concerned stirrups strain gages under this setup were E4-E6 (at interior face of left interior support) and E7-E9 (at interior face of right interior support). Figure 142 shows the monitored strains for E7-E9 gages. Maximum strains were below 7 microns. Similarly, Figure 143 presents strains recorded at E4-E6 gages. It can be seen that maximum strains recorded at this location were slightly higher than 10 microns. Very small strain around 10 microns suggested that this span was not shear critical.

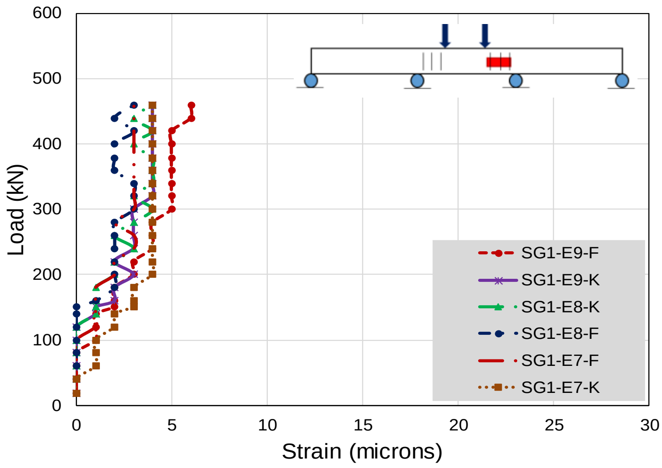

Figure 142 Stirrups strains recorded at E7-E9 (at interior face of right interior support under loading setup SP-1-L02)

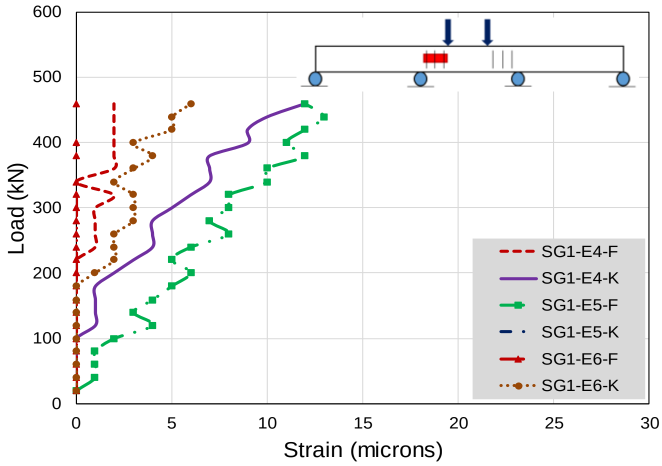

Figure 143 Stirrups strains recorded at E4-E6 (at interior face of right interior support under loading setup SP-1-L02)

4.1.6.3 Type Three

Under this loading setup, 4-point loading was applied to interior and left exterior spans up to the service limit. Concerned stirrup gage locations under this loading setup were D1-D3 (at left exterior support), E1-E3 (at exterior face of left interior support), E4-E6, and E7-E9. Corresponding strain data are plotted in Figures 144-147 respectively. Due to the damage of strain gages D2, D3, E1, and E3, only data of strain gage D1 and E3 are plotted in Figures 144 and 145, respectively. Maximum strains recorded at D1-D3, E1-E3, E4-E6, and E7-E9 were limited to 590, 5, 15, and 7 microns, respectively. It is evident that exterior span was shear critical as negligible stirrup strains were recorded within the interior span under 4-point service load.

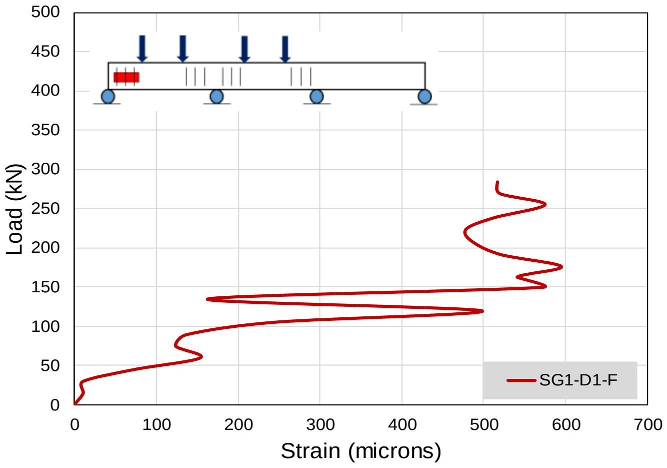

Figure 144 Stirrup strain recorded at D1 (at left exterior support under loading setup SP-1-L03)

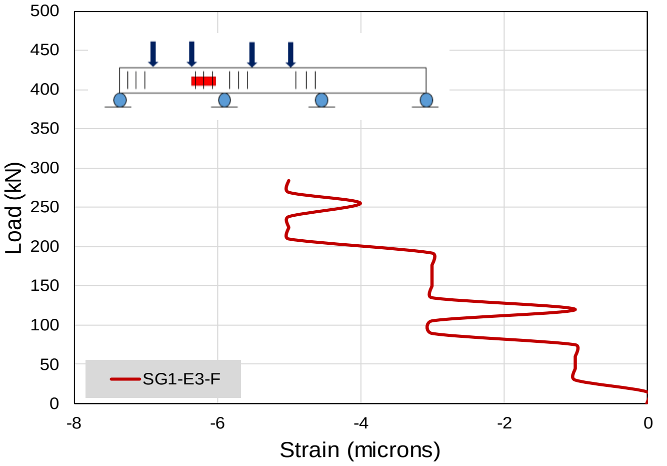

Figure 145 Stirrup strain recorded at E3 (at exterior face of left interior support under loading setup SP-1-L03)

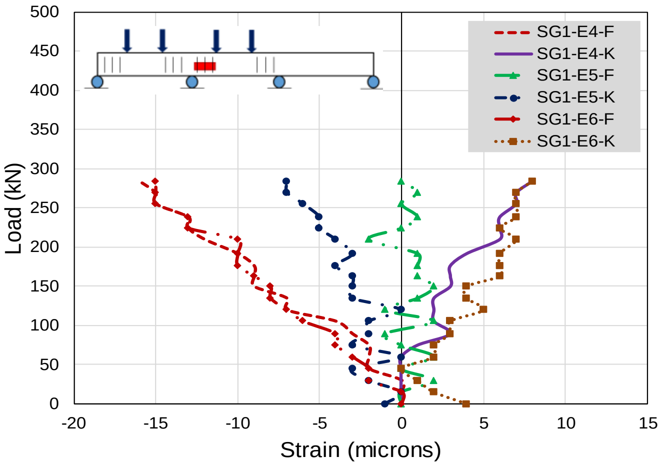

Figure 146 Stirrup strain recorded at E4-E6 (at interior face of left interior support under loading setup SP-1-L03)

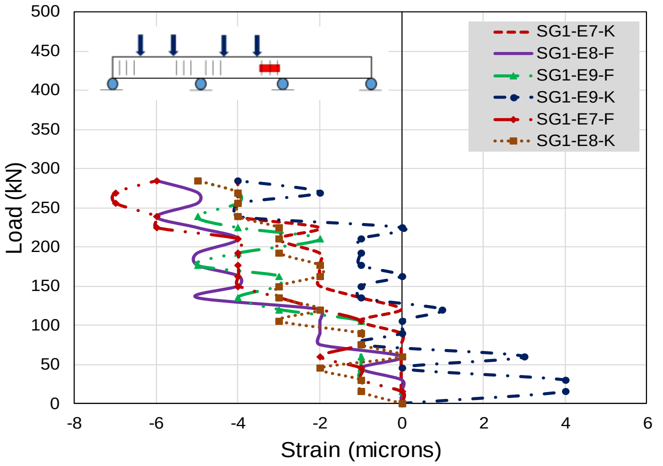

Figure 147 Stirrup strain recorded at E7-E9 (at interior face of right interior support under loading setup SP-1-L03)

4.1.6.4 Type Four

This loading was similar to SP-1-L03 but with an increased intensity of load to ultimate state. Concerned stirrup locations were again D1-D3 (at left exterior support), E1-E3 (at exterior face of left interior support), E4-E6, and E7-E9. Corresponding strain data are plotted in Figures 144-147, respectively. It is to be mentioned that unreliable data was obtained at D1-D3 location. Therefore, this data is not presented here for clarity. Some strain gages were also damaged at remaining locations. Therefore, only available strain gage data are plotted in Figures 148, 149, and 150 for locations E1-E3, E4-E6, and E7-E9, respectively. With reference to these locations, maximum strains were limited to 110, 400, and 15 microns for E1-E3, E4-E6, and E7-E9, respectively. Recorded strains were significantly lower than the yield strain of stirrups under ultimate load.

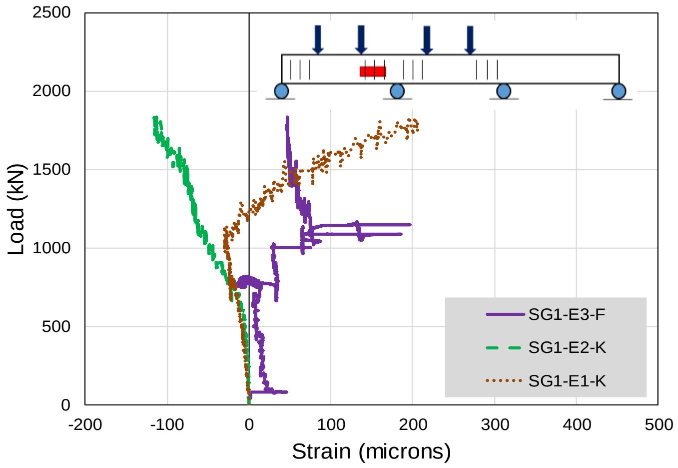

Figure 148 Stirrup strain recorded at E1-E3 (at exterior face of left interior support under loading setup SP-1-L04)

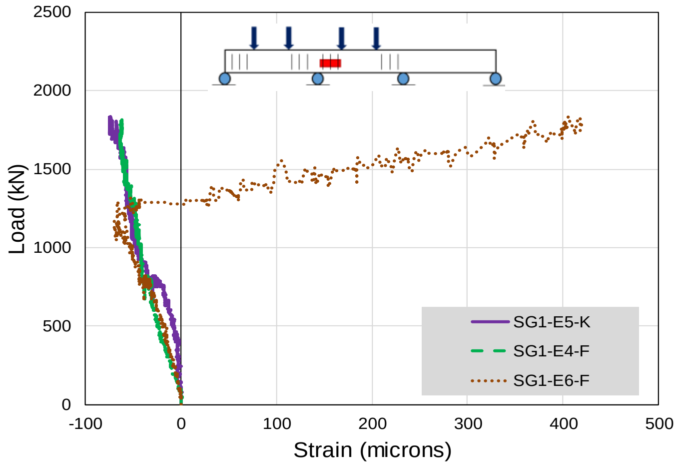

Figure 149 Stirrup strain recorded at E4-E6 (at interior face of left interior support under loading setup SP-1-L04)

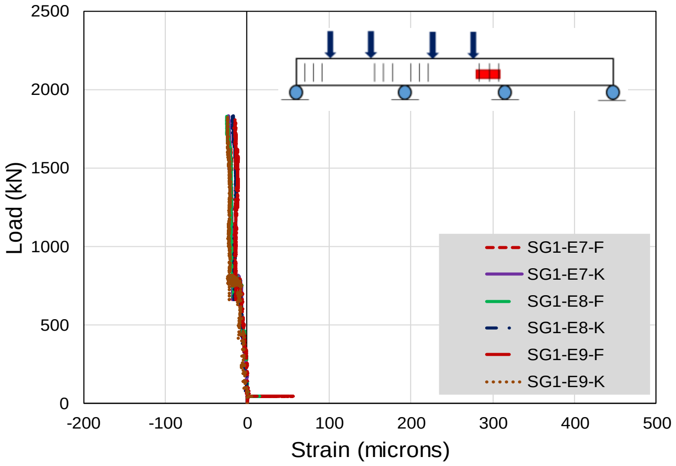

Figure 150 Stirrup strain recorded at E7-E9 (at interior face of right interior support under loading setup SP-1-L04)

4.1.7 Tendon Strains

4.1.7.1 Type One

Figure 151 and 152 presents recorded tendon strains at locations C3 and A3, respectively. Maximum recorded strains at these locations were 175 and 117 microns, respectively. It is to be mentioned that a number of strain gages on tendons failed and only reliable results are presented. Further, these strains remained well below the yield strains of tendons indicating no permanent damage to tendons under 2-point service loads on right exterior girder.

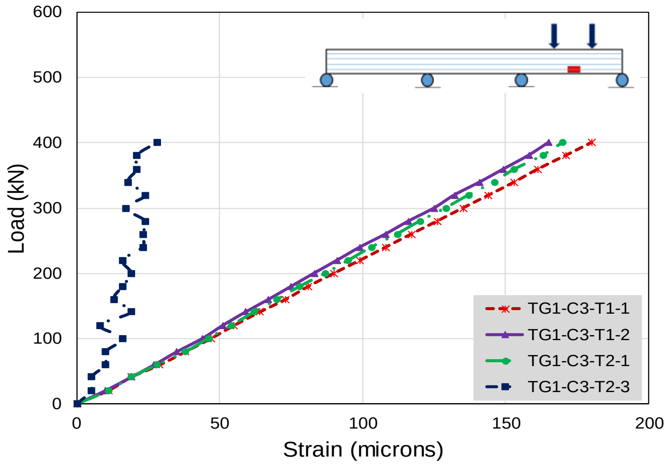

Figure 151 Tendon strains at location C3 (loading setup SP-1-L01)

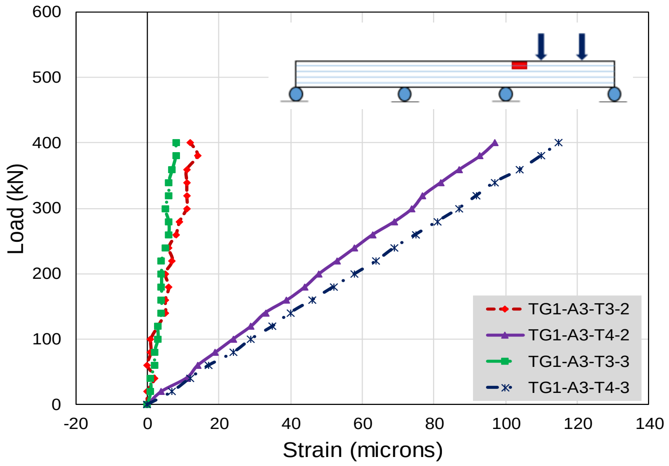

Figure 152 Tendon strains at location A3 (loading setup SP-1-L01)

4.1.7.2 Type Two

Under the application of 2-point service load on the interior span of specimen SP-1, recorded strains on tendons are presented in Figures 153 and 154 for locations A2 and C2, respectively. Since the loads were limited to the service load magnitude which are implicitly contained within the yield limits of the longitudinal steel bars, maximum tendon strains remained well below their yield limits with their magnitudes 125 and 170 microns at locations A2 and C2, respectively.

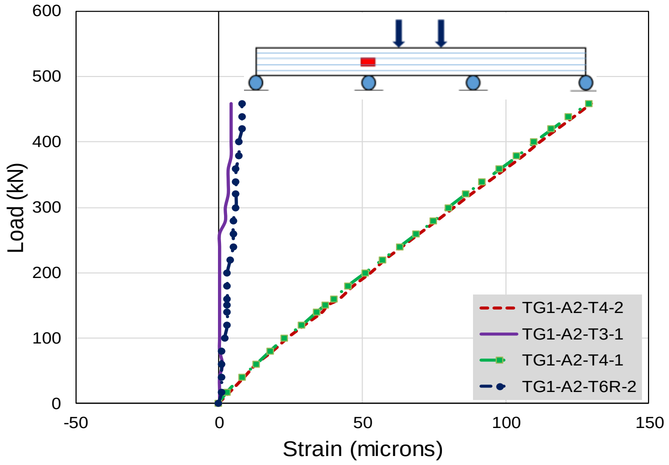

Figure 153 Tendon strains at location A2 (loading setup SP-1-L02)

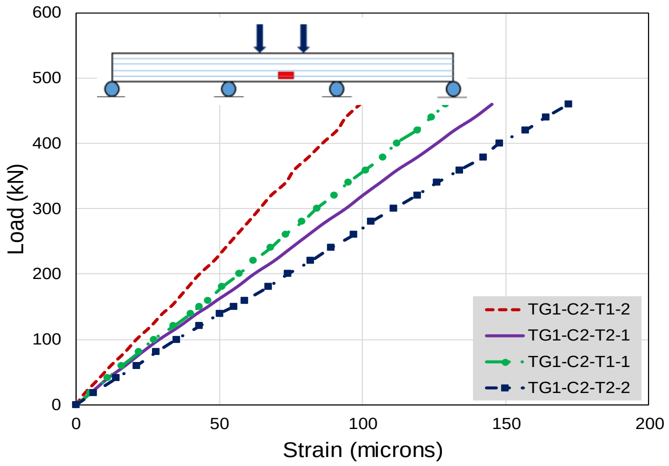

Figure 154 Tendon strains at location C2 (loading setup SP-1-L02)

4.1.7.3 Type Three

Figure 155 presents recorded tendon strains during the application of 4-point service load on specimen SP-1. It can be seen that strains remain linear at C1, A2, C2, and A3 locations with maximum recorded strains as 81, 125, 170, and 50 microns, respectively. This suggests that none of the tendons yielded during the application of 4-point service loads.

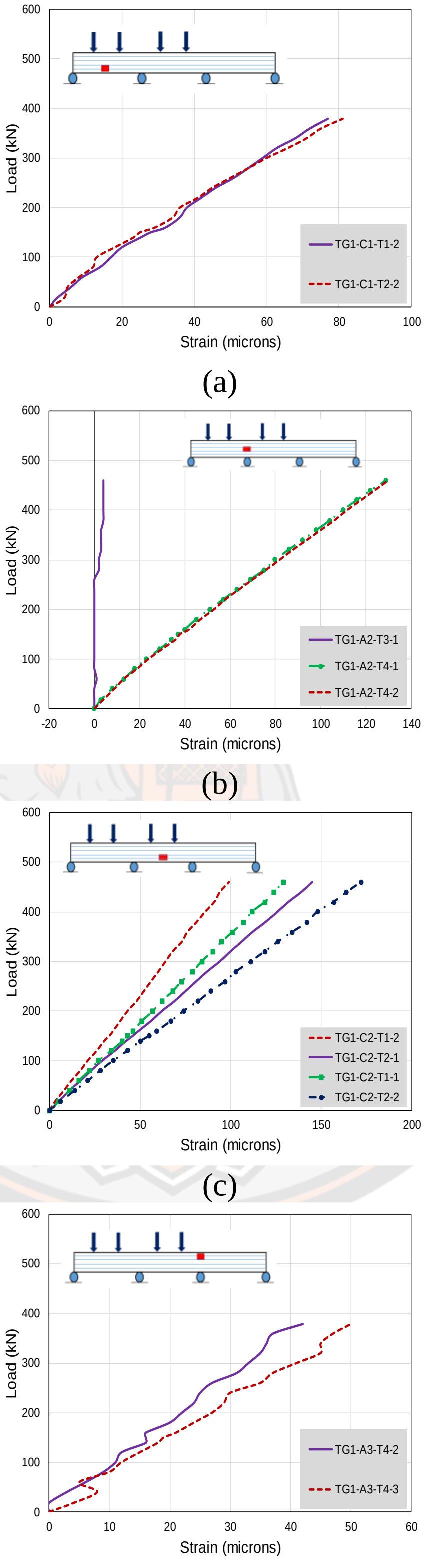

(a)

(b)

(c)

(d)

Figure 155 Tendons strains recorded during loading setup SP-1-L03 at locations (a) C1, (b) A2, (c) C2 (d) A3

4.1.7.4 Type Four

This loading setup corresponds to the application of 4-point ultimate loading on specimen SP-1. It can be seen from Figure 156 that tendons did not yield at locations C1, C2, and A3. Tendons strains in excess of their yield strains were only recorded at the left interior support with magnitude of approximately 4000 microns.

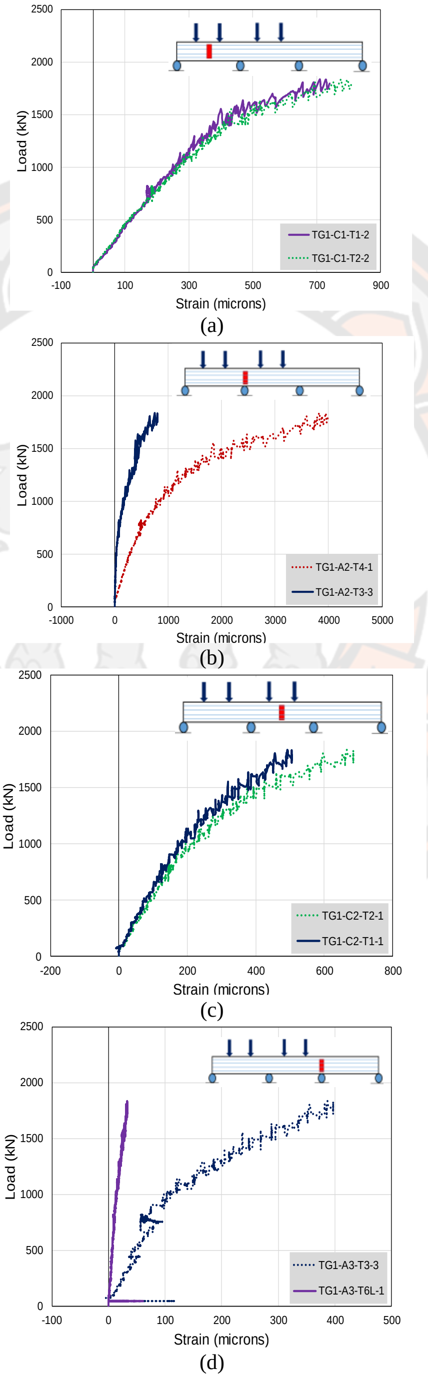

Figure 156 Tendons strains recorded during loading setup SP-1-L04 at locations (a) C1, (b) A2, (c) C2 (d) A3

4.1.8 Structural Factors

In this study, structural factors such as Factor of Safety (FOS) and Demand-Capacity-Ratio (DCR) are calculated based on the design and ultimate loads observed in the large-scale tests. The design service load and ultimate load of FPPC girder was 300 kN and 750 kN, respectively. Whereas the ultimate load recorded in the large-scale test was 2733 kN. c

4.1.9 Ductility of FPPC Girder

The ductility of reinforced concrete members is determined by calculating the ductility ratio. A higher ductility ratio shows that a beam may withstand significant deflections before failings. There are several techniques to defining ductility, which can be classified into two broad categories: energy and deformation-based methods. The most frequently used technique is one based on deformation, as indicated by the deformation margin between the ultimate stage and service stage. The ductility ratio is calculated using the deformation technique, as shown in Equation 1.

$$\mu D = \Delta u / \Delta y \qquad (1)$$

where μD represents the deformation-based ductility ratio, Δu represents the 400 ultimate mid-span deflection, and Δy represents the mid-span deflection during the service stage. In this study, the FPPC girder was tested under service loads for each span (sections 4.1.1.1 to 4.1.1.3) under loading conditions type one to three. Therefore, it is not possible to calculate the ductility ration of each girder by using the above equation. However, The FPPC girder was tested under ultimate conditions under loading type four. Further in the ultimate condition, the load versus deflection responses of middle girder was captured during the test as shown in Fig. 118. The calculated ductility ratio was approximately 21.20. Since a single FPPC girder was tested in this study, therefore, it is not possible to directly compare the performance of each girder in terms of ductility ratio. Future studies are recommended to further compare the ductility of each girder in FRRP girder system.

4.1.10 Behavior of Bearing

In this study, the monorail girder was mainly comprised of three reinforced concrete (RC) hollow haunched girders (one interior and two exterior girders), four piers or supports, two pier segments, four wet joints and four bearings at each support. A special system or bearing was designed to connect the pier segment with the bridge pier, as shown in Fig. 157. Monorail bearings were installed at support of girder which separated in 2 types; Fixed-bearing and Free-bearing which the difference for both bearing is movement in longitudinal direction of bearing (direction of movement has shown in Fig. 158). Configuration of bearing for test specimen in this study is consist of three Fixed-bearings and one Free-bearing (Figure 158). The design load data is given in Table 14. In the ultimate load test, the bearings at all supports remained undamaged (Figs. 159-161), except for the bearing at support S-1. The complete failure of bearing B-01 was observed, as shown in Fig. 162. At first, slight cracking of the non-shrink grout at bearing B-01 was observed following a sudden tensile rupture of the bearing bolts.

Figure 157 Typical view of bearing.

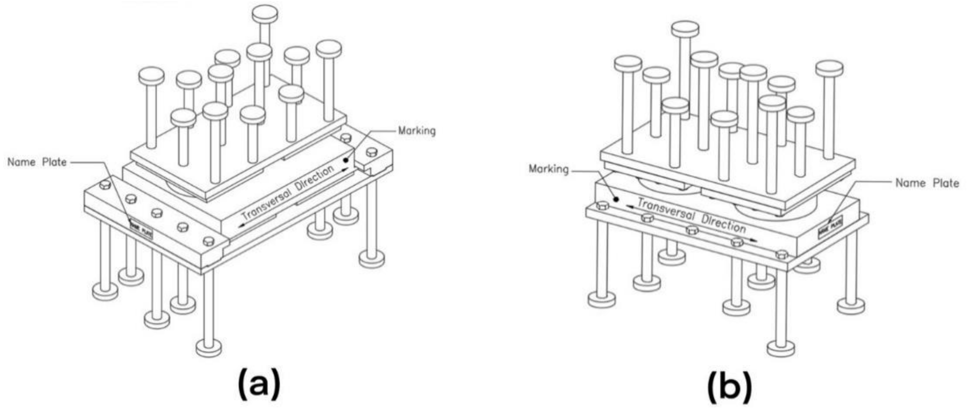

Figure 158 (a) Fixed-bearing and (b) Free-bearing

Figure 159 Bearing B-04 after test

Table 14 Monorail Bearing design loads data

Device		Vertical Loads (kN)		Horizontal Loads (kN)		Trans. Moment (kN)		Movement (mm)		Rotat.
Type	Code	SLS	ULS	SLS	ULS	SLS	ULS	Long.	Trans.	(±rad)
Fixed	FS-1	2,045	3,104	215	334	141	374	-	-	0.01
Free	GS-1	1,017	1,557	84	176	99	206	±50	-	0.01

Figure 160 Bearing B-03 after test

Figure 161 Bearing B-02 after test

Figure 162 Ultimate failure of bearing B-01.

4.1.11 Failure Mode of Girder

In the case of the first three types of loadings, i.e. loading types 1, 2 and 3, the FPPC girder remained undamaged. Also, concrete cracks were not observed at any location. Although crack gauges at all locations recorded some values in terms of crack width in these loadings, these values were very small and cracks were invisible. The ultimate failure mode of the FPPC girder under loading Type-4 was progressive and very destructive. The first crack was observed at an ultimate load of 550 kN at the middle span, as shown in Fig. 163 (a). As the load was further increased, i.e. at 650 kN, the first crack progressed upward. At the same time, new cracks were observed at the same span, as shown in Fig. 163 (b). At an ultimate load of 800 kN, vertical cracks were observed at the region of negative moments, i.e. at the locations of wet joints W-01 and W-02, as shown in Fig. 163 (c). As the load was further increased, the widening and further propagation of the cracks was observed at the middle span and wet joints (wet joints A and B). At an ultimate load of 900 kN, a vertical crack was also observed at the location of wet joints W-03 and W-04, as shown in Fig. 163 (d). The first crack at the middle of the left span was observed at an ultimate load of 1200 kN, as shown in Fig. 33 (e). Also at this stage, more cracks were observed at the middle span.

Meanwhile, the first crack at the top side of the right span was observed at an ultimate load of 2000 kN (Fig. 163 (f)). However, the bottom side of the right exterior span remained uncracked. At the ultimate state, very wide cracks were observed at the wet joints and middle span. Also, the severe splitting and crushing of the concrete was observed near support S-2, as shown in Figs. 164 and 165.

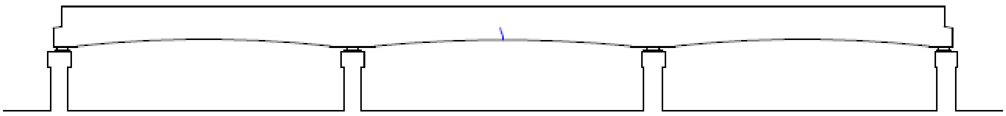

(a) Load = 550 kN

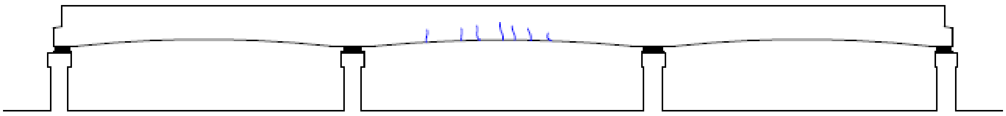

(b) Load = 650 kN

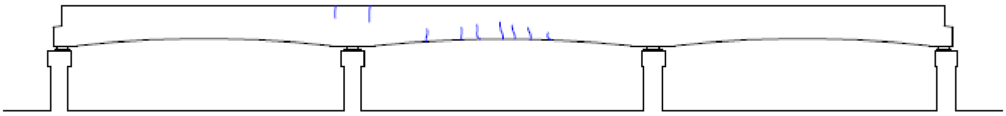

(c) Load = 800 kN

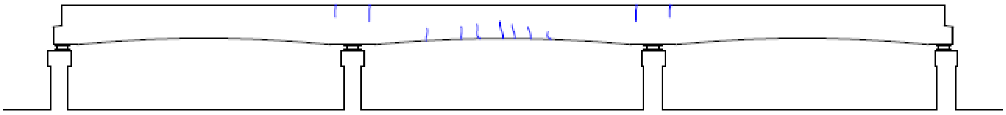

(d) Load = 900 kN

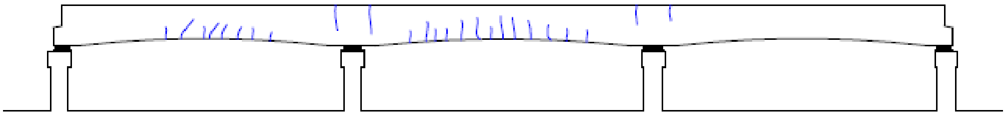

(e) Load = 1200 kN

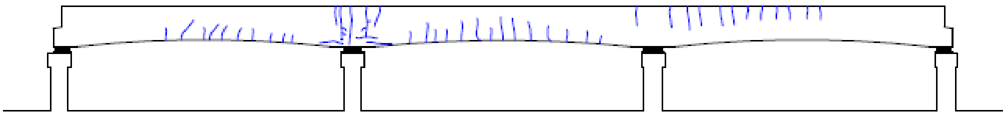

(f) Load = 2000 kN

Figure 163 Cracking pattern of the FPPC girder at different loads, a) 550 kN, b) 650 kN, c) 800 kN, d) 900 kN, e) 1200 kN, and f) 2000 kN

Figure 164 Cracking pattern at the pier segment.

(a) W-01　**(b)W-02**

Figure 165 Detailed cracking pattern at the pier segment.

4.2 Part B

4.2.1 Load-Deflection Response

This section summarizes and compares experimental load-deflection response of all beams. Firstly, comparison is made among group 1 beams. Then, subsequent comparisons are made among different beams on the basis of similarities in their geometric configurations. For instance, load-deflection response of beams B01, B04, and B07 are compared as they share the same section i.e., without any internal opening. Similarly, responses of beams B02, B05, and B08 are compared. Finally, the load-deflection response of beams B03, B06, and B09 are compared. Table 15 presents the summary of the key parameters obtained from load-deflection curve of each beam. Figure 166 presents load-deflection response of beams in group 1 (i.e., without CFRP strengthening). It can be seen that all 3 beams exhibited similar initial stiffness up to their cracking loads (though cracking loads slightly varied as mentioned earlier). Up to the yield load, beam with solid section i.e., B01 demonstrated highest stiffness of all followed by beam B02 and B03, respectively. Beam with 100mm opening experienced lowest yielding load among its counterpart beams. Nonetheless, yield deflection of all 3 beams were comparable.

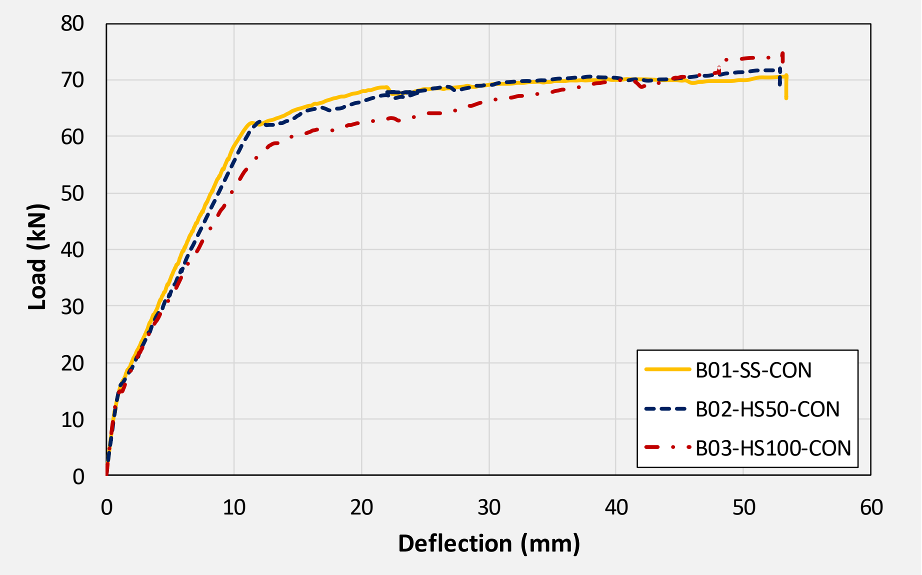

Figure 166 Comparison of load-deflection response of beams in 1st group (no CFRP strengthening)

Application of CFRP, irrespective of its configuration, improved the behavior of beams. Fig. 167 compares load-deflection response of beams B01, B04, and B07. These beams had solid section with beam B01 acting as control beam while beams B04 and B07 were furnished with CFRP sheet in configuration A and B, respectively. It can be seen that a U-shape CFRP was most effective in terms of improving initial stiffness, load corresponding to yield, and ultimate load. Ultimate loads of beams B01, B04, and B07 were 70.81, 86.22, and 112.81 kN, respectively. This corresponds to an increase of 22 and 59% in ultimate loads sustained by beams B04, and B07, respectively. However, post-peak behavior of strengthened beams were mainly limited by the performance of CFRP. As shown in Fig. 167, sudden drops were observed in load capacities for beams B04 and B07. This is attributed to the sudden de-bonding and rupture of CFRP in beams B04 and B07, respectively. It is to be mentioned that the rupture of U-shape CFRP was explosive and sudden resulting in larger degradation of load-capacity as compared to beam B04. Another interesting observation was that even after the rupture and de-bonding of CFRP sheets, load in beams B04 and B07 did not drop below the load carried by the control beam B01. This denoted the importance and effectiveness of CFRP in preventing any underlying damage to beams. Since, ultimate loads in CFRP strengthened beams were limited to either CFRP sudden de-bonding or rupture, corresponding deflections were noticeably lower than that of the controlled beam B01.

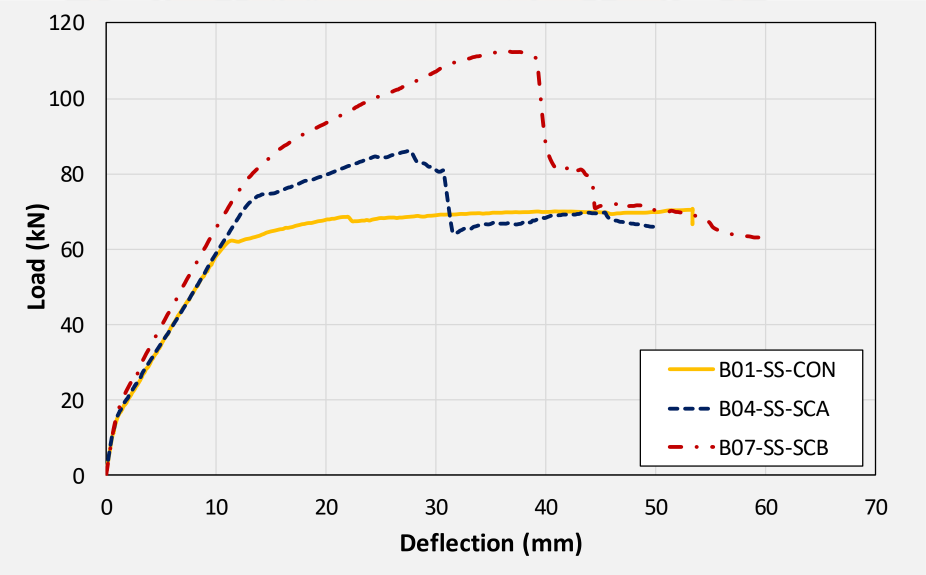

Figure 167 Comparison of load-deflection curves of solid beams

Figure 168 compares load-deflection response of beams with 50mm internal square opening. A similar discussion can be pertained to beams with 50mm square openings as it was made for solid section beams earlier. Application of CFRP sheet brought about significant improvements in initial stiffness, yield loads, and ultimate loads. An improvement of approximately 36 and 60% in ultimate loads was observed for beams B05 and B08, respectively. Again, application of U-shape CFRP sheet imparted higher improvement to load-capacity as compared to CFRP sheet on bottom side only. Analogous to beams in group 1, deflections against ultimate loads were limited ascribing to the sudden CFRP de-bonding and rupture resulting in an abrupt drop of load to the level of control beam B02.

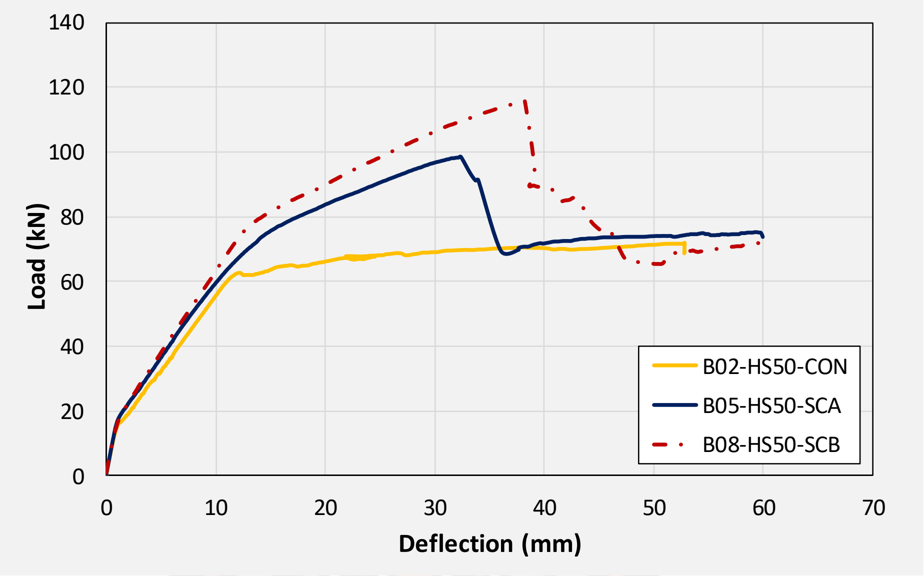

Figure 168 Comparison of load-deflection curves of beams with 50mm square opening

Figure 169 presents a comparison on load-deflection response of beams with 100mm opening. A similar trend as earlier beams was observed in the improvement imparted by CFRP sheets to the load-deflection response. An improvement of 16 and 53% in ultimate loads was observed for beams B05 and B08, respectively. Overall, U-shape CFRP sheet resulted in more improvement in ultimate loads regardless of the size and presence of internal opening. Whereas corresponding deflections at ultimate loads were mainly dependent on the behavior of CFRP sheets. Either de-bonding or rupture of

CFRP occurred abruptly causing sudden drop of load capacities. For solid sections and 50mm openings, drop in load as a result of either CFRP de-bonding or rupture was limited and did not fell below the threshold formed by the controlled beam. In case of beams with 100mm opening, concrete crushing at mid-span was highly pronounced. This caused the load to drop further below the one sustained by controlled beam B03. Typical concrete crushing sustained by 100mm CFRP strengthened beams is shown in Figure 170.

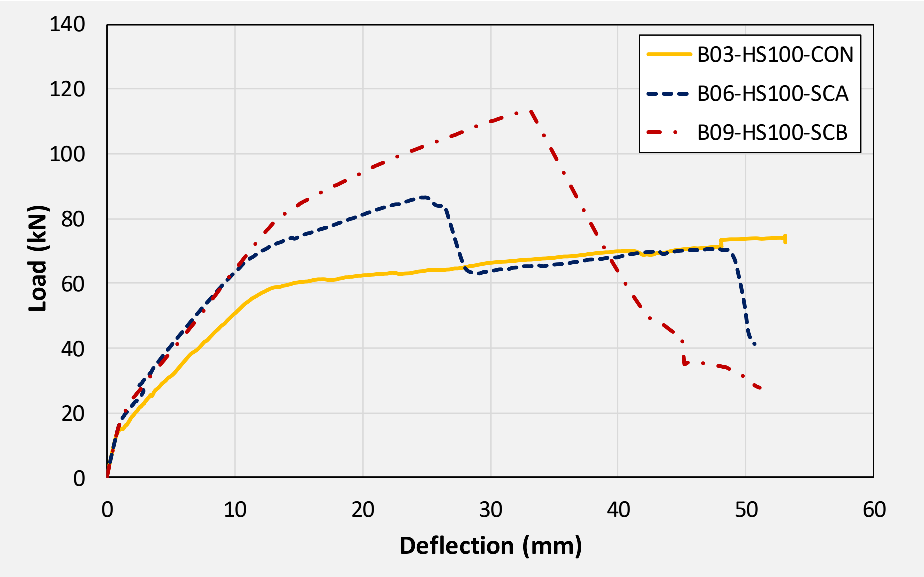

Figure 169 Comparison of load-deflection curves of beams with 100mm square opening

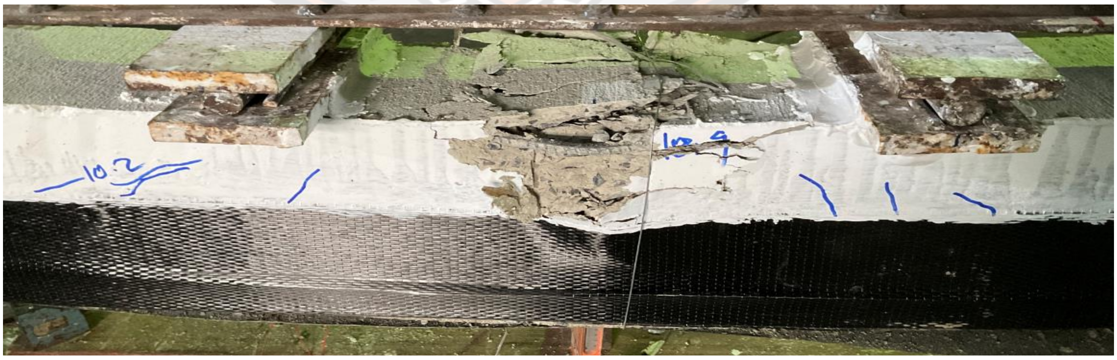

Figure 170 Pronounced concrete crushing observed in beams B06 and B09

Table 15 Key parameters obtained from load-deflection curves

Beam	Ultimate load (kN)	Increase in load (%)	Deflection* (mm)
B01-SS-CON	70.81	-	53.41
B04-SS-SCA	86.22	22	27.47
B07-SS-SCB	112.81	59	39.29
B02-HS50-CON	72.01	-	52.84
B05-HS50-SCA	98.52	36	32.35
B08-HS50-SCB	115.47	60	38.26
B03-HS100-CON	74.75	-	53.06
B06-HS100-SCA	86.51	16	25.00
B09-HS100-SCB	113.09	53	32.97

4.2.2 Steel Strains

Table 16 presents maximum steel strains monitored using strain gages attached to the top and longitudinal steel bars. Figure 171 presents strain monitored on bottom longitudinal steel bars at midspan of beams in group 1 i.e., beams B01, B02, and B03. It can be seen that strain gages in all beams reported strains well within their yield plateaus. This was expected in beam B01 having solid section and designed as under-reinforced. Presence of square openings of size 50 and 100mm did not transform the ductile response and all the beams were able to develop yielding in longitudinal bars.

Comparison of positive strains in solid-section beams is presented in Figure 172. It is apparent that the application of CFRP to beams helped mobilize higher strains in bottom steel bars in comparison to the control beam B01. This agrees with load-deflection responses of aforesaid beams. CFRP strengthened beams (B04 and B07) sustained higher loads than their corresponding control beam (B01). Consequently, higher moments were generated within their mid-spans. These higher moments were effectively resisted by bottom longitudinal steel bars which is reflected by their higher measured strains than those of the control beam. Maximum positive strains sustained by tension steel bars of beams B01, B04, and B07 were 8600, 9100, and 9300 microns, respectively.

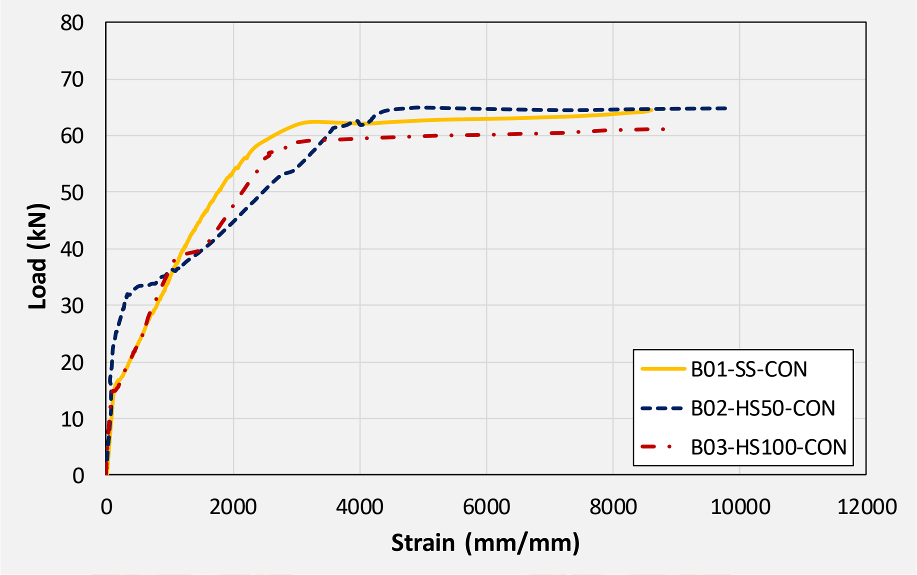

Figure 171 Monitored positive steel strain in beams B01, B02, and B03

A comparison of compression steel strains monitored on solid section beams is shown in Figure 173. It is to be noted that strain gage mounted on compression steel bar of beam B07 failed prematurely, and reliable strain data could not be extracted. It can be observed that the demand on compression longitudinal steel in CFRP strengthened beam remained similar to that in control beam. However, compression steel in post-yield regions experienced higher strains as compared to its counterpart steel in control beam. This can be reflected in that CFRP strengthened beam experienced higher moments in their midspans as compared to the control beams. Consequently, higher compressive stresses were generated in the cross-section above their neutral axes resulting in higher compressive strains. This may be the reason that CFRP strengthened beams sustained larger concrete crushing at their midspans as compared to those experienced by control beams.

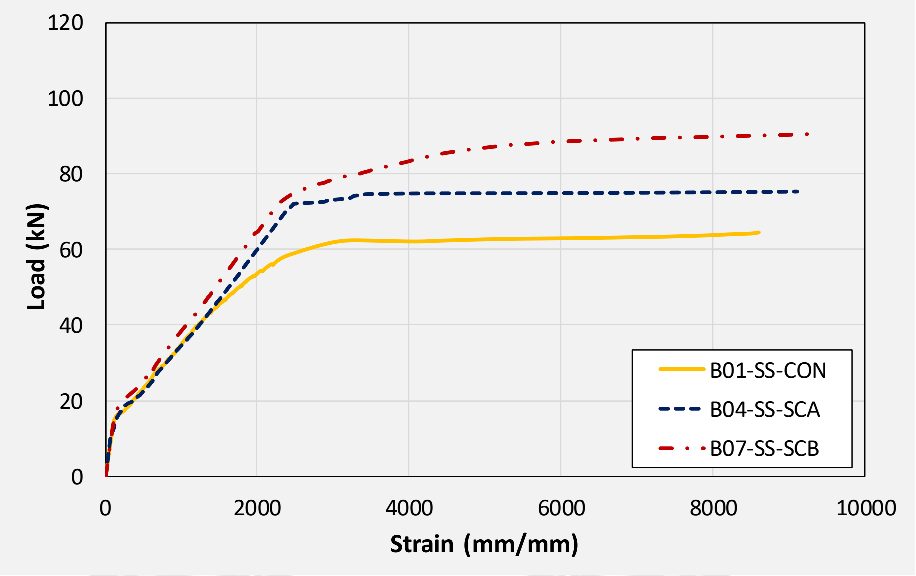

Figure 172 Monitored positive steel strain in solid section beams

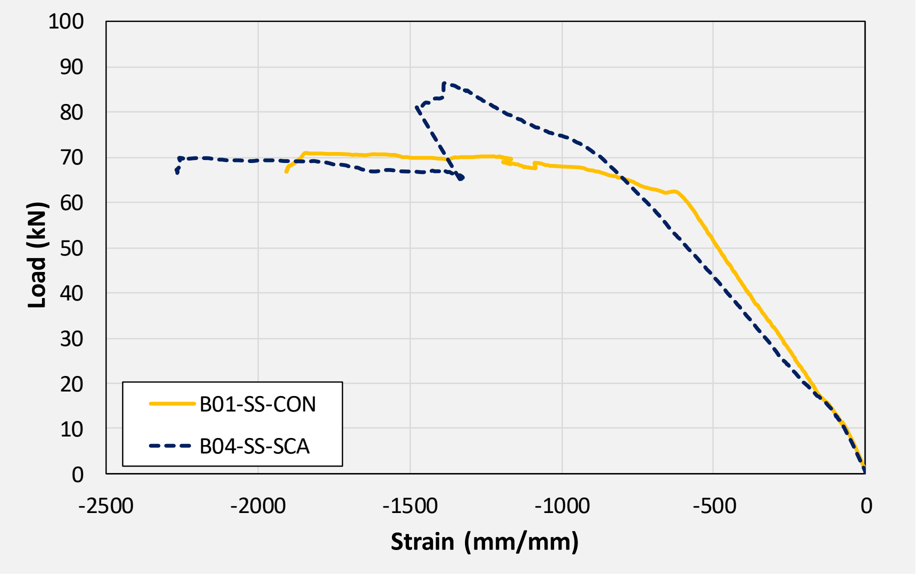

Figure 173 Monitored negative steel strain in solid section beams

Figures 174 and 175 present monitored positive and negative strains, respectively, on longitudinal steel bars in beams with internal 50mm square opening. Contrary to the maximum strain magnitudes in solid section beams, maximum strains monitored decreased with CFRP strengthening. For instance, beams B02, B05, and B08 recorded 9829, 9115, and 8710 microns, maximum positive steel strains, respectively. This may be ascribed to the efficacy of CFRP in reducing demand on tensile steel slightly. This effect was more pronounced in U-shape CFRP attached to beam B08 as compared to the single CFRP sheet bonded to beam B05's soffit. Magnitude of negative strains increased as a result of CFRP strengthening due to previously explained reasons. Analogous to solid section beams, sudden drop in strain-load profiles was seen coincidental with the sudden drop in peak loads as a result of abrupt debonding of CFRP. Table 16 summarizes peak compressive and tensile longitudinal steel strains in beams with 100mm internal square openings. It can be seen that maximum negative strains in beam B03 barely exceeded 1500 microns. However, beams B06 and B09 registered maximum negative steel strains of 20882 and 10986 microns, respectively. Magnitude of negative strain recorded in beam B09 was limited to 10986 microns due to the malfunction of strain gage attributed to large concrete crushing within its vicinity.

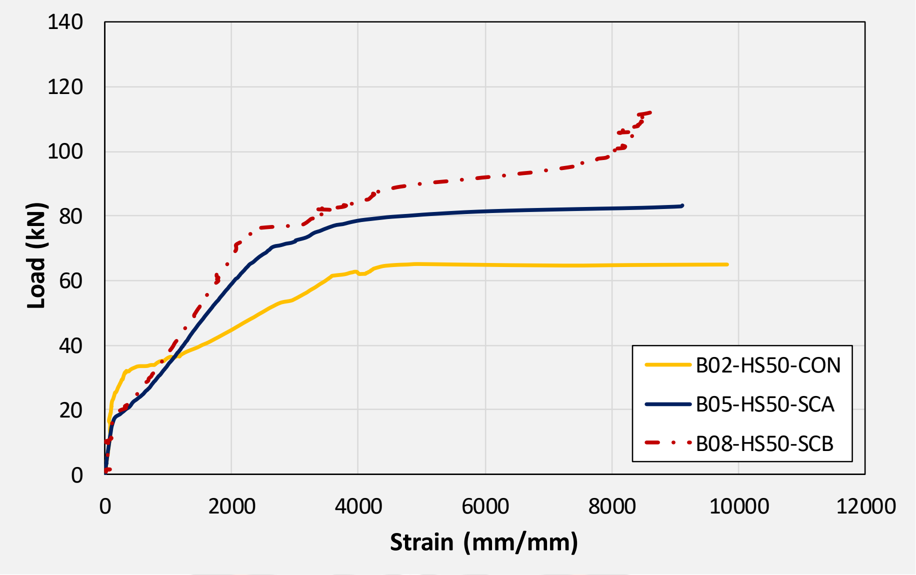

Figure 174 Monitored positive steel strain in beams with 50mm internal square openings

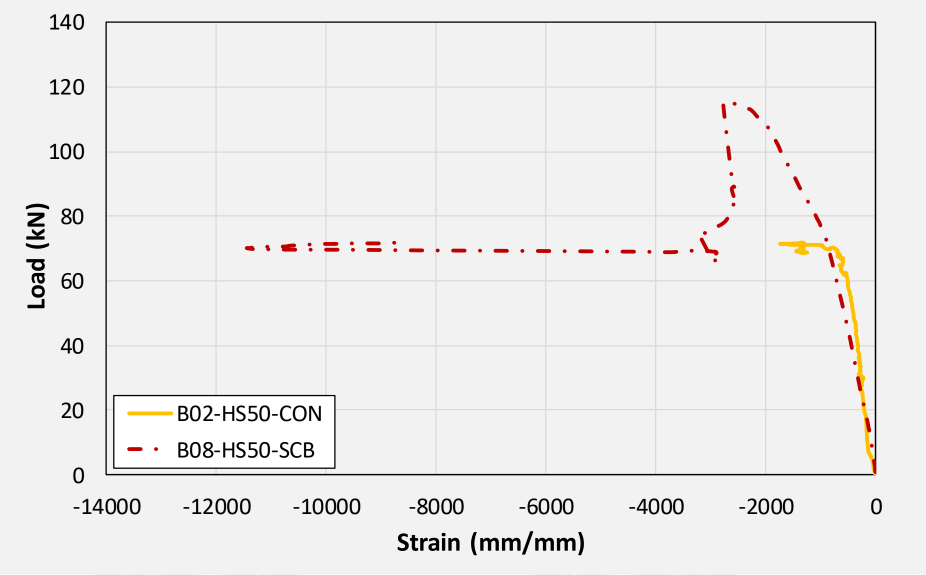

Figure 175 Monitored negative steel strain in beams with 50mm internal square openings

Table 16 Summary of maximum strains monitored on longitudinal steel bars

Beam	Strain (tensile)	Strain (Compression)
B01-SS-CON	8608	1906
B02-HS50-CON	9829	1726
B03-HS100-CON	8991	1501
B04-SS-SCA	9111	2266
B05-HS50-SCA	9115	-
B06-HS100-SCA	7612	20882
B07-SS-SCB	9299	-
B08-HS50-SCB	8710	11451
B09-HS100-SCB	8916	10986

4.2.3 Energy Dissipation

The energy absorption capacity of solid and hollow sections RC beams was defined as the area under the curve, i.e., load versus deflection curves. The energy dissipation for final step in load versus deflection was ignored as recommended in other studies. Table 17 presents the amount of energy dissipated by each beam calculated from the area under their respective load-deflection curves. Comparing energy dissipated by un-strengthened beams, maximum energy was dissipated by the solid section (B01) beam followed by beams with 50mm and 100mm openings, respectively. A comparison for dissipated energies by solid section beams revealed that lowest energy was dissipated by beam B04 (strengthened with CFRP sheet on bottom side only) followed by the un-strengthened beam B01 and beam B07 (strengthened with U-shape CFRP sheet). For beams with 50mm internal openings, un-strengthened beam B02 dissipated lowest energy followed by beams B05 (bottom CFRP sheet) and B08 (U-shape CFRP), respectively. A similar trend was also observed for beams with 100mm internal openings where maximum and minimum dissipated energy bounds were created by beams B09 (U-shape CFRP) and B03 (un-strengthened), respectively.

Table 17 Energy dissipated by beams

Beam	Energy dissipation (kN-mm)
B01-SS-CON	3302
B02-HS50-CON	3240
B03-HS100-CON	2784
B04-SS-SCA	3257
B05-HS50-SCA	4301
B06-HS100-SCA	3293
B07-SS-SCB	4750
B08-HS50-SCB	4301
B09-HS100-SCB	3638

4.2.4 Failure Modes

Beam B01 was a solid section beam without any external CFRP support. This beam behaved in a very ductile way as expected given that it was designed as an under-reinforced section. Cracking load was observed to be 22 kN with first noticeable flexural crack appearing at its midspan. With the increase in load, further flexural cracks appeared within the constant moment zone as shown in Figure 176. Crushing of concrete at the top of its midspan was observed at a load of 69kN. Final failure mode was accompanied by the yielding of longitudinal reinforcement and concrete crushing at the top of its midspan. These results are in consistent with the previous studies. Its failure was a typical representation of ductile failures associated with under-reinforced sections. Second beam in group 1 was furnished with a concentric internal square opening of 50mm size. This beam behaved in a similar way as the 1st beam B01 (see Figure 177). However, the presence of an internal opening reduced its effective flexural rigidity, thus, enabling an earlier formation of flexural cracks at its midspan. Its cracking load was observed at 16 kN. Concrete crushing was observed at a load of 71 kN that, compared to beam B01, corresponds to a slight increase. Nonetheless, beam B02 experienced a ductile failure analogous to beam B01. An increased opening size in beam B03 did not govern its general behavior as it underwent a ductile failure as well (see Figure 178). However, its cracking load was further deteriorated to 15kN. Ultimate loads of beams B01, B02, and B03 were recorded as 70.81, 72.01, and 74.75 kN, respectively. Another noticeable observation was the occurrence and position of cracks. Beam B03-HS100-CON mobilized more cracks near its supports followed by beam B02 and B01, respectively. In the past, similar cracking patterns have been also reported.

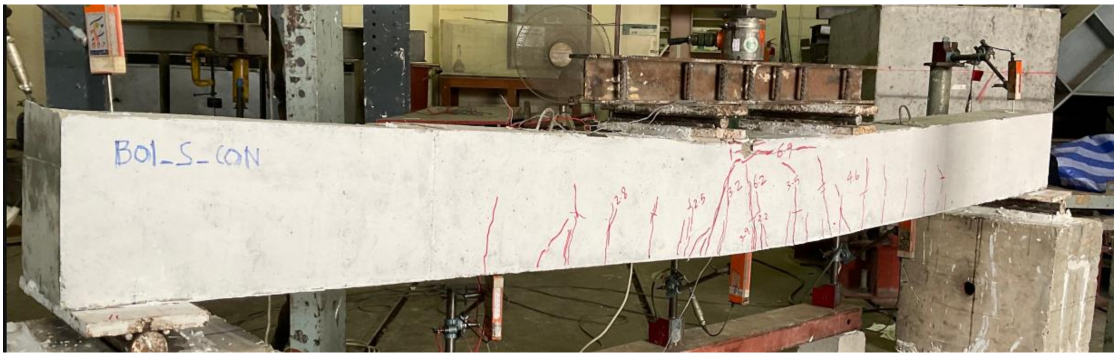

Figure 176 Failure mode of beam B01-SS-CON

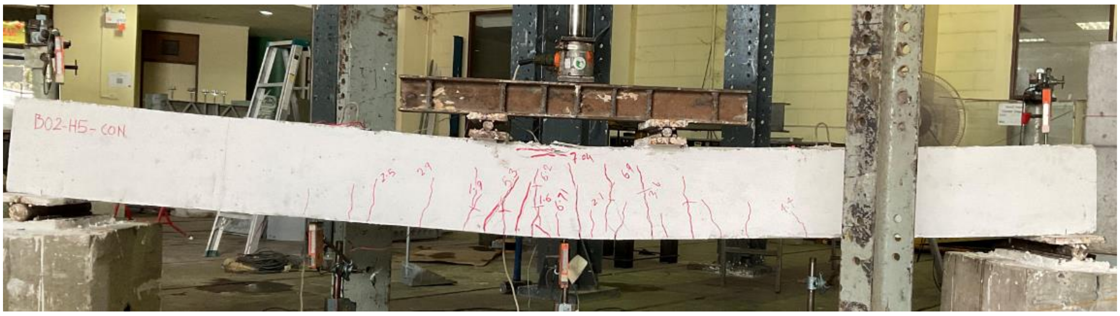

Figure 177 Failure mode of beam B02-HS50-CON

Figure 178 Failure mode of beam B03-HS100-CON

Beams in 2nd group were strengthened with a single CFRP layer on their bottom sides only. Beam B04, with a solid section, has its final failure shown in Figure 179. With the application of CFRP, cracking load was slightly increased to 23.1 kN. This beam also performed in a ductile manner. Ultimate failure of this beam accompanied sudden de-bonding of CFRP layer. Onset of debonding initiated at its midspan and proceeded towards supports (see Figure 180). Second beam in this group was B05 that furnished an internal square opening of 50mm. Application of CFRP sheet at the bottom side increased its cracking load to 20 kN (i.e., comparing with the cracking load of beam B02). This beam also experienced CFRP debonding at its ultimate failure. Nonetheless, an improved ductile behavior was observed as compared to its counterpart control beam in group 1 i.e., B02. Higher concrete crushing was observed at its midspan as compared to that observed in beam B04. Beam B06 exhibited in a similar way to other 2 beams in this group. Its failure was ductile limited to CFRP debonding and experienced highest amount of concrete crushing at its midspan in this group (see Figure 181). In the past, sudden deboning of CFRP from the RS beams has been also reported in the many studies.

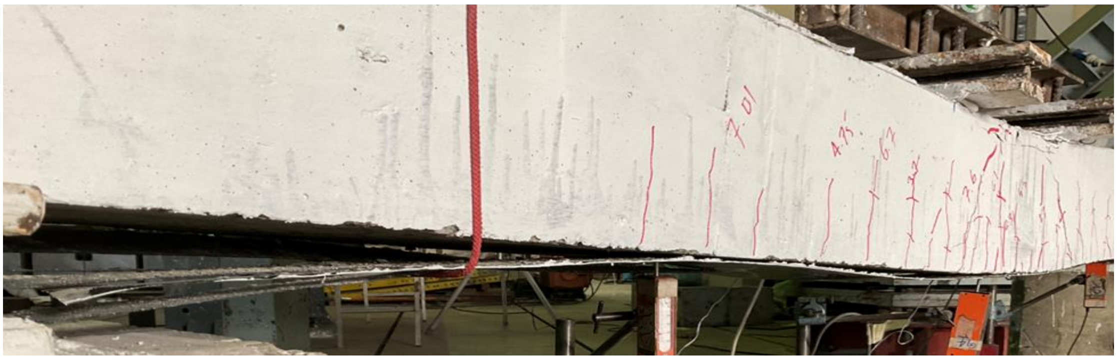

Figure 179 Failure mode of beam B04-SS-SCA

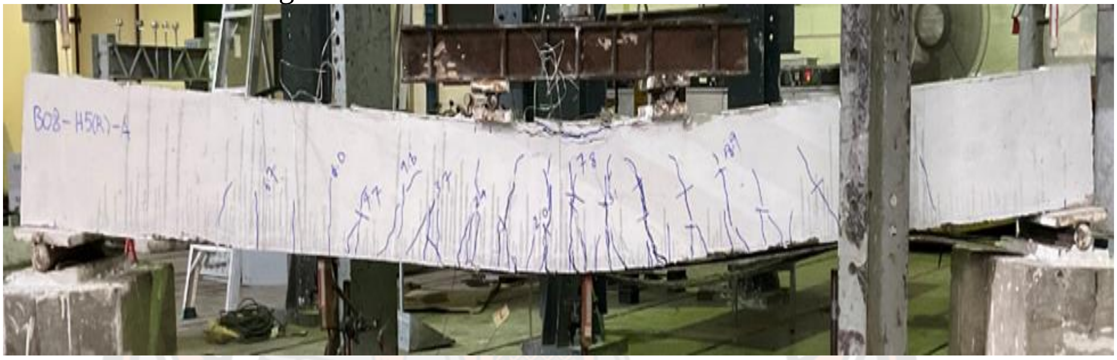

Figure 180 Failure mode of beam B05-HS50-SCA

Figure 181 Excessive concrete crushing observed in beam B06-HS100-SCA

Three beams (i.e., B07, B08, and B09) in 3rd group were strengthened with a single U-shape sheet each. In terms of behavior and failure modes, beams in 3rd group were almost identical to those in group 2. All beams exhibited a ductile response. However, CFRP sheet experienced a sudden and explosive rupture near corners of beams in transverse direction. It is to be mentioned that CFRP used was unidirectional with its main fibers aligned transverse to the longitudinal axis of beams. Rupture of CFRP fibers was not observed in their longitudinal direction. Though, a corner radius of 30mm was provided along bottom transverse corners of beams in this group, it could still not prevent stress concentrations resulting in CFRP rupture. A typical failure mode of beams in this group is presented in Figure 182.

Figure 182 Typical CFRP rupture observed in 3rd group

4.2.5 Correlation of large-scale and Small-scale Tests

It is well known fact that the testing of large scale monorail scale girders is very high cost, time consuming and un-affordable. Therefore, small-scale tests are usually planned to study the different research parameters within affordable budgets and other sources. In this study, small-scale tests were also conducted to study the different parameters such size of openings and strengthening configurations. In the small-scale tests, a total of 9 reinforced concrete beams with and without hollow openings were tested. Beams were categorized into three main groups depending upon the presence or configuration of adopted strengthening scheme. Each group contained 3 beams: one without any opening i.e., having a solid cross-section, one with an internal opening of 50 x 50 mm and one with an internal opening of 100 x 100 mm. All openings were made to coincide with the geometric center of beams. To increase the flexural strength of beams with internal openings, group 2 and 3 beams were strengthened with CFRP sheets. Configuration of CFRP sheets was varied in group 2 and 3. Group 2 beams were strengthened with a single CFRP layer applied to their tension sides only thereafter called as configuration A (SCA). Beams of group 3 were strengthened with a U-shaped CFRP sheet applied to their tension sides thereafter called as configuration B (SCB). Following results of small-scale tests could be used to develop correlation between smalls-scale and large-scale tests in this study.

1. The figure 165 shown that the load versus deflection responses of solid and hollow section beams are almost identical. Thus the use of hollow-section girders for Precast Post-Tensioned Continuous (PPC) girder for straddle monorail is suitable and affordable solution to reduce the cost of the project.
2. Further, there might be increase in the load on the large-scale Precast Post-Tensioned Continuous (PPC) girder for straddle monorails under different situations such as environmental issues and usage. The small-scale tests have shown that the CFRP composites are very effective to enhance the ultimate load carrying capacity of hollow sections. Thus, the CFRP composites could be used for Precast Post-Tensioned Continuous (PPC) girder in case there is a need to enhance the load carrying capacity of the large-scale Precast Post-Tensioned Continuous (PPC) girders.

4.3 Part C

4.3.1 Finite element analysis results

4.3.1.1 Load versus Deflection Responses

The finite element analysis (FEA) results in terms of load versus displacement (Y direction) are shown in Figs. 183-185 for different load conditions such as service load on right exterior girder, service load on interior girder, combined service load on left exterior and interior girder and combined ultimate load on left exterior and interior girder. The finite element analysis results are only presented and discussed for a single location i.e., middle of each span. Also, the experimental results i.e., load versus displacement in Y direction are also presented in Figs. 183-185 for the comparisons purposes. It can be seen that the finite element analysis results are in close agreement with the experimental results in each load type. In general, the experimental stiffness and ultimate displacement were observed higher than the finite element analysis. This phenomenon could be associated to the different errors during the instrumentation and experimental observations. The FEA results in terms of complete load versus deflection relationships are shown in Figures 188-190 for different loading conditions. Although in the experimental program only service load was considered in first and second loading condition, however, in FEA, ultimate load was also considered in both first and second loading condition to obtain the complete load versus deflection relationships. In Figure 188-190, the descending curves (curves beyond peak or ultimate load) are shown up to approximately 15-20% drop in the ultimate load because in FEA, it was not possible to capture the complete descending curves of load versus deflection relationships beyond 15-20% drop in the ultimate load due to convergence problems in ATENA. The FEA results indicate highest increase in the ultimate in the case of first loading condition i.e., two-point load applied at the right exterior beam and highest mid-span deflection was observed in the case second loading condition i.e., two-point load applied at the interior beam. Further experimental and analytical studies are needed to precisely study the effect of different loading conditions on the ultimate load carrying capacity and deflection of different girders in precast post-tensioned continuous girder system.

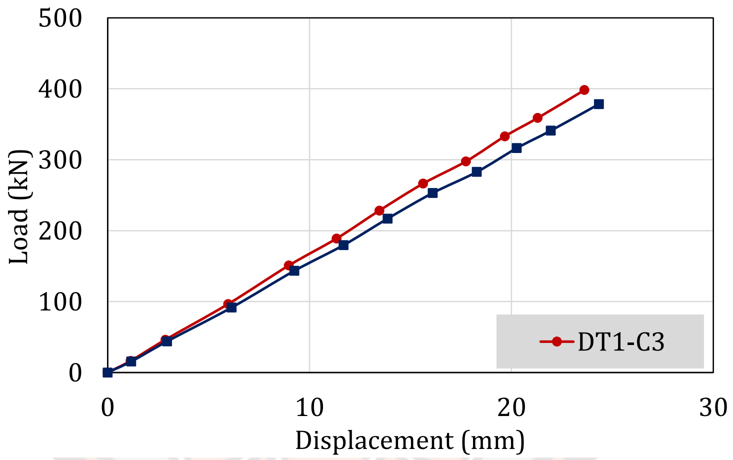

Figure 183 FEM versus experimental results– Service load at righter exterior girder

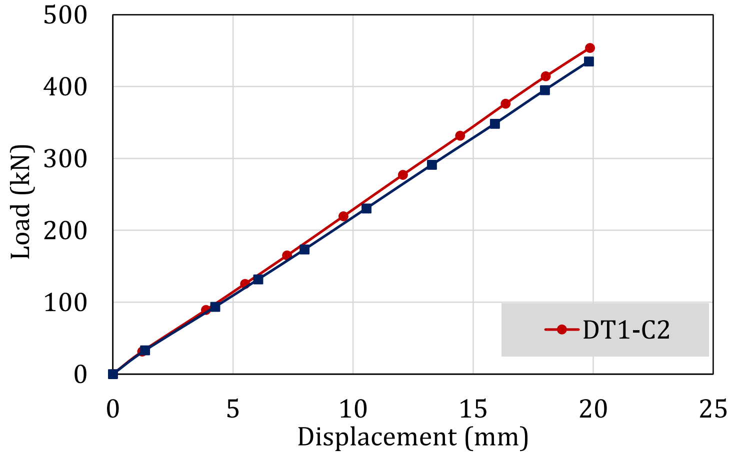

Figure 184 FEM versus experimental results– Service load at middle girder

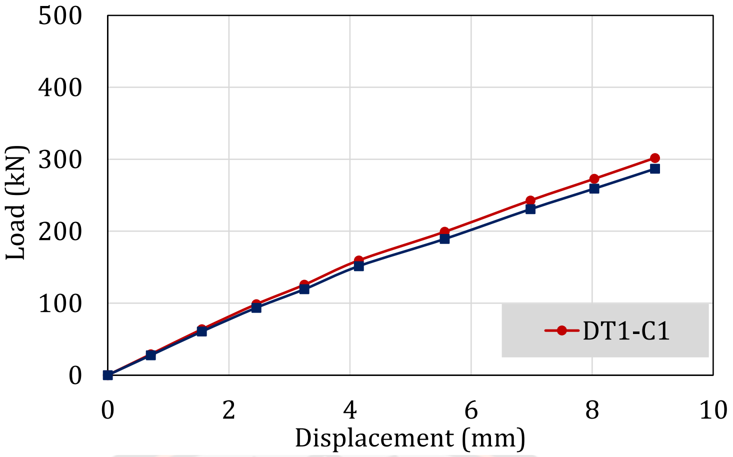

Figure 185 FEM versus experimental results – Combined service load at left exterior and middle girder

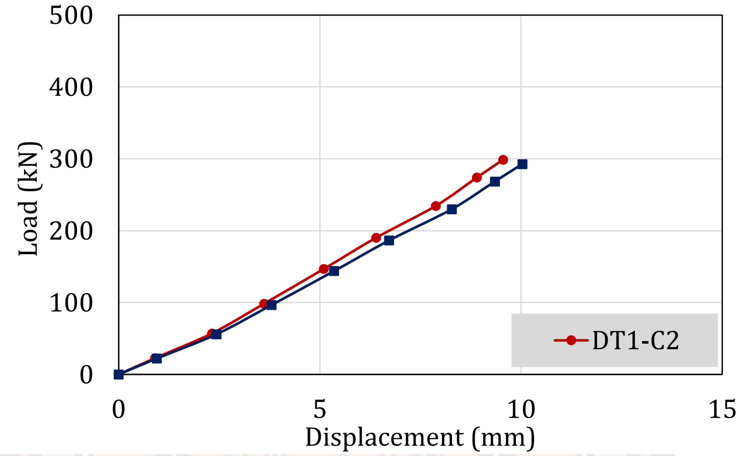

Figure 186 FEM versus experimental results of left exterior girder – Combined service Load at left exterior and middle girder

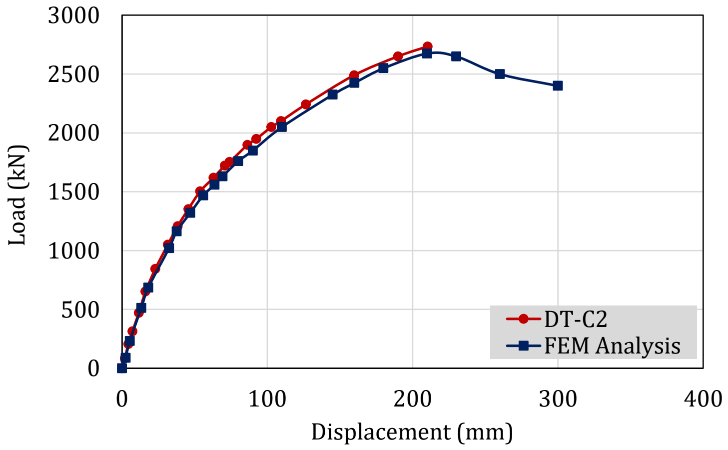

Figure 187 FEM versus experimental results of interior girder – Combined ultimate Load at left exterior and middle girder

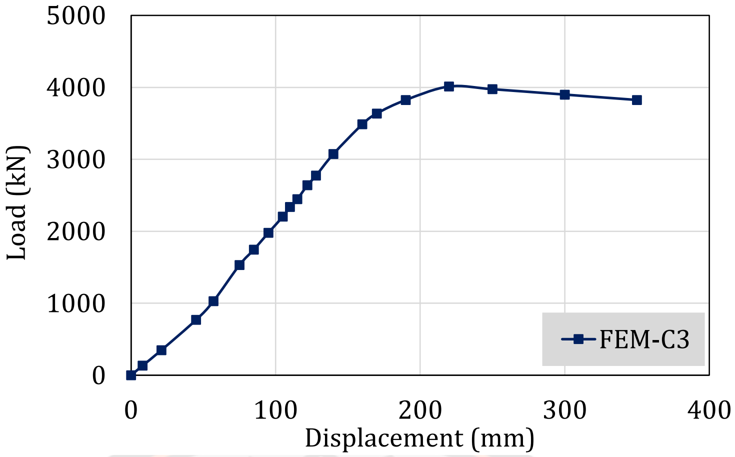

Figure 188 FEA results of right exterior girder – Ultimate load at righter exterior girder

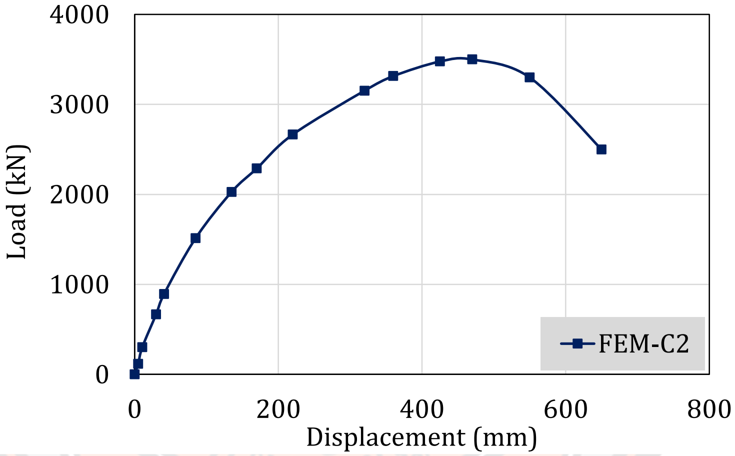

Figure 189 FEA results of middle girder – Ultimate load at middle girder

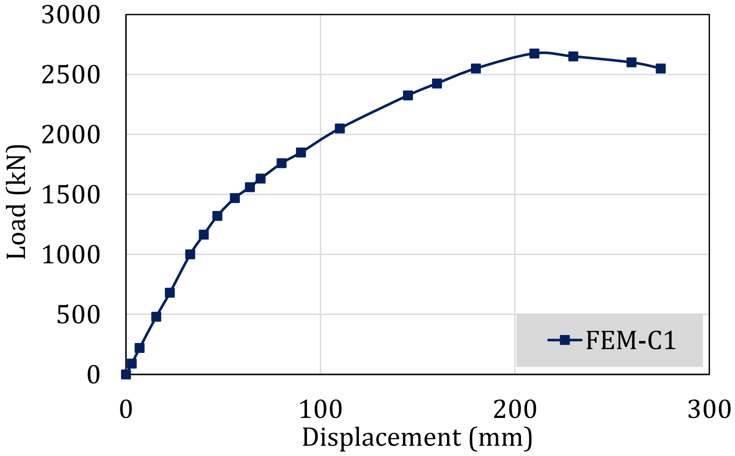

Figure 190 FEM results of left exterior girder – Combined ultimate load at left exterior and middle girder

4.3.1.2 Ultimate Failure Modes

The ultimate failure modes and crack patterns of FPPC girder as observed in finite element analysis are shown in Figs. 191 and 192. It can be seen that the crack pattern observed in finite element analysis are in well agreement with the experimental results. Similar to the experimental results, the severe cracks were observed at discontinuous ends and interior pier segment.

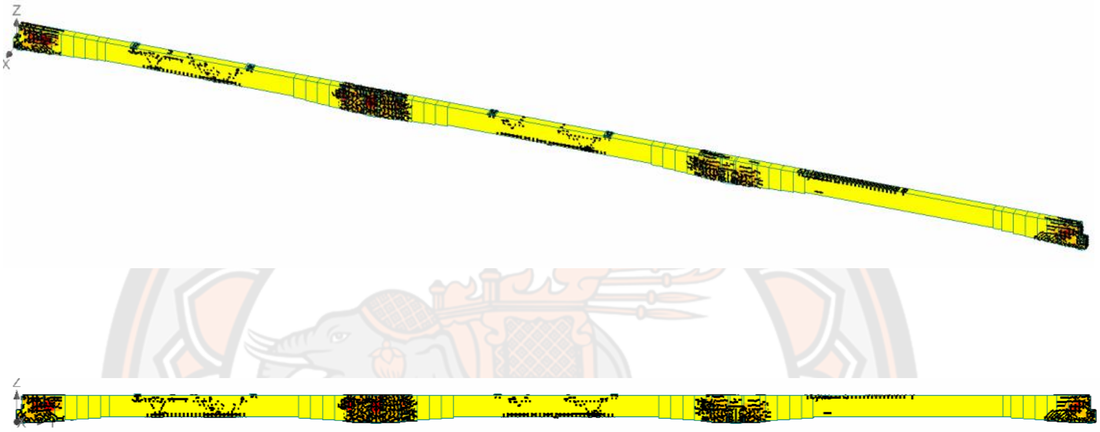

Figure 191 Cracking pattern observed in the finite element analysis

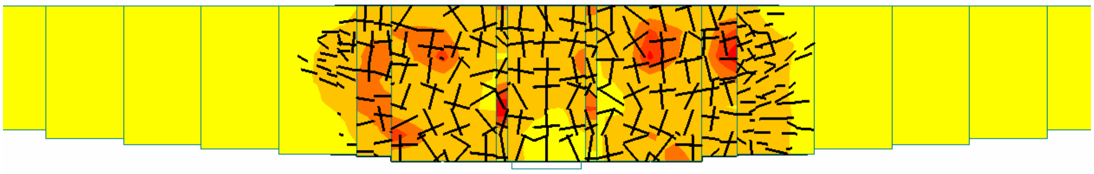

Figure 192 Cracking of pier segment as observed in finite element analysis

4.3.1.2 Behavior of Continuous FPPC Girder

The finite element analysis results presented in the previous sections (4.3.1.1 and 4.3.1.2) has clearly demonstrated that the ATENA program is quite success full to simulate the behavior of continuous FPPC girder. The recorded load versus deflection responses shown in Figures 183-187 show that the FPPC girder behaved as a continuous FPPC girder. Further, the cracking patters presented in the Figures 191 and 192 are clearly showing the development of negative moments at the intermediate ends. Although, the finite element model has clearly demonstrated that the behavior of FPPC girder in ATENA is a continuous girder, however, for further research, it is recommended to develop more finite element models considering different parameters such as the absence of the distributed reinforcement, spacing of shear reinforcement and amount of the longitudinal reinforcement.

Chapter V
Conclusions

In This study, in Part A, the experimental behaviour of the full-scale precast post-tensioned continuous (FPPC) girder for straddle monorail was conducted. The full-scale FPPC girder represents the actual size, design and construction details of a newly designed monorail transit system (Yellow Line and Pink Line Monorail) in Bangkok, Thailand. The FPPC girder was constructed and tested at the casting yard of Sino-Thai Engineering and Construction Public Company Limited (STECON), located at Saraburi Province, Thailand. In Part B, A total of 9 beams were tested in three groups depending upon the presence/configuration of CFRP sheets. Each group comprised of 3 beams: one with solid section, one with an internal square opening of 50×50mm, and one with internal opening of 100×100mm. Group 1 beams were tested in as-built condition. Beams of group 2 were strengthened with a single CFRP sheet bonded their soffits whereas group 3 beams were strengthened with a single U-shape CFRP sheet bonded to their tensile regions. Each beam was tested under four-point bending. Objectives were to study the effect of internal openings on flexural response of RC beams and beneficial effects of CFRP sheet. Further, it was deemed to study configuration of CFRP sheets yielding optimum results. Whereas in Part C, Finite element analysis of FPPC monorail bridge girder was performed by using a computer program ATENA which is a computational tool for nonlinear engineering analysis of bridges and culverts. Based on the experimental and analytical studies, the following conclusions can be derived:

- The FPPC girder was observed to be uncracked at all locations under service load conditions.
- The load versus deflection responses of the FPPC girder at all locations were observed essentially linear under service load conditions. Moreover, the maximum deflection of the FPPC girder under all load conditions was marginally less than the permissible limits.

- The ultimate load of the FPPC girder was recorded at 2600 kN and corresponding ultimate deflection was observed at 210 mm. This observed value is higher than that of the design load. The first linear relation of load and deformation was observed until 550 kN, and severe crushing and splitting of the concrete were observed at continuous supports.
- The ultimate failure of the FPPC girder was mainly due to severe damage to the bearing at the discontinuous end.
- Comparing the load-deflection response of un-strengthened beams, cracking load decreased in beam with 50mm opening compared with that of the solid section beam. It was further reduced in beam with 100mm opening. Presence of an opening inside beam reduces its cracking load which is further reduced as the size of the opening is increased.
- In large-scale FPPC girder, the calculated factor of safety and demand-capacity-ratio are 9.11 and 3.64, respectively. These structural factors clearly state that the design of FPPC girder is reliable and accurate.
- In small-scale un-strengthened beams with 50 (B02) and 100mm (B03) square openings experienced similar ultimate loads and deflections to those of their counterpart solid section beam (B01).
- A comparison in ultimate loads sustained by beams with similar openings size or solid section beams revealed that lowest ultimate loads were recorded for un-strengthened beams. Application of CFRP in both configurations enhanced ultimate loads. However, this improvement was far superior in beams strengthened with U-shape CFRP sheets.
- Beams strengthened with CFRP sheet bonded to their bottom sides experienced sudden de-bonding of CFRP at their ultimate loads resulting in abrupt drop in the load. Similar drop in load was also observed for beams strengthened with U-shape CFRP due to sudden rupture along beams' corners. Nonetheless, degradation of peak load in either case did not fall below the corresponding load sustained by the control beam. This phenomenon was true for all beams except B09-HS100-SCB which experienced its load degradation lower than that of the control beam. This was attributed to excessive concrete crushing at its midspan resulting in a such distinctive behavior.

- Beam strengthened with CFRP experienced higher compressive longitudinal steel strains. This is an important aspect in flexural enhancement of beams with internal openings using CFRP. In the absence of inadequate negative longitudinal reinforcement, high compressive stresses above neutral axis can crush concrete prematurely resulting in brittle failure. A glimpse of such an abrupt load drop was observed in beam B09 that experienced significant concrete crushing.
- The finite element analysis results indicate that the computer program ATENA is well capable to predict the ultimate load carrying capacity, displacement and cracking patterns of FPPC girder.

REFERENCES

1. Galal, K. and Q. Yang, *Experimental and analytical behavior of haunched thin-walled RC girders and box girders.* Thin-walled structures, 2009. **47**(2): p. 202-218.
2. Pritchard, B., *HAUNCHED BRIDGES AND THE SUCKER DECK PRINCIPLE: BENEFICIALLY VARYING DECK DEPTH TO MATCH HEADROOM OVER OBSTACLE CROSSED.* Proceedings of the Institution of Civil Engineers-Structures and Buildings, 1994. **104**(1): p. 39-50.
3. Tang, T., et al., *Crushing analysis of thin-walled beams with various section geometries under lateral impact.* Thin-Walled Structures, 2016. **102**: p. 43-57.
4. Carrera, E., et al., *Nonlinear analysis of thin-walled beams with highly deformable sections.* International Journal of Non-Linear Mechanics, 2021. **128**: p. 103613.
5. El-Niema, E., *Investigation of concrete haunched T-beams under shear.* Journal of Structural Engineering, 1988. **114**(4): p. 917-930.
6. Lawson, R. and J. Rackham, *Design of haunched composite beams.* The Steel Construction Institute, 1989.
7. Horne, M., H. Shakir Khalil, and S. Akhtar, *The stability of tapered and haunched beams.* Proceedings of the Institution of Civil Engineers, 1979. **67**(3): p. 677-694.
8. Tena-Colunga, A., L.A. Urbina-Californias, and H.I. Archundia-Aranda, *Assessment of the shear strength of continuous reinforced concrete haunched beams based upon cyclic testing.* Journal of Building Engineering, 2017. **11**: p. 187-204.
9. Godínez-Domínguez, E.A., A. Tena-Colunga, and G. Juárez-Luna, *Nonlinear finite element modeling of reinforced concrete haunched beams designed to develop a shear failure.* Engineering Structures, 2015. **105**: p. 99-122.
10. Albegmprli, H.M., et al., *Reliability analysis of reinforced concrete haunched beams shear capacity based on stochastic nonlinear FE analysis.* Computers and Concrete, 2015. **15**(2): p. 259-277.
11. Vlasov, V., *Thin-walled elastic beams, Washington: The National Science Foundation, 1961.* Google Scholar.
12. Hou, C., K. Matsumoto, and J. Niwa, *Shear failure mechanism of reinforced concrete haunched beams.* Journal of JSCE, 2015. **3**(1): p. 230-245.
13. Jaafer, A.A. and A.W. Abdulghani. *Nonlinear finite element analysis for reinforced concrete haunched beams with opening*. in *IOP Conference Series: Materials Science and Engineering*. 2018. IOP Publishing.
14. Tena-Colunga, A., L.A. Urbina-Californias, and H.I. Archundia-Aranda, *Cyclic behavior of continuous reinforced concrete haunched beams with transverse reinforcement designed to fail in shear.* Construction and Building Materials, 2017. **151**: p. 546-562.
15. Tang, M.-C., *The New Shibanpo Bridge, Chongqing, China.* Structural engineering international, 2010. **20**(2): p. 157-160.
16. Ingebrigtsen, T., *Stolma bridge, norway.* Structural engineering international, 1999. **9**(2): p. 100-102.
17. Battista, R.C. and M. Pfeil, *Control of wind oscillations of Rio-Niterói bridge, Brazil.* Proceedings of the Institution of Civil Engineers-Structures and Buildings, 2010. **163**(2): p. 87-96.

18. Bao, Y., Y. Li, and J. Ding, *A case study of dynamic response analysis and safety assessment for a suspended monorail system.* International Journal of Environmental Research and Public Health, 2016. **13**(11): p. 1121.
19. Barton, H., *Monorails.* Journal of the Institution of Locomotive Engineers, 1962. **52**(285): p. 8-59.
20. Zhang, T., *APM and monorail for Urban applications*, in *Automated People Movers and Automated Transit Systems 2016*. 2016. p. 222-239.
21. Trahair, N., *Distortional buckling of overhanging monorails.* Engineering structures, 2010. **32**(4): p. 982-987.
22. Pu, Q., et al., *Fatigue behavior of prestressed concrete beam for straddle-type monorail tracks.* Applied Sciences, 2018. **8**(7): p. 1136.
23. Cai, C., et al., *Dynamic interaction of suspension-type monorail vehicle and bridge: numerical simulation and experiment.* Mechanical Systems and Signal Processing, 2019. **118**: p. 388-407.
24. Trahair, N., *Lateral buckling of monorail beams.* Engineering structures, 2008. **30**(11): p. 3213-3218.
25. He, X., *Application and prospect of straddle monorail transit system in China.* Urban Rail Transit, 2015. **1**(1): p. 26-34.
26. Voo, Y.L., S.J. Foster, and C.C. Voo, *Ultrahigh-performance concrete segmental bridge technology: Toward sustainable bridge construction.* Journal of Bridge Engineering, 2015. **20**(8): p. B5014001.
27. Ritdumrongkul, S., et al. *Design of Palm Jumeirah Monorail*. in *IABSE Symposium: Sustainable Infrastructure-Environment Friendly, Safe and Resource Efficient, Bangkok, Thailand, 9-11 September 2009*. 2009.
28. Kimijima, N., et al., *New urban transport system for middle east monorail system for Dubai Palm Jumeirah transit system.* Hitachi Review, 2010. **59**(1): p. 47.
29. Sirisonthi, A., et al., *Construction techniques and development of 1st monorail system in Thailand.* 2019.
30. Murray, C.D., et al., *Destructive testing and computer modeling of a scale prestressed concrete I-girder bridge.* Engineering Structures, 2019. **183**: p. 195-205.
31. Tanaka, Y., et al., *Innovation and application of UFC bridges in Japan.* Proceedings of UHPC, 2009: p. 112-120.
32. Graybeal, B.A., *Flexural behavior of an ultrahigh-performance concrete I-girder.* Journal of Bridge Engineering, 2008. **13**(6): p. 602-610.
33. Aravinthan, T., E. Witchukreangkrai, and H. Mutsuyoshi, *Flexural behavior of two-span continuous prestressed concrete girders with highly eccentric external tendors.* ACI Structural Journal, 2005. **102**(3): p. 402-411.
34. Murray, C.D., et al., *Experimental testing of older AASHTO Type II bridge girders with corrosion damage at the ends.* PCI Journal, 2019. **64**(1): p. 49-64.
35. Dymond, B.Z., C.E. French, and C.K. Shield, *Investigation of shear distribution factors in prestressed concrete girder bridges.* 2016.
36. Bagge, N., et al., *Full-Scale Tests to Failure Compared to Assessments–Three Concrete Bridges*, in *High Tech Concrete: Where Technology and Engineering Meet*. 2018, Springer. p. 1917-1924.

37. Abdel-Halim, M., R.M. McClure, and H.H. West, *Overload Behavior of an Experimental Precast Prestressed Concrete Segmental Bridge.* PCI J, 1987. **32**: p. 102-123.
38. Takebayashi, T., K. Deeprasertwong, and Y. Leung, *A FULL-SCALE DESTRUCTIVE TEST OF A PRECAST SEGMENTAL BOX GIRDER BRIDGE WITH DRY JOINTS AND EXTERNAL TENDONS.* Proceedings of the Institution of Civil Engineers-Structures and Buildings, 1994. **104**(3): p. 297-315.
39. Hashemi, S. and R. Al-Mahaidi, *Experimental and finite element analysis of flexural behavior of FRP-strengthened RC beams using cement-based adhesives.* Construction and Building Materials, 2012. **26**(1): p. 268-273.
40. Jendele, L. and J. Cervenka, *Finite element modelling of reinforcement with bond.* Computers & structures, 2006. **84**(28): p. 1780-1791.
41. Vecchio, F. and W. Shim, *Experimental and analytical reexamination of classic concrete beam tests.* Journal of Structural Engineering, 2004. **130**(3): p. 460-469.
42. Chaimahawan, P., et al., *Finite Element Analysis of Reinforced Concrete Pile Cap using ATENA.* Latin American Journal of Solids and Structures, 2021. **18**.
43. ASTM, S., *Standard specification for deformed and plain carbon-steel bars for concrete reinforcement ASTM A615.* A615M-09b (West Conshohocken: American Society for Testing and Materials), 2009.
44. ASTM. *Standard specification for low-relaxation, seven-wire steel strand for prestressed concrete*. 2016. ASTM West Conshohocken, PA.
45. International., A., *ASTM C109/C109M-12 Standard test method for compressive strength of hydraulic cement mortars (using 2-in. or [50-mm] cube specimens).* 2013.
46. ASTM, *C307-18. Standard Test Method for Tensile Strength of Chemical-Resistant Mortar, Grouts, and Monolithic Surfacings.* ASTM Int, 2018.
47. Institue, A.C., *(ACI)-ASCE Committee. Guide for the analysis and design of reinforced and prestressed concrete guideway structures. ACI 343.1R-12.* American Institute, Farmingston Hills, MI., 2012.
48. AASHTO 2nd, L., *Bridge design specifications.* American association of state highway and transportation officials, Washington, DC, 1998.
49. Červenka, V., L. Jendele, and J. Červenka, *ATENA Program Documentation–Part 1.* Cervenka Consulting sro, 2000.
50. Cervenka, V., J. Cervenka, and R. Pukl, *ATENA—A tool for engineering analysis of fracture in concrete.* Sadhana, 2002. **27**(4): p. 485-492.
51. Mello, A.F.A.d. and R.A.d. Souza, *Analysis and design of reinforced concrete deep beams by a manual approach of stringer-panel method.* Latin American Journal of Solids and Structures, 2016. **13**: p. 1126-1151.
52. Shaaban, I.G. and M. Said, *Finite element modeling of exterior beam-column joints strengthened by ferrocement under cyclic loading.* Case studies in construction materials, 2018. **8**: p. 333-346.
53. Hussain, Q. and A. Pimanmas, *Shear strengthening of RC deep beams with sprayed fibre-reinforced polymer composites (SFRP) and anchoring systems: part 1. Experimental study.* European Journal of Environmental and Civil Engineering, 2016. **20**(1): p. 79-107.
54. Hussain, Q. and P. Joyklad, *Effect of lateral reinforcement ratio on strength and ductility of RC columns.* Kasem Bundit Engineering Journal, 2017. **7**(1): p. 1-16.